Universidad Autónoma de Madrid

Thermopower and Conductance of Single-Molecule Junctions and Atomic Contacts

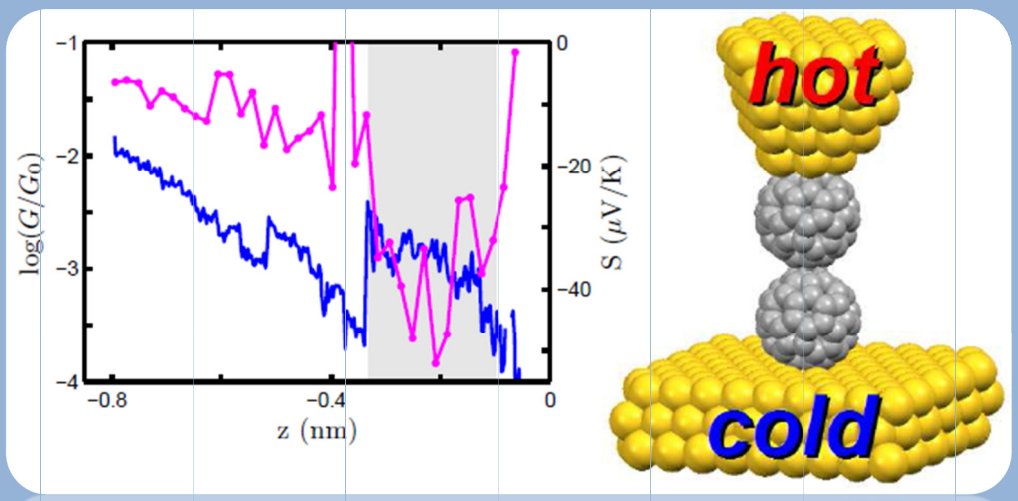

Charalambos Evangeli

Madrid 2014

Cover: Conductance at 100 mV (blue) and thermopower (magenta), simultaneously acquired, during the formation of the C_{60} dimer. In this measurement,the temperature difference between the tip and the substrate was $\Delta T = 12\ \mathrm{K}$.

Thermopower and Conductance of Single-Molecule Junctions and Atomic Contacts

Memoria presentada por

Charalambos Evangeli

para optar al grado de Doctor en Ciencias Físicas por la Universidad Autónoma de Madrid

Dirigida por

Nicolás Agraït de la Puente

Departamento de Física de la Materia Condensada

Madrid, Noviembre 2014

Thermopower and Conductance of Single-Molecule Junctions and Atomic Contacts

Thesis Presented by

Charalambos Evangeli

for the degree of Doctor in Physics by Universidad Autónoma de Madrid

Thesis Supervisor

Nicolás Agraït de la Puente

Department of Condensed Matter Physics

Madrid, November 2014

Thesis committee:

Prof. Julio Gómez Herrero (Universidad Autónoma de Madrid)
Prof. Jan M. van Ruitenbeek (Leiden University)
Prof. Juan Carlos Cuevas Rodríguez (Universidad Autónoma de Madrid)
Prof. Colin J. Lambert (University of Lancaster)
Prof. José Ignacio Pascual Chico (CIC nanoGUNE)

This work has been supported by the European Union (FP7) through programs ITN "FUNMOLS" Project Number 212942, ELFOS and by the A.G. Leventis Foundation.

Acknowledgements

This work has been the result of the collaboration of many people throughout the last 5 years. I would like to acknowledge everybody that helped, with the hope that I will not forget anybody.

First, a heartfelt thanks to my supervisor Nicolás Agraït, who trusted me and gave me the opportunity to work on this project. His daily guidance and support in the lab was indispensable. He was always available and patient with me, spending time discussing the problems which arose during the realization of this work. I learned a lot from him about experiments, and Physics in general.

Teresa González and Edmund Leary, who taught me and guided me in the laboratory. They were there, ready to help with every problem. We spent many long hours discussing a multitude of issues, and without their invaluable input this project would never have come to fruition.

Thanks to José Gabriel Rodrigo, for helping with issues surrounding the experimental setup. Andrés Buendía and Rosa Díez, Santiago Marquez and Juan Benayas our technicians, for all their help in designing and constructing the experimental setups.

Professor Colin Lambert, for the four months I spent with his group and all the collaboration we had during all these years, and also for the many nights of "Golden Lion" entertainment. Thanks to all his group in Lancaster University; David, David (with the long hair), Rachel, Iain, Ali, Steven and Csaba for the patience they had to teach and collaborate with an experimentalist! In particular, Kataline, for teaching me about theoretical calculations, helping me with settling, and all the collaboration we had. Vasilis, Thanos, Christos for making more pleasant my stay in Lanchaster.

Professor Michele Calame, for the short stay at his group in the University of Basel, all the people of his group and especially Cornelia, Jan and Toni.

Thanks to all the people in our group: Aday, Jorge, Laura, Siya, Guille, for tolerating my swearing in Greek, particularly during the last few months. Siya, for being a great partner in the lab, working together, even on the overnight experiments, and being a gracious tour guide in India. Laurita, the only optimistic person in the lab, for helping me with translations; Aday, for the many hours of group therapy, with and without alcohol, for our lab-complaints; Guille, for elevating the atmosphere of the lab with early morning calls for las camisetas amarillas and Jorge (Giorgos), for always being "focusado".

Thanks to the people from the Low Temperatures Lab. Mersak, the big brother, for his help and support from the first day I entered the lab. Your talent for communicating through "Franglishñolbic" was very much appreciated. Tomás, for his noisy pump (as he was saying: All your results are thanks to my pump). Bisher, for his help with communication issues in Spanish, especially the first few months in the lab. Augusto, Ana, Andrés, Roberto, Edwin, Antón, Isa and Pepe for making daily life in the lab better with their humour and energy. The two senior PhD students of my group, Carlos and Andrés, for teaching me about experimental techniques. Manuel and Jan, for the Fontana Friday nights. Jan, thanks for insisting on disconnecting from the stress of the week. Thanks also to the people on the other floors - Ahmad, Michelle, Curro, Antonio, Michelle, Mohamed, Amjad, Guillermo, David, Juanpe …apologies to anyone I have omitted!

The people of the FUNMOLS network, for the nice moments of Net-working and Not-working during the meetings. Andrea, for his "sexy" molecules, all the parties in Madrid and trips; Toni, the relaxed guy; Pavel, for all the discussions with a guy who knows about the real difficulties of life; Murat, my Turkish friend who showed me that friendships between people go beyond national issues; lastminuteAndres.es; Marta, for our discussions about life; Hui, the optimistic girl of the network and Giorgio, the serious one, and Mateus, my Polish twin. Also, all the professors of the Network for the discussions, scientific collaboration and various contributions to our progress; Nazario Martín, for providing us with molecules; Martin Bryce, Heike Riel, Dirk Guldi, Thomas Wandlowski and Jan Jeppesen.

During this thesis I had the opportunity to collaborate with people from other

groups and Universities in order to complete this work. Juan Carlos Cuevas and his group for the theoretical calculations, and for shattering the stereotypes regarding theoretical physicists (i.e. thanks for explaining things to me in a clear and simple manner). Prof. M. Nielsen, for synthesizing the molecules and Prof. G. Solomon, for the theoretical calculations.

Thanks to the professors of the laboratory; Miguel Ángel Ramos, Hermann Suderow, Sebastián Vieira and Gabino Rubio-Bollinger. Also to the secretaries of the Department Elsa Sánchez and Luisa Carpallo.

It would not be possible not to mention my friends outside the laboratory for their support, especially in the last difficult year; The QC group - Mic, Nicole, Neil, Patricia, Silvia, Marilena and Andrea for the BBQ therapy; and also Marco, Vanessa, Nuria and Pablo for all help and the nice moments. Neil – thank you - for your patience reading and understanding everything about “the expansion of the tip when it is heated, and its subsequent approach towards the sample”, in order to correct the English of this thesis.

All my friends in Cyprus and Greece and my cousins for the nice holidays we had together during all these years, giving me the energy to continue. Kyras, Mouskos, Pomos, Giorkos, Andreas, Petros, Tomis, Mpampis, Michalis, Natasa, Christoforos, Christos, Vasilis, Mikela, Louda, Achileas and Christodoulos.

I would like also to thank my football team APOEL for all the great moments in the Champions League in Porto, Lyon, Madrid, London, Barcelona and Paris. Short one-day breaks from the daily routine with amazing memories.

Thanks to everybody that I forgot to mention!

Finally, and most importantly, my parents Andreas and Paraskevi. They supported me in everything during these years. I owe everything to them. The last wish of my father was to be here with me for this important moment of my life but unfortunately he couldn’t make it.

Table of Contents

Figures and Tables Index

Abstract

Thermoelectric effects in molecular junctions are of great interest from fundamental and applied point of view. Indeed, organic thermoelectric materials are believed to be one of the potential solutions for key energy problems like the problem of waste heat recovery (e.g. from transportation vehicles) or the heat dissipation problem (e.g. in microelectronics). Present day inorganic thermoelectric materials, despite the good performance, are already globally limited, relatively difficult to process (energetically expensive and toxic), heavy and brittle for use in everyday life. Organic thermoelectric materials are promising alternatives since they are light, flexible and potentially cheap, although their present efficiency still needs to be improved. A strategy for enhancing the thermoelectric performance is the introduction of nanostructures and multiple interfaces [See2010]. Thus, one of the most important open problems in nanoscience concerns the understanding and optimization of thermoelectricity in organic thermoelectric materials at the nanoscale [Zhang2014].

Single-molecule junctions formed using scanning probe techniques constitute an excellent model system to study the processes occurring at the organic-inorganic interface at a fundamental level. In most of the experiments in molecular junctions, the electronic conductance is typically the only magnitude measured. Quite recently, the possibility of measuring the thermopower to give further insight into the transport process has been demonstrated [Reddy2007] and is currently used by just a few groups [Baheti2008; Widawsky2011; Yee2011].

The main goal of this thesis has been to study experimentally the thermopower and conductance of single-molecule junctions using a scanning tunneling microscope (STM) in ambient conditions. An important part of this work is the construction of a new STM head specifically designed for these measurements and the development of a novel powerful technique for measuring simultaneously the thermopower and

conductance of single-molecule junctions, making a complete characterization of the molecular junction possible. This is detailed in chapter 4.

In chapter 5, this new technique is used to measure the thermopower of C_{60} molecules and demonstrate the possibility of engineering the thermopower of a molecular junction by molecular scale manipulation, in particular, the enhancement of thermopower by forming a C_{60} dimer is shown.

The thermoelectric properties of atomic nanocontacts of gold and platinum are explored in chapter 6. As contact size dimensions are reduced, a crossover from bulk to quantum behaviour involving a change of sign of the thermopower takes place. Interestingly, quantum oscillations are observed in gold atomic-size contacts, whereas in platinum they are totally absent. This difference between gold and platinum is traced back to the different electronic structure of these two metals.

In chapter 7 the effect of lateral chains on the thermopower of OPE derivatives is examined. The addition of lateral chains is found to increase the thermopower as it brings the Fermi level closer to molecular resonances. An enhancement of thermopower with stretching of the molecule is also observed.

Finally, in chapter 8 the use of C_{60} as a linker in molecular junctions is explored by forming single-molecule junctions of dumbbell molecules, consisting of two fullerenes joined by a conjugated backbone.

References

[Baheti2008] Baheti, K., J. A. Malen, P. Doak, P. Reddy, S.-Y. Jang, et al. (2008). "Probing the Chemistry of Molecular Heterojunctions Using Thermoelectricity." Nano Letters **8**(2): 715-719.

[Reddy2007] Reddy, P., S.-Y. Jang, R. A. Segalman and A. Majumdar (2007). "Thermoelectricity in Molecular Junctions." Science **315**(5818): 1568-1571.

[See2010] See, K. C., J. P. Feser, C. E. Chen, A. Majumdar, J. J. Urban, et al. (2010). "Water-Processable Polymer−Nanocrystal Hybrids for Thermoelectrics." Nano Letters **10**(11): 4664-4667.

[Widawsky2011] Widawsky, J. R., P. Darancet, J. B. Neaton and L. Venkataraman (2011). "Simultaneous Determination of Conductance and Thermopower of Single Molecule Junctions." Nano Letters **12**(1): 354-358.

[Yee2011] Yee, S. K., J. A. Malen, A. Majumdar and R. A. Segalman (2011). "Thermoelectricity in Fullerene–Metal Heterojunctions." Nano Letters **11**(10): 4089-4094.

[Zhang2014] Zhang, Q., Y. Sun, W. Xu and D. Zhu (2014). "Organic Thermoelectric Materials: Emerging Green Energy Materials Converting Heat to Electricity Directly and Efficiently." Advanced Materials **26**(40): 6829-6851.

Resumen

Los efectos termoeléctricos en uniones moleculares son de gran interés tanto desde el punto de vista fundamental como de las aplicaciones. De hecho, los materiales termoeléctricos orgánicos son considerados una solución potencial para problemas energéticos clave como el problema de la recuperación de calor perdido (por ejemplo, en vehículos de transporte) o el problema de la disipación de calor (por ejemplo, en microelectrónica). Los materiales termoeléctricos inorgánicos actuales, a pesar de su buen rendimiento, están ya limitados globalmente, son relativamente complicados de producir (son energéticamente caros y tóxicos), y resultan demasiado pesados y frágiles para su uso en la vida diaria. Los materiales termoeléctricos orgánicos son una alternativa prometedora para los actuales materiales termoeléctricos inorgánicos debido a que son ligeros, flexibles y potencialmente económicos, aunque su eficiencia actual aún necesita ser mejorada. Una estrategia para mejorar el rendimiento termoeléctrico es la introducción de nanoestructuras y fronteras múltiples [See2010]. Por consiguiente, uno de los problemas abiertos más importantes en nanociencia incluye la comprensión y optimización de la termoelectricidad en materiales termoeléctricos orgánicos en la nanoescala [Zhang2014].

Las uniones moleculares consistentes en única molécula y formadas utilizando técnicas de barrido local constituyen un sistema modelo excelente para estudiar los procesos que ocurren en la frontera orgánico-inorgánico a nivel fundamental. En la mayoría de experimentos en uniones moleculares, la conductancia electrónica es típicamente la única magnitud medida. Recientemente se ha demostrado la posibilidad de medir thermopower para obtener una mejor comprensión del proceso de transporte [Reddy2007] y en la actualidad sólo algunos grupos la utilizan [Baheti2008; Widawsky2011; Yee2011].

El principal objetivo de esta tesis ha sido estudiar experimentalmente el thermopower y la conductancia de uniones moleculares formadas por una única molécula utilizando un microscopio de efecto túnel (STM) en condiciones ambiente.

Una parte importante de este trabajo es la construcción de una nueva cabeza de STM diseñada especialmente para estas medidas y el desarrollo de una nueva y potente técnica que permite la medición simultánea de thermopower y conductancia de uniones moleculares formadas por una sola molécula, haciendo posible una caracterización completa de la unión molecular. Esto se detalla en el capítulo 4.

En el capítulo 5, esta nueva técnica es utilizada para medir el thermopower de moléculas C_{60} y para demostrar la posibilidad de hacer ingeniería con el thermopower de una unión molecular mediante la manipulación a escala molecular; en particular, se muestra el incremento del thermopower mediante la formación de dímeros de C_{60}.

Las propiedades termoeléctricas de nanocontactos atómicos de oro y platino se exploran en el capítulo 6. Según se reducen las dimensiones del contacto, tiene lugar un cruce desde el comportamiento en volumen al comportamiento cuántico que incluye un cambio de signo del thermopower. Se observan oscilaciones cuánticas muy interesantes en los contactos de oro de tamaño atómico, mientras que están totalmente ausentes en el platino. El origen de esta diferencia entre oro y platino se encuentra en las estructuras electrónicas diferentes de estos dos metales.

En el capítulo 7 se examina también el efecto de cadenas laterales en el thermopower de derivados de moléculas OPE. Se ha encontrado que la adición de cadenas laterales incrementa el thermopower dado que acercan el nivel de Fermi a las resonancias moleculares. También se ha observado un aumento del thermopower al estirar la molécula.

Finalmente, en el capítulo 8 se explora la posibilidad de utilizar C_{60} como enlace en uniones moleculares, mediante la formación de uniones moleculares compuestas por una única molécula dumbbell, consistente en dos fullerenos unidos por una columna conjugada.

Referencias

[Baheti2008] Baheti, K., J. A. Malen, P. Doak, P. Reddy, S.-Y. Jang, et al. (2008). "Probing the Chemistry of Molecular Heterojunctions Using Thermoelectricity." Nano Letters **8**(2): 715-719.

[Reddy2007] Reddy, P., S.-Y. Jang, R. A. Segalman and A. Majumdar (2007). "Thermoelectricity in Molecular Junctions." Science **315**(5818): 1568-1571.

[See2010] See, K. C., J. P. Feser, C. E. Chen, A. Majumdar, J. J. Urban, et al. (2010). "Water-Processable Polymer−Nanocrystal Hybrids for Thermoelectrics." Nano Letters **10**(11): 4664-4667.

[Widawsky2011] Widawsky, J. R., P. Darancet, J. B. Neaton and L. Venkataraman (2011). "Simultaneous Determination of Conductance and Thermopower of Single Molecule Junctions." Nano Letters **12**(1): 354-358.

[Yee2011] Yee, S. K., J. A. Malen, A. Majumdar and R. A. Segalman (2011). "Thermoelectricity in Fullerene–Metal Heterojunctions." Nano Letters **11**(10): 4089-4094.

[Zhang2014] Zhang, Q., Y. Sun, W. Xu and D. Zhu (2014). "Organic Thermoelectric Materials: Emerging Green Energy Materials Converting Heat to Electricity Directly and Efficiently." Advanced Materials **26**(40): 6829-6851.

Part I:
Background

1 Quantum Electron Transport

At the nanoscale the classical physics knowledge about the electrical properties of conductors and semiconductors does not apply and a quantum mechanical approach is needed. In this chapter I will introduce the basic definitions for electron transport in the nanoscale that will be used in the following chapters for the characterization of single molecules and atomic contacts. I will follow the description in ref. [Cuevas2010] explaining the basic theory of quantum tunneling and the Landauer formalism for quantum transport.

1.1 Introduction

The classical Ohm's law for macroscopic conductors implies that the conductance G is proportional to the traverse area S and inversely proportional to the length L of the given sample

$$G = \sigma S/L. \qquad \text{Equation 1-1}$$

This is the result of scattering of the carriers due to defects and impurities of the material. However, when the size of the material is much smaller, a quantum mechanical approach is needed to describe the electrical properties of the material.

1.2 The Landauer formula

The scattering approach is the most popular theoretical formalism for the description of the coherent transport in nanoscale junctions. We consider the typical transport experiment where the system to be examined is the sample (nanojunction with dimensions at the nanoscale) and it is connected to the macroscopic contacts by two leads (see Figure 1-1a). The leads are the electron reservoirs with a defined temperature and chemical potential. The idea in the scattering approach is to connect the transmission and reflection probabilities through the sample with the electronic transport.

Let us first consider the nanojunction as the one dimensional rectangular potential shown in Figure 1-1b. The electrons coming from the leads are scattered from this potential. We consider an incoming electron as a plane wave, e^{ikx}, which will be partially reflected by the barrier, re^{-ikx} (r is the probability amplitude) and partially transmitted, te^{ikx} with probability $T = |t|^2$.

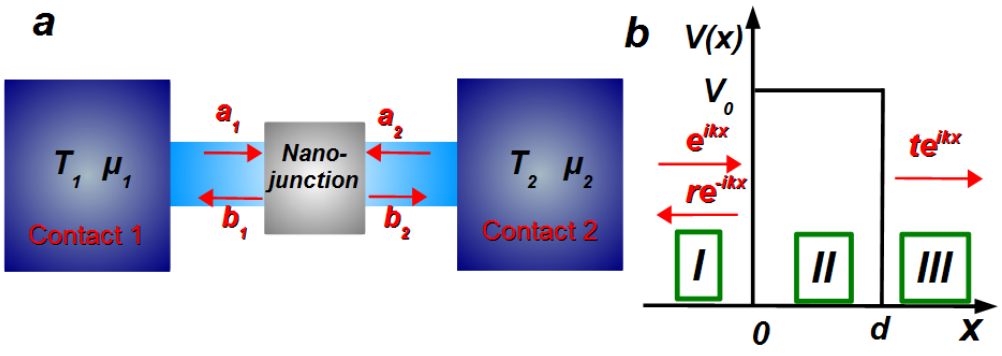

Figure 1-1: Transport through a nanojunction. (a) Nanojunction connected to two large contacts through two leads. (b) Rectangular potential barrier of height V_0 and width d.

The electrical density carried by an electron is given by the quantum mechanical expression:

$$J_k = \frac{\hbar}{2mi}\left[\Psi^*(x)\frac{d\Psi}{dx} - \Psi(x)\frac{d\Psi^*}{dx}\right] = \frac{e}{d}v(k)T(k), \qquad \text{Equation 1-2}$$

where $v(k) = \hbar k/m$is the group velocity, d is the length of the system.

For the system we examine, many electrons are participating in the transport so that we have to consider a sum over k and take into account the Pauli principle by introducing a factor $f_1(k)[1 - f_2(k)]$, where $f_{1,2}$ are the Fermi distributions in reservoir 1 and 2. This factor will ensure that the initial occupied states of reservoir 1 and the empty states of reservoir 2 are contributing to the current flow from 1 to 2 which will be given by:

$$J_{1\to2} = \frac{e}{d}\sum_k v(k)T(k)\, f_1(k)[1 - f_2(k)]. \qquad \text{Equation 1-3}$$

By converting the sum to an integral and changing variable k to E by introducing the density of states $dk/dE = m/\hbar^2 k$, we get:

$$J_{1\to2} = \frac{e}{h}\int dE\; T(E)\, f_1(E)[1 - f_2(E)]. \qquad \text{Equation 1-4}$$

In the same way, the current from reservoir 2 to 1 is given by

$$J_{2\to1} = \frac{e}{h}\int dE\; T(E)\, f_2(E)[1 - f_1(E)], \qquad \text{Equation 1-5}$$

and the total current is

$$I(V) = J_{1\to2} - J_{2\to1} = \frac{2e}{h}\int dE\; T(E)\,[f_1(E) - f_2(E)]. \qquad \text{Equation 1-6}$$

This is the Landauer formula and it illustrates the close relation between current and transmission. An extra factor 2 is added because of the spin degeneracy. At zero temperature, $f_1(E)$ and $f_2(E)$ are step functions and are equal to 1 below

their chemical potentials $\mu_1 = E_F + eV/2$ and $\mu_2 = E_F - eV/2$ respectively, and 0 above this energy. The net current then for low voltages is $I = GV$ and the conductance is given by:

$$G = \frac{2e^2}{h}T. \qquad \text{Equation 1-7}$$

For one single-mode conductor the conductance is given by the universal quantity $G_0 = 2e^2/h \approx 12.9\ \mathrm{K\Omega}$.

Let us now go back to the general two-lead scattering problem (Figure 1-1a) in order to extract the multichannel Landauer formula. The reservoirs 1 and 2 have temperatures $T_{1,2}$, chemical potentials $\mu_{1,2}$ and the distribution of the electrons inside them is described by the Fermi distribution. We assume that far from the sample the transverse (perpendicular to the direction of transport) and the longitudinal (along the direction of transport) motion of the electrons can be separated. In the longitudinal direction the system is open, and is characterized by a continuous wavevector k_l and a longitudinal energy $E_l = \hbar^2 k_l^2/2m$. The transverse motion is quantized and described by a discrete index n and the transverse energies $E_{1,2;n}$. These states are called quantum channels. The total energy is $E = E_n + E_l$, and since E_l is positive, for a given total energy, E, only finite number of channels exist. $\hat{a}_{1,2}$ and $\hat{b}_{1,2}$ (see Figure 1-1a) are the operators describing the incoming electrons impinging on the sample and the outgoing respectively, and they are related through the scattering matrix $\hat{S}$:

$$\hat{S} = \begin{pmatrix} \hat{r} & \hat{t}' \\ \hat{t} & \hat{r}' \end{pmatrix}, \qquad \text{Equation 1-8}$$

where the blocks $\hat{r}$ and $\hat{r}'$ describe the electron reflection back to the resevoirs 1,2 and the blocks $\hat{t}$ and $\hat{t}'$ the electron transmission through the sample.

The Landauer formula can be generalized to multiple transverse energies, by introducing the matrix $\hat{t}\hat{t}^\dagger$ which can be extracted with simple matrix algebra from the scattering matrix. $T_n(E)$ are its eigenvalues (transmission coefficients) with values $0 < T_n(E) < 1$. The corresponding wavefunctions are referred as

eigenchannels or conduction channels. n is the index for the transverse (across the leads) quantized motion of the electrons. Finally, the current is given by:

$$I = \frac{e}{h}\sum_{n}\int_{-\infty}^{\infty} dE\, T_n(E)[f_1(E) - f_2(E)], \qquad \text{Equation 1-9}$$

and the conductance

$$G = \frac{e^2}{h}\sum_{n} T_n, \qquad \text{Equation 1-10}$$

which is the multichannel generalization of Landauer formula.

In the following paragraphs I will describe two special cases of the Landauer approach, the quantum tunneling through a barrier and transport through a molecular junction.

1.3 Quantum tunneling

The Landauer approach, described above, illustrates the close relation between current and transmission. In this section I will show an example of how the transmission coefficient can be computed for a simple situation. We consider a one dimensional rectangular potential of height V_0 (see Figure 1-2a) and an incoming electron with energy E and mass m. Classical mechanics predicts that the electron will be reflected if $E < V_0$. In contrast, quantum mechanics predicts that it can pass through the barrier and this phenomenon is what is called quantum tunneling. The probability of the electron passing through the barrier is given by the transmission coefficient, T. In order to calculate the transmission T we find the wave functions in the three different regions I, II and III (see Figure 1-2a) from the time independent Schrodinger equation

$$-\frac{\hbar^2}{2m}\frac{d^2\Psi(x)}{dx^2}+V(x)=E\Psi(x),$$

Equation 1-11

with $V(x)=\begin{cases}V_0 & 0\le x\le d\\ 0 & otherwise\end{cases}$.

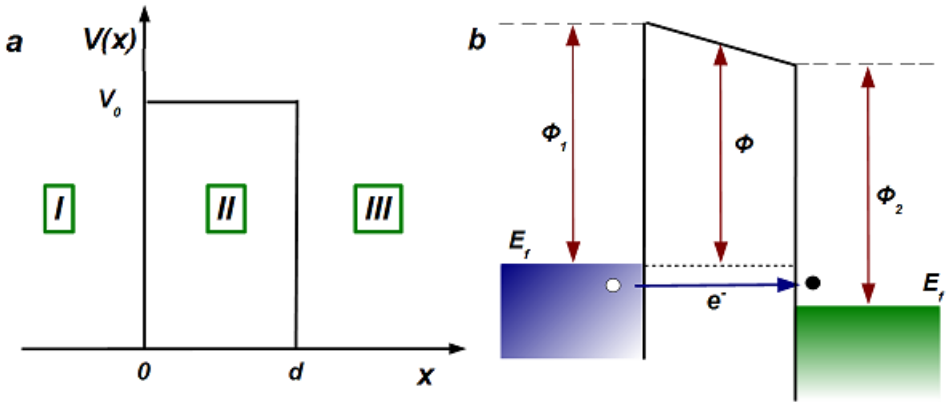

Figure 1-2: Quantum electron tunneling. (a) Rectangular potential barrier of height V_0 and width d. (b) Tunneling through a junction of two metallic electrodes separated with an insulated film when a small voltage is applied.

The solutions of the Schrödinger equations in the three regions are

$$\Psi_I=a_1e^{ik_1x}+b_1e^{-ik_1x},$$

$$\Psi_{II}=a_2e^{k_2x}+b_2e^{-k_2x},$$

$$\Psi_{III}=a_3e^{ik_3x},$$

Equation 1-12

where $k_1=k_3=\frac{\sqrt{2mE}}{\hbar}$ and $k_2=\frac{\sqrt{2m(V_0-E)}}{\hbar}$.

Then we match these functions and their first derivatives at the boundaries ($x=0$, $x=d$). Finally for $E<V_0$ we get for the transmission coefficient:

$$T = \left|\frac{a_3}{a_1}\right|^2 = A.\, e^{-2k_2 d}. \qquad \text{Equation 1-13}$$

When a voltage is applied a small drop appears in the potential profile (see Figure 1-2b). According to the calculations of Simmons, for a very small voltage the net current density is a linear function of the applied voltage V and is given by:

$$I \propto Ae^{-\alpha\sqrt{\varphi}d}, \qquad \text{Equation 1-14}$$

where $\alpha = \frac{2}{\hbar}\sqrt{2m}$ [Binnig1982].

This formula gives an explanation for the exponential decay of the low bias conductance. It has a strong exponential dependence on the barrier width d and the effective barrier height (work function) $\varphi = V_0 - E$, which depends on the material and the experimental conditions.

1.4 Quantum transport through molecular junctions

Another special case of the Landauer approach is transport through a molecular junction connected to the macroscopic contacts by two leads (see Figure 1-3). In the low voltage regime the transport mechanism through a molecule is mainly tunneling and can be described with the scattering approach. We consider the level scheme of Figure 1-3a, where molecular orbitals are within the junction and they are occupied up to the highest occupied molecular orbital (HOMO). The Fermi energy of the metallic leads is between the HOMO-LUMO (lowest unoccupied molecular orbital) gap of the molecule. The molecular orbitals are broadened depending on the metal-molecule coupling and many molecular orbitals can participate in the transport.

However, a simplified model for transport, the “single-level resonant tunneling model”, considers that the main participant is the closest to the Fermi energy. Having this in mind, we can draw the schematic in Figure 1-3b. The main

parameters of the model are the level position (ε_0) measured with respect to the Fermi energy of the electrodes and the scattering rates Γ_{LR} describing the coupling to the metal electrodes.

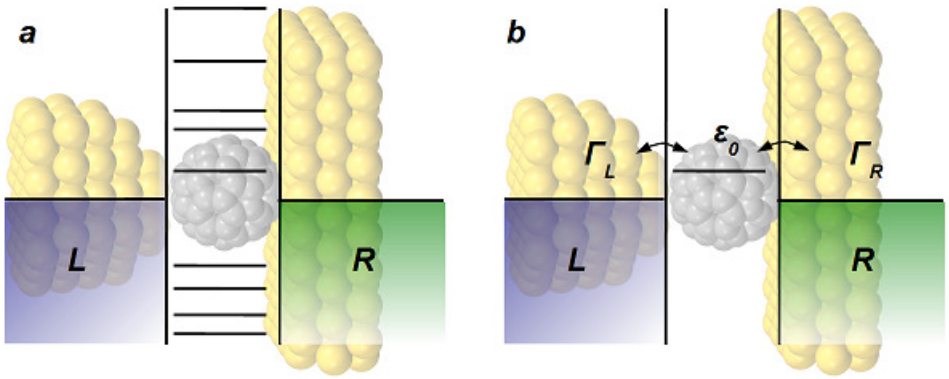

Figure 1-3: Level schemes for molecular junction. (a) Typical molecular junction that has several discrete energy levels whereas the metallic leads have continuous fill states up to the Fermi energy. (b) Molecular junction where transport is dominated by a single energy level, ε_0.

The $I-V$ characteristics of such a junction can be extracted from the Landauer formula by using the energy and voltage dependent transmission coefficient, $T(E,V)$, given by the Breit-Wigner formula:

$$T(E,V) = \frac{4\Gamma_L\Gamma_R}{[E-\varepsilon_0(V)]^2 + [\Gamma_L+\Gamma_R]^2} \qquad \text{Equation 1-15}$$

References

[Binnig1982] Binnig, G., H. Rohrer, C. Gerber and E. Weibel (1982). "Surface Studies by Scanning Tunneling Microscopy." Physical Review Letters **49**(1): 57-61.

[Cuevas2010] Cuevas, J. C. and E. Scheer (2010). Molecular Electronics: An Introduction to Theory and Experiment, World Scientific.

Thermoelectric Effects

Thermoelectric effects are due to the coupling of thermal and electrical transport. In this chapter I will focus on the theory of one particular thermoelectric effect, the Seebeck effect or thermopower. In the atomic scale the Seebeck effect is governed by quantum effects that are radically different from the mechanisms governing thermopower in macroscopic systems. I will first introduce all the definitions for the classical theory of the Seebeck effect and then I will continue with the theory of thermopower at the nanoscale. The scattering approach used in the previous chapter to describe the electronic transport is used here to describe quantum thermoelectric effects.

2.1 Thermoelectric effect

In many metals and semiconductors there is a coupling between the electrical current and the thermal current, which gives rise to thermoelectric phenomena [Dresselhaus2001]. There are three thermoelectric effects that appear in thermoelectric devices, the Seebeck effect, Peltier effect, and Thomson effect.

Seebeck effect

Seebeck effect is the conversion of a temperature difference to electricity. When a metallic bar is subjected to a voltage, V, or a temperature (T) difference an electric current will be generated. The electric current density, $\bar{J}$, will be given by:

$$\bar{J} = \sigma(-\bar{\nabla}V + \bar{E}_{th}), \qquad \text{Equation 2-1}$$

where σ is the conductivity and $\bar{\nabla}V$ is the voltage gradient. $\bar{E}_{th} = -S\bar{\nabla}T$ is the field generated locally by the thermal electromotive force, where S is what called Seebeck coefficient.

If the system reaches a steady state where $\bar{J} = 0$ everywhere then

$$\bar{\nabla}V = -S\bar{\nabla}T, \qquad \text{Equation 2-2}$$

If the temperature difference (ΔT) between the two ends of the material is small then:

$$S = -\frac{\Delta V}{\Delta T} \qquad \text{Equation 2-3}$$

where ΔV is the thermoelectric voltage at the two ends.

Peltier effect

Peltier Effect is the heating or cooling effect created at a junction of two different conductors A and B, when an electric current flows through the junction. Heating or cooling depends on the direction of the current. The Peltier heat that is generated at the junction per unit time is given by

$$\dot{Q} = (\Pi_A - \Pi_B)I \qquad \text{Equation 2-4}$$

where Π_A and Π_B are the Peltier coefficients for conductor A and B respectively and they represent how much heat is carried by a unit charge. I is the current from A to B.

The total heat at the junction can be influenced by Joule heating and thermal gradient effects in addition to the Peltier heat.

Peltier and Seebeck effects are connected through the Thomson relation:

$$\Pi = TS \qquad \text{Equation 2-5}$$

The above relation implies that in a close thermoelectric circuit the Seebeck effect will drive a current which through the Peltier effect will transfer heat from the cold to the hot junction.

Thomson effect:

Thomson effect is a reversible heating or cooling of a homogeneous conductor when there is a flow of electric current and a temperature gradient. The Seebeck coefficient of a material, usually is not constant with temperature thus if there is a spatial temperature gradient in a material will cause a gradient in the Seebeck coefficient. If a current pass through this gradient then a Peltier effect will occur. For a current density J passing through a conductor the heat production rate per unit volume is

$$\dot{q} = -\tau \bar{J} \bar{\nabla} T \qquad \text{Equation 2-6}$$

where $\bar{\nabla} T$ is the temperature gradient and τ the Thomson coefficient.

The Thomson coefficient is related with the Seebeck coefficient through the relation

$$\tau = T \frac{dS}{dT}. \qquad \text{Equation 2-7}$$

2.2 The Seebeck effect

In this section the Seebeck effect is described in more detail, since this is the effect we will study in this thesis. We can consider a metallic piece that is heated at one end and cooled at the other (Figure 2-1). The electrons at the hot end are more energetic and a diffusion of electrons from the hot end to the cold end will occur. Positive carriers accumulate in the hot region and negative in the cold region. This separation of the carriers produces an electric field and therefore a voltage difference between the cold and hot ends. However there is always a competing process. Some low energy electrons from the cold end will start diffusing in the

opposite direction. Thus the thermoelectric coefficient will depend on the balance of these two processes. The distinction may be due to a difference in rate of scattering, a difference in speeds, a difference in density of states, or a combination of these effects. The voltage difference (ΔV) created due to the temperature difference (ΔT) is the Seebeck effect. If the material comes in steady state where the current density is zero everywhere and the temperature difference ΔT between the terminals of the material is small, then as shown in the previous section the thermopower of the material is defined:

$$S = -\frac{\Delta V}{\Delta T} = -\frac{V_{left} - V_{right}}{T_{left} - T_{right}}, \qquad \text{Equation 2-8}$$

where the terms left and right refer to the left or right side of the material.

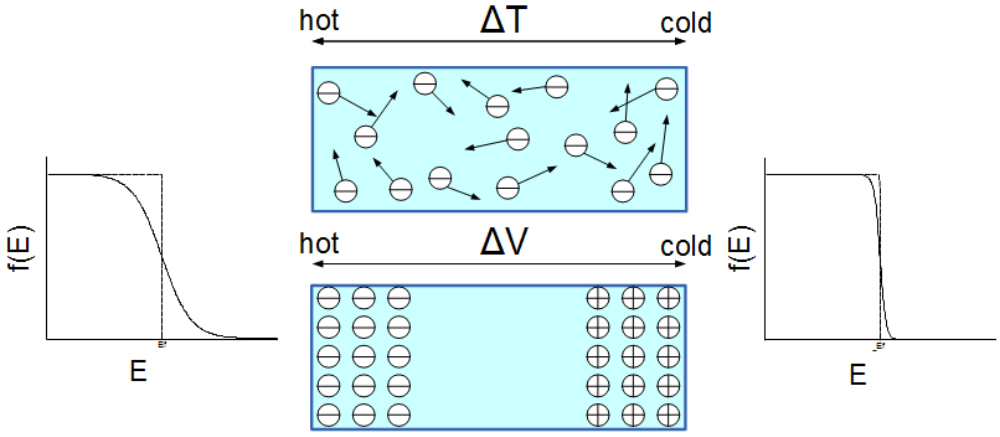

Figure 2-1: The Seebeck Effect. A temperature difference in a conductor causes a flow of the carriers, which gives rise to a potential difference. The Fermi distributions for the two different temperatures are shown [Kasap2006].

Thus, if S is positive (negative), the end with the higher temperature has the lower (higher) voltage. The voltage gradient in the material points against the temperature gradient. For metals, both electrons and holes contribute to the

thermoelectric voltage and, as a consequence, they almost cancel each other out and the S of the metals is low. Semiconductors can give high values of S, negative for n-type and positive for p-type. Thus, the sign of the thermopower tells us which carrier dominates in the material.

The Seebeck coefficient is a property of a specific material which depends on temperature, so that $S = S(T)$ and is widely referred to, as thermoelectric power or thermopower. When $S = S(T)$ is given we can calculate the voltage difference between two points of the material with temperatures T and T_0

$$\Delta V = \int_{T_0}^{T} S(T)dT. \qquad \text{Equation 2-9}$$

Let us now see the thermopower of metals in more detail. For many metals the motion of the electrons can be described independently without taking in to account scattering by lattice vibrations, impurities or crystal defects during diffusion so that the free electron model can be used to extract the Seebeck coefficient. I will follow a simplified explanation based on the free electron model of ref. [Kasap2006].

According to the free electron model for a metal with density of states $g(E) = (8\pi 2^{1/2})\left(\frac{m_e}{h^2}\right)^{3/2} E^{1/2}$ with a Fermi-Dirac distribution $(E) = \frac{1}{1+exp\left(\frac{E-E_F}{kT}\right)}$, it can be proved that the average energy per electron is given by:

$$E_{av} = \frac{3}{5}E_{F0}\left[1 + \frac{5\pi^2}{12}\left(\frac{kT}{E_{F0}}\right)^2\right], \qquad \text{Equation 2-10}$$

where E_{F0} is the Fermi energy at $T = 0K$.

According to the Fermi-Dirac distribution, at the hot end the electrons will have higher energy. That will cause their diffusion to the cold end up to the moment that a voltage difference is created. For a small temperature difference ΔT a voltage difference ΔV will be created. The work that an electron spends against the ΔV to diffuse from the hot to the cold end is given by $-e\Delta V = E_{av}(T + \Delta T) - E_{av}(T)$.

From this expression, by substituting the E_{av} and expanding $(T + \Delta T)$, we get the following for the thermopower:

$$S_{FE} = -\frac{\pi^2 k^2 T}{2eE_{F0}}, \qquad \text{Equation 2-11}$$

where S_{FE} refers to thermopower derived from free electron model.

This equation fails to calculate the sign and magnitude of the Seebeck coefficient for many metals as shown in Table 2-1 because the electrons are considered free. So their speed v and mean free path λ increase with electron energy, which is higher in the hot region, and so diffusion is always predicted to be from the hot to the cold region. In reality, the electrons are scattered by lattice vibrations, impurities or crystal defects during diffusion. A detailed theory is given by Mott which takes into account the energetics of the scattering [Mott1936]. To compare the thermopower of metals with the free electron theory we can write:

$$S_{measured} = S_{FE}x, \qquad \text{Equation 2-12}$$

where x is a numerical parameter that depends on the energy dependencies of various charge transport parameters. Some typical values of x are shown in the table and the Seebeck coefficients for different temperatures for different metals in Figure 2-2.

Table 2-1: Seebeck coefficient for different metals and comparison with the free electron model. $(x = S_{measured}/S_{FE})$

metal	S at 0 °C (μV/K)	S at 27 °C (μV/K)	x
Al	-1.6	-1.8	2.78
Au	+1.79	+1.94	-1.48
Cu	+1.7	+1.84	-1.79
K		-12.5	3.8
Li	+14		-9.7
Mg	-1.3		1.38
Na		-5	2.2
Pd	9	-9.99	
Pt	4.45	-5.28	

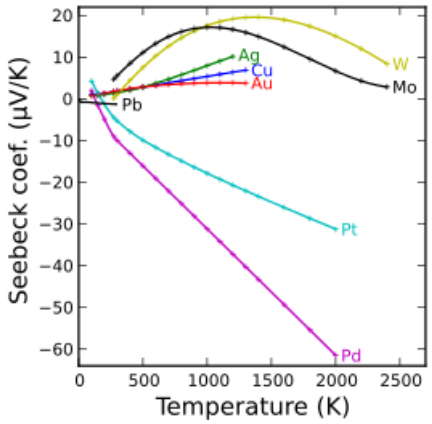

Figure 2-2: Seebeck coefficients for different metals for different temperatures. [Cusack1958].

2.3 Thermocouple

A thermocouple consists of two different metallic wires (metal A and B) connected as shown in Figure 2-3 where one junction is held at a reference temperature T_0 and the other is used as a sensor for a temperature T_1. The voltage across each metal element depends on the Seebeck coefficient so that the voltage difference between the two metals depends on their thermopower difference, $S_A - S_B$. Using Equation 2-9 we find that the voltage (V_m) we can measure between the two ends of metal B is:

$$V_m = \Delta V_A - \Delta V_B = \int_{T_0}^{T} (S_A - S_B) dT, \qquad \text{Equation 2-13}$$

Where $S_{AB} = S_A - S_B$ is the thermoelectric power of the thermocouple.

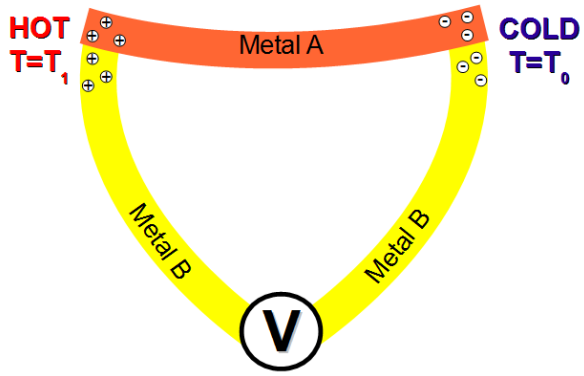

Figure 2-3: Schematic of a thermocouple. Metal A and B have different known Seebeck coefficients. A voltage between the hot and cold junction can be measured and the temperature difference can be calculated.

Thermocouples of specific materials are calibrated and are used for the estimation of the temperature difference of two points by measuring the voltage difference V_m.

2.4 Thermoelectric power generation and figure of merit

A simple model of a power generator could be a single thermocouple that consists of a positive (p-type) and a negative (n-type) branch as shown in Figure 2-4. The two branches are electrically connected at one end (connection b) and this connection is in contact with a heat supply. A resistive load is placed between the other two ends. Finally, the two branches are electrically connected in series and thermally connected in parallel. The supply of heat causes an electrical current to flow around the circuit as shown by the bold arrows in Figure 2-4 due to the Seebeck effect. In the following, notation p refers to the p-type branch and n to the n-type branch.

The field generated by the thermal electromotive force will be $E_{th} = (S_p - S_n)(T_1 - T_2)$ and this will generate a current in the circuit:

$$I = \frac{(S_p - S_n)(T_1 - T_2)}{R_p + R_n + R_L}, \qquad \text{Equation 2-14}$$

where R_p and R_n are the electrical resistances of the branches and R_L is the electrical resistance of the load. Then the power to the load, w_L, will be

$$w_L = I^2 R_L = \left[\frac{(S_p - S_n)(T_1 - T_2)}{R_p + R_n + R_L}\right]^2 R_L. \qquad \text{Equation 2-15}$$

Most of the heat is conducted to the sink through the thermocouple branches and some is lost by two main mechanisms:

1. Heat is used to balance the Peltier effect associated with the flow of current. The Peltier coefficient is given by Equation 2-4. By the use of the Equation 2-5, we can express the rate of cooling in terms of Seebeck coefficient $\dot{Q}_1 = (S_p - S_n) I T_1$.
2. Flow of heat due to the thermal conduction along the branches $\dot{Q}_2 = (K_p + K_n)(T_1 - T_2)$, where K_p and K_n are the thermal conductances of the branches.

Then the total heat flow ($\dot{Q}$) from the source is

$$\dot{Q} = \dot{Q}_1 + \dot{Q}_2 = (S_p - S_n)IT_1 + (K_p + K_n)(T_1 - T_2). \qquad \text{Equation 2-16}$$

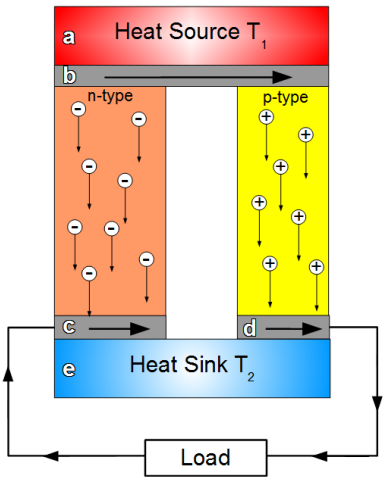

Figure 2-4: Thermoelectric Generator. A thermocouple used as a thermoelectric generator. Bold arrows show the direction of the generated current in the circuit and small arrows show the motion of the carriers due to the temperature difference in the material. Letters a-e indicate the different parts of the generator. [Winkless2012].

The efficiency is given by the relation $\eta = w_L/\dot{Q}$. The maximum efficiency can be obtained by maximizing η with respect to R_L. It can be shown that n is maximum, when the ratio of the load resistance, R_L, to the internal resistance, $R_p + R_n$, is given by:

$$\frac{R_L}{R_p + R_n} = \sqrt{1 + ZT_m}, \qquad \text{Equation 2-17}$$

where $T_m = \frac{T_1 + T_2}{2}$ and Z is the figure of merit which is given by:

$$Z = \frac{S^2 G}{K}, \qquad \text{Equation 2-18}$$

where $S = S_p - S_n$ is the thermopower, $K = K_p + K_n$ is the thermal conductance (notice that the branches are thermally connected in parallel) and $G = 1/(R_p + R_n)$ is the electrical conductance (notice that the branches are electrically connected in series) of the thermocouple. Z has dimensions of inverse temperature. It can also be expressed dimensionless as ZT at a specific temperature.

The efficiency will be

$$\eta = \frac{(T_1 - T_2)\left(\sqrt{1 + ZT_m} - 1\right)}{T_1\left(\sqrt{1 + ZT_m} + T_2/T_1\right)}. \qquad \text{Equation 2-19}$$

The efficiency n increases by increasing the Z. In order to increase the Z the quantity $(K_p + K_n)(R_p + R_n)$, that depends on the electrical resistance and thermal conductance of the material, should minimized [Goldsmid2009; Rowe2010]. Equation 2-18 implies that an efficient thermoelectric device should maximize the electrical conductance (minimize its internal resistance) and minimize the thermal conductance simultaneously so that temperature gradient will be maintained in the device. Finally, Seebeck coefficient should be maximized to ensure that coupling between thermal and electrical current is as large as possible [Bergfield2013].

In generally the figure of merit of a thermoelectric material for a specific temperature (T) is written as

$$ZT = \frac{S^2 GT}{K}, \qquad \text{Equation 2-20}$$

where K is the thermal conductance and G the electrical conductance and S the absolute thermopower of the material. K has an electrons and holes contribution (K^{el}) and a phonons contribution K^{el}, so that $K = K^{el} + K^{ph}$.

Increasing the figure of merit for a material by Increasing the electrical conductance or decreasing the thermal conductance is difficult since, in most cases, the Wiedemann-Franz law is valid, which indicates that, for a metal, the ratio of the electronic contribution of the thermal conductance to the electrical conductance is proportional to the temperature:

$$\frac{K^{el}}{G} = LT, \qquad \text{Equation 2-21}$$

where L is the Lorentz number and it is equal to $L = 2.44 \times 10^{-8}\ \mathrm{W\Omega K^{-2}}$. With any increase of the electrical conductance an increase of the thermal conductance will appear. The approach to increase the figure of merit for a thermoelectric material has been to maximize S and minimize K^{ph}.

For practical applications, $ZT > 1$ is needed. A thermoelectric material with $ZT > 4$ would be the solution for many heating and cooling problems at the nano- and macro- scale, with no operational carbon footprint. The best thermoelectric materials up to now in the laboratory have $ZT \approx 3$, while thermoelectric devices for commercial use have $ZT \approx 1$ due to various packaging and manufacturing challenges [Bergfield2010].

2.5 Thermopower at the nanoscale

Thermopower at the nanoscale changes dramatically and quantum mechanics is needed to describe the phenomena. In the following I describe the quantum mechanical approach for the thermopower at the nanoscale.

2.5.1 Thermopower of a nanojunction

The thermopower at the nanoscale can be described, in the same way as we described electronic transport, with the scattering approach. When a temperature difference is applied at the two ends of a macroscopic material, a continuous temperature gradient will be created in the material, while for a constriction between two leads, a sharp drop of the temperature will be created at the point of the constriction (see Figure 2-5). The electrons will be more energetic due to the temperature and the transport of electrons trough the constriction to the cold lead will start. Charges will start accumulating in one side of the constriction and leave

carriers of the opposite charge in the other side, and when the movement of the charges stops a Voltage ΔV difference will be created.

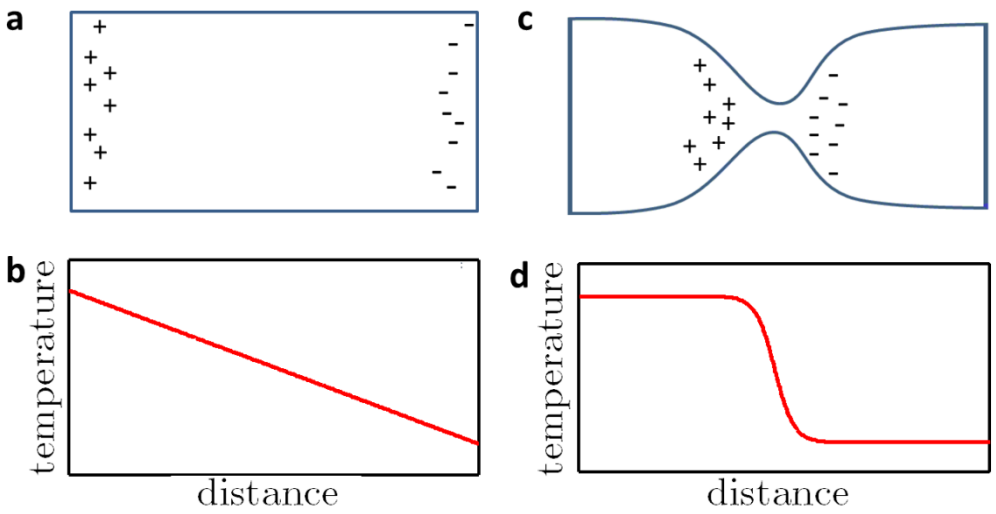

Figure 2-5: Thermopower at the macro- and nanoscale. (a,b) A different temperature at the two ends of a bulk material causes a continuous temperature gradient in the material (b) and flow of the carriers, which gives rise to a potential difference (a). (c,d) A different temperature at the two ends of a constriction causes a sharp drop of the temperature (d) and transmission of the electrons from the hot to the cold side which will give rise to a potential difference (c).

Since thermopower in nanoscale is a transport property, it is interesting to see what the relation is between the Seebeck coefficient (S) and the transmission function $T(E)$. We consider the Landauer formula:

$$I = \frac{e}{h}\sum_{n}\int_{-\infty}^{\infty} dE\; T_n(E)[f_1(E) - f_2(E)], \qquad \text{Equation 2-22}$$

We set it equal to zero since S is defined at open circuit. The difference between the distributions of the leads $(f_1(E) - f_2(E))$ is expanded with reference to contact 1.

$$0 = \frac{2e}{h}\int_{-\infty}^{\infty} dET(E)\left[\left(\frac{\partial f}{\partial \mu}\Big|_{\mu=\mu_1}\right)_{T_1} \Delta\mu_{1-2} + \left(\frac{\partial f}{\partial T}\Big|_{T=T_1}\right)_{\mu_1} \Delta T_{1-2}\right]. \qquad \text{Equation 2-23}$$

The temperature derivative is written in terms of energy $\frac{\partial f}{\partial T} = -\frac{E-\mu}{T}\frac{\partial f}{\partial E}$ and the chemical potential is approximated $\frac{\partial f}{\partial \mu} = -\frac{\partial f}{\partial E} \approx \delta(E-\mu)$. Then from Equation 2-23 we get:

$$\frac{\Delta\mu_{1-2}}{\Delta T_{1-2}} = \frac{1}{T(E)|_{E=\mu_1}}\int_{-\infty}^{\infty} dET(E)\frac{E-\mu_1}{T_1}\frac{\partial f_1}{\partial E}. \qquad \text{Equation 2-24}$$

The change in chemical potential will cause a voltage $\Delta\mu_{1-2} = -eV_{1-2}$. Then we can Taylor expand the transmission function $T(E) = T(E)|_{E=\mu_1} + (E-\mu_1)\frac{\partial T(E)}{\partial E}\Big|_{E=\mu_1}$ and using the Summerfield expansion [Ashcroft1976] we get.

$$S = \frac{V_{1-2}}{\Delta T_{1-2}} = -\frac{\pi^2 k_B^2 T}{3e}\frac{\partial[lnT(E)]}{\partial E}\Big|_{E=\mu}. \qquad \text{Equation 2-25}$$

As indicated by the Equation 2-25, the thermopower is related to the transmission function at the chemical potential of the contacts [Malen2010]. This formula is valid at low temperatures and away from transition resonances so that the variation of the transmission function is small [Dubi2011].

Thermal and electrical properties of a nanojunction can be written starting with the fundamental thermodynamic identity at constant volume ($TdS = dE - \mu dN$) and using the measurable thermoelectric coefficients: electrical conductance G, thermopower S, Peltier coefficient Π and thermal conductance κ.

$$\begin{pmatrix} \Delta V \\ \dot{Q} \end{pmatrix} = \begin{pmatrix} R & S \\ \Pi & \kappa \end{pmatrix} \begin{pmatrix} I \\ \Delta T \end{pmatrix}. \qquad \text{Equation 2-26}$$

Equation 2-26 relates the charge current I and the heat current $\dot{Q}$ with the electrical bias $\Delta V$and the temperature difference ΔT across the system. Furthermore, the thermoelectric coefficients S, G, κ and ZT can be calculated by extending the Landauer-Buttiker formalism to include both charge and heat currents in the linear temperature and bias regime. [Bergfield2009; Finch2009]

$$S = -\frac{1}{eT}\frac{L_1}{L_0}, \qquad \text{Equation 2-27}$$

$$G = \frac{2e^2}{h} L_0, \qquad \text{Equation 2-28}$$

$$\kappa = -\frac{2}{h}\frac{1}{T}\left(L_2 - \frac{L_1^2}{L_0}\right), \qquad \text{Equation 2-29}$$

$$ZT = \frac{1}{\frac{L_0 L_2}{L_1^2} - 1}, \qquad \text{Equation 2-30}$$

where

$$L_n = \int_{-\infty}^{\infty} \left(E - E_f\right)^2 T(E) \frac{\partial f(E)}{\partial E} dE. \qquad \text{Equation 2-31}$$

In nanojunctions, in linear response and at room temperature the heat current is carried mainly by electrons. For that reason usually the heat conductance (k^{ph}) due to phonons is neglected in the calculations and $k = k^{el}$ [Bergfield2010].

The high correlation of the transport of heat and current, which is higher at the nanoscale, makes the increase of the ZT very difficult. Although, due to the coherent nature of the transport in the molecular junctions systems, quantum interference phenomena could appear and give a large ZT.

2.5.2 Energy levels of the Junction vs Thermopower

The idea for the thermopower of a molecular junction is quite similar to the thermopower of a constriction. In Figure 2-6 the energy level scheme of a molecular junction is shown. In the hot side more electrons have higher energy than the Fermi energy, E_f, than in the cold side (see Fermi distribution drawn with purple line). Thus these electrons from the hot side can tunnel to the cold side through the molecular energy levels. Some electrons will tunnel back from the cold to hot but this movement will be less frequent due to the absence of empty molecular level at that energy.

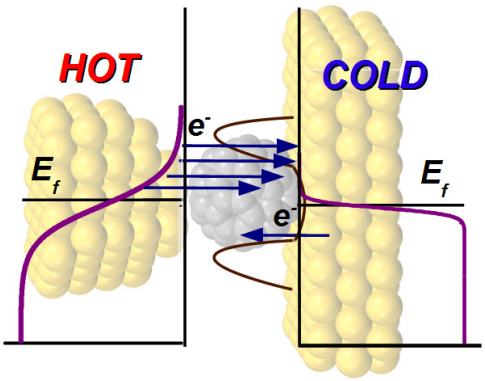

Figure 2-6: Energy level diagram of the thermopower in a molecular junction. More electrons in the hot side of the junctions have energies higher than E_F, so that they tunnel to the cold side through the empty molecular energy levels. Less electrons tunnel from the cold to the hot side due to the absence of empty molecular levels at such energies. Fermi distributions of the electrons are shown by purple line and the electrons by blue arrows.

Studying the thermopower in a molecular junction allow us to extract about where the Fermi energy is placed between the HOMO and LUMO states. We consider a Molecular Junction with HOMO and LUMO energies E_{HOMO} and E_{LUMO}, respectively. In chapter 1.4 we discussed the single-level resonant tunneling model

to describe a molecular junction which assumes that transport is dominated by a single molecular orbital. In the same way, we can use a two level model where two energy levels participate in the transport. In this model the transmission function can be modeled by two Lorenzian peaks [Paulsson2003]

$$T(E) = \frac{\Gamma_1\Gamma_2}{\Gamma^2 + (E - E_{HOMO})^2} + \frac{\Gamma_1\Gamma_2}{\Gamma^2 + (E - E_{LUMO})^2}, \quad \text{Equation 2-32}$$

where $\Gamma_1, \Gamma_2$is the level broadening due to the lead 1 and 2 respectively and $\Gamma = (\Gamma_1 + \Gamma_2)/2$.

Assuming that the Fermi energy is situated between the HOMO-LUMO levels and far from them in the weak coupling limit ($|E_F - E_{HOMO}| \gg |\Gamma_1 + \Gamma_2|$, $|E_F - E_{LUMO}| \gg |\Gamma_1 + \Gamma_2|$) we can Taylor expand Equation 2-25 in the energy around the midpoint of the HOMO-LUMO gap.

$$S = -\frac{8\pi^2 k_B^2 T}{e}\frac{1}{(E_{HOMO} - E_{LUMO})^2}\left(E_F - \frac{E_{HOMO} + E_{LUMO}}{2}\right). \quad \text{Equation 2-33}$$

This shows that the Seebeck coefficient is independent of the coupling to the contacts when the Fermi energy is situated in the middle of the HOMO-LUMO gap and depends only on the relative alignment of the energy levels while the conductance of a molecular junction depends strongly on the coupling [Yee2011].

From this simple model we can see that, for a given value of transmission between the E_{HOMO} and E_{LUMO}, there are two values of the Fermi energy which solve the Equation 2-32. Hence, from the transmission function one cannot determine the position of the Fermi energy. In contrast, one can determine the position of the Fermi energy with respect to the center of the HOMO-LUMO gap from the sign of the Thermopower. In Figure 2-7 we show an example of the electronic transmission function $T(E)$ with Fermi energy close to the LUMO or HOMO. The conductance is related with the magnitude of the $T(E)$ at the Fermi energy while the thermopower is related with the slope of the derivative of $lnT(E)$at the Fermi energy. For a LUMO dominated molecule $S < 0$ and for a HOMO dominated $S < 0$ [Yee2011].

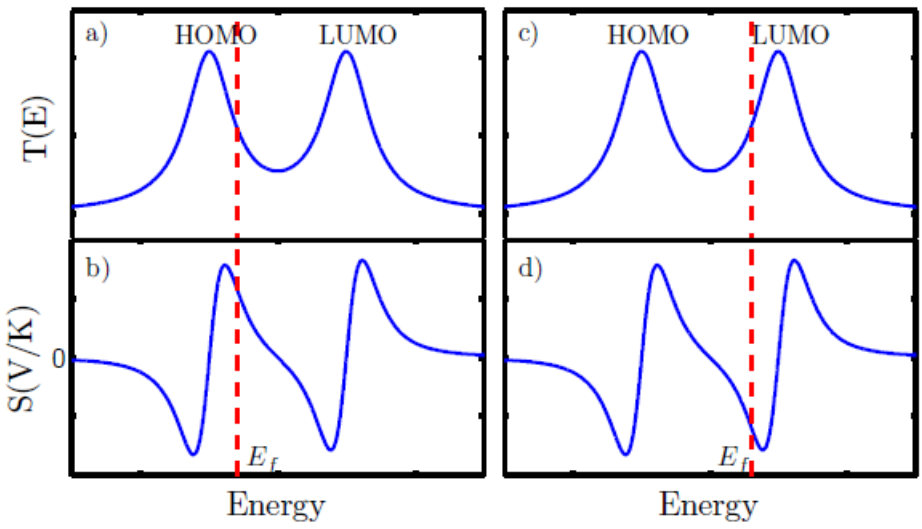

Figure 2-7: Relation of transmission function and thermopower. (a,c) Example of electronic transmission function for a molecular junction where fermi energy (green dashed line) is closer to the HOMO (a) or closer to LUMO (c). Conductance is related with the value of $T(E)$ at E_F. (b,d) Thermopower S is related to the slope of $lnT(E)$ at E_F. If E_F is closer to HOMO then $S > 0$ (b), and if E_F is closer to LUMO then $S < 0$ (d).

2.5.3 Quantum interference and thermopower

Quantum Interference phenomena often appear in molecular junctions because the transport is mainly ballistic and the wave-like (coherent) transport is dominant. These phenomena can dramatically change the electron transmission around Fermi energy and this might lead to dramatic changes of the Seebeck coefficient and that make molecular junctions good candidates for thermoelectric applications.

A simple example of interference through a molecular junction is shown in Figure 2-8a,b. The meta-connected ring gives two different transport pathways with different lengths in the molecule. The two pathways have a π-radians phase difference at energy $E = 0$, and when they combine, they interfere, causing a deep hole in the transmission spectrum at this anti-resonance (destructive interference).

In contrast, at the para linkage, the two pathways have the same length and they show constructive interference. As a consequence, the molecule with para linkage conducts better than the one with meta. On the other hand, while the thermopower S is proportional to the derivative of the transmission, a dramatic enhancement will occur, which will give rise to bigger values of the figure of merit ZT [Bergfield2013].

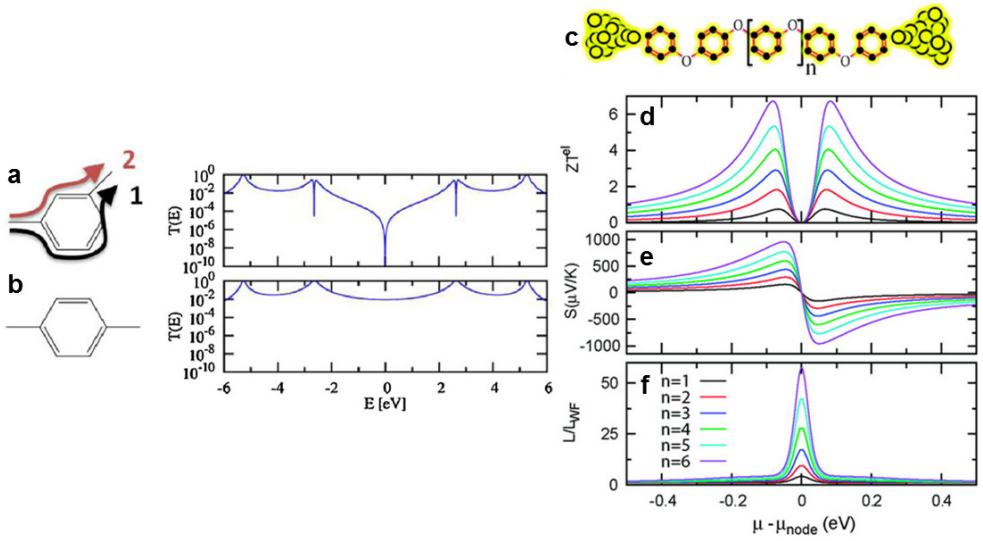

Figure 2-8: Quantum interference in molecular junctions. (a,b) The calculated transmission function through the two cyclic molecules is shown. The archetypal meta (a) and para (b) configured benzene junctions show destructive and constructive interference, respectively, at the mid-gap energy. [Bergfield2013]. (c-f) Enhancement of ZT (d), thermopower S (e), and Lorenz number L (f) for polyphenyl ether (PPE) SMJs with n repeated phenyl groups (c) [Bergfield2009].

In Figure 2-8c-f an example is given for a meta-connected ring. This molecule has midgap nodes in its transmission probability due to interference. Thermopower is increased close to the transmission node (Figure 2-8e) and Lorenz number is increased at the transmission node (Figure 2-8f). As a consequence, the figure of merit increases close to the nodes (Figure 2-8d) [Bergfield2010].

References

[Ashcroft1976] Ashcroft, N. W. and N. D. Mermin (1976). Solid state physics, Saunders College.

[Bergfield2013] Bergfield, J. P. and M. A. Ratner (2013). "Forty years of molecular electronics: Non-equilibrium heat and charge transport at the nanoscale." physica status solidi (b) **250**(11): 2249-2266.

[Bergfield2010] Bergfield, J. P., M. A. Solis and C. A. Stafford (2010). "Giant Thermoelectric Effect from Transmission Supernodes." ACS Nano **4**(9): 5314-5320.

[Bergfield2009] Bergfield, J. P. and C. A. Stafford (2009). "Thermoelectric Signatures of Coherent Transport in Single-Molecule Heterojunctions." Nano Letters **9**(8): 3072-3076.

[Cusack1958] Cusack, N. and P. Kendall (1958). "The Absolute Scale of Thermoelectric Power at High Temperature." Proceedings of the Physical Society (1960) **72**(5): 898-901.

[Dresselhaus2001] Dresselhaus, M. S. (2001). SOLID STATE PHYSICS Transport Properties of Solids.

[Dubi2011] Dubi, Y. and M. Di Ventra (2011). "Colloquium: Heat flow and thermoelectricity in atomic and molecular junctions." Reviews of Modern Physics **83**(1): 131-155.

[Finch2009] Finch, C. M., V. M. García-Suárez and C. J. Lambert (2009). "Giant thermopower and figure of merit in single-molecule devices." Physical Review B **79**(3): 033405.

[Goldsmid2009] Goldsmid, H. J. (2009). Introduction to Thermoelectricity, Springer.

[Kasap2006] Kasap, S. O. (2006). Principles of Electronic Materials and Devices, McGraw-Hill Education.

[Malen2010] Malen, J. A., S. K. Yee, A. Majumdar and R. A. Segalman (2010). "Fundamentals of energy transport, energy conversion, and thermal properties in organic–inorganic heterojunctions." Chemical Physics Letters **491**(4–6): 109-122.

[Mott1936] Mott, N. F. and H. Jones (1936). The Theory of the Properties of Metals and Alloys, Clarendon Press.

[Paulsson2003] Paulsson, M. and S. Datta (2003). "Thermoelectric effect in molecular electronics." Physical Review B **67**(24): 241403.

[Rowe2010] Rowe, D. M. (2010). CRC Handbook of Thermoelectrics, Taylor & Francis.

[Winkless2012] Winkless, L. (2012). "Thermoelectric Generators - TEGs." from http://www.thenakedscientists.com/HTML/articles/article/thermoelectric-generators/.

[Yee2011] Yee, S. K., J. A. Malen, A. Majumdar and R. A. Segalman (2011). "Thermoelectricity in Fullerene–Metal Heterojunctions." Nano Letters **11**(10): 4089-4094.

Experimental Tools

In this chapter I will describe the two homebuilt Scanning Tunneling Microscopes used to obtain the results presented in this thesis: the Room Temperature STM (RT STM) and the Low Temperature STM (LT STM). The two setups were modified and partially re-built in order to adapt them for the desired experiments.

3.1 Functioning of the Scanning Tunneling Microscope

The Scanning Tunneling Microscope (STM) was the experimental tool that caused the big breakthrough in Nanotechnology in the last 30 years. In 1981 G.Binning, H.Rohrer, Ch. Gerber and E. Weibel observed vacuum tunneling between a tungsten tip and a platinum sample [Binnig1982]. This observation, combined with the ability of scanning using piezoelectric elements, generated the STM. In 1986 the first two were awarded the Nobel Prize in Physics. The STM is a powerful instrument which gives many possibilities of investigating physical phenomena at the nanoscale. The surface structure of conducting and semiconducting materials can be scanned with atomic resolution. In addition, the tip acts as a probe giving the opportunity to explore physical properties of the materials at the atomic scale by using different spectroscopic techniques.

The idea of the STM is quite simple and is based on the quantum tunneling effect. A bias voltage is applied between a sharp tip and the sample. Both sample and tip should be conducting or semiconducting. As the tip approaches the sample a

current flow appears between the apex of the tip and locally on the sample due to the quantum tunneling effect.

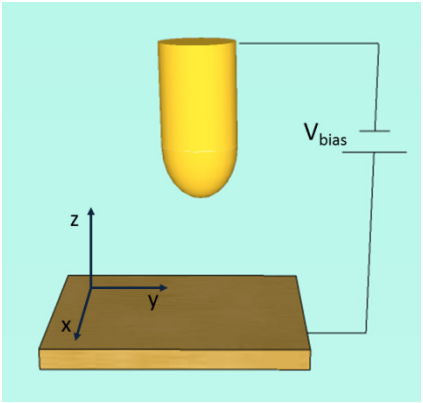

Figure 3-1: The basic principle of STM function. A bias voltage is applied between the tip and the sample. The tip can move in the x, y, z direction and the distance between the tip and the sample is controlled by a feedback loop.

By keeping the tunneling current constant by means of a feedback loop, and scanning the surface along the x and y axes we can record the z movement and create a 3D local mapping of the surface (Figure 3-2a). The adjustment of the vertical height is performed by applying voltage (V_z) at the z piezoelectric drive, and the lateral tip position is determined by the voltages V_x, V_y applied on the x and y piezoelectric drive respectively. Finally, the recorded signal $V_z(V_x, V_y)$, can give the topographic image $z(x, y)$ if the calibration of the piezoelectric drive is known.

The feedback loop has a finite response which limits the speed of scanning in the constant current mode. A way to avoid that is the constant height imaging (Figure 3-2b) where the feedback loop is switched off. The vertical tip/sample distance is kept constant and the tunneling current is recorded while scanning in the x, y direction. The high sensitivity of the tunneling current, due to the exponential dependence on the tip/surface distance, will give the topography of the surface [Wiesendanger1994].

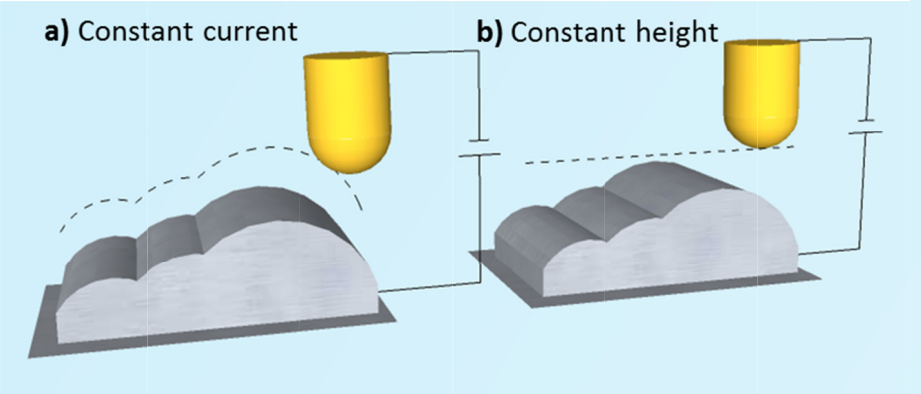

Figure 3-2: The two scanning modes of a STM. (a) Constant current mode, the current between the tip and the sample is kept constant while scanning. (b) Constant height mode, the tip is kept at a certain height from the surface while scanning.

3.2 Room temperature STM

Our Room Temperature (RT) STM was our main tool used for the experiments. This STM offers high stability and very low drift (few Angstroms per min). It has a scanning range of $(1 \times 1\ \mu m)$. It consists of 3 parts made out of brass; the support table, the body and the head of the STM. The piezotube (PZT) is glued with epoxy (Stycast) on the head of the STM. At the end of the PZT a flat disk with central nut is fixed, where the tip holder can be screwed on. The head is then placed on the body which is placed on the table on top of three vertical supports responsible for the vertical coarse mechanical movement. One metallic sphere is placed on top of each of the three supports, and they fit into the notches of the body, for better stability. The coarse movement of the head is needed to move the tip toward the sample which is on the table. Three screws are responsible for the mechanical vertical movement of the supports. Two of them are controlled manually and the third is controlled by an electrical motor for better precision. The symmetric geometry of this STM is what gives the high stability and the very low thermal drift (see Appendix B).

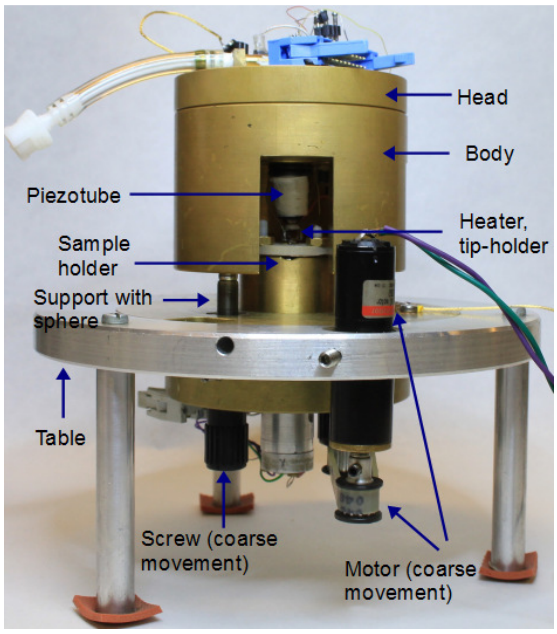

Figure 3-3: The Room temperature STM used for the experiments.

3.2.1 The piezotube

The piezoelectric element is responsible for the control of the fine movement of the tip of the STM. At the (RT) STM the piezoelectric element is a piezotube (PZT), which is a monolithic actuator contracting longitudinally when a voltage is applied at the inner and outer electrodes. The outer part is separated into four quadrants ($\pm x, \pm y$) which are connected to four different electrodes while the inner part of the tube is connected to a fifth electrode.

To bend the tube, a voltage is applied to a quadrant, so that it expands and another opposite voltage is applied to the opposite quadrant which is contracted. The global effect is to bend the tube, while when a voltage is applied at the inner electrode causes expansion and compression. By fixing the tip on the end of the PZT and applying voltage at the appropriate electrode the piezotube bends, expands and compress, so that the tip moves in the x, y, z direction. For details about the PZT calibration see the Appendix A.

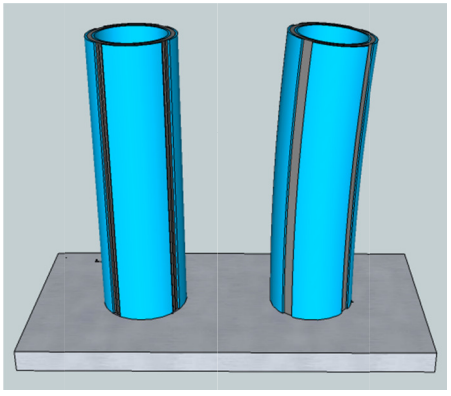

Figure 3-4: Schematics of the piezotube. The piezotube in the initial vertical position and the laterally bent position.

3.2.2 Tip holder and the heater

At the end of the PZT, a flat disk with central nut is glued, where we can screw on the tip holder. The tip holder is simply a screw where, on its head, the tip is soldered (see Figure 3-5a,b). We built in addition, a second holder with incorporated heater (see Figure 3-5c). The heater was used in our experiments in order to heat the tip and establish a temperature difference between the tip and the sample. This allowed us to measure the thermopower of nanojunctions.

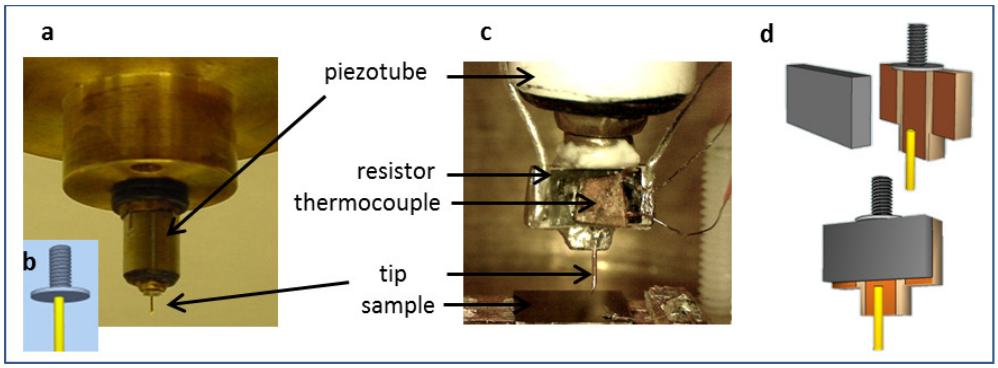

Figure 3-5: Tip holders of the STM. (a) Photo of the piezotube with the tip-holder of the STM. (b) Schematic of the tip-holder (c) Photo of the tip-holder with incorporated heater. (d) Schematic of the different parts of the tip holder with incorporated heater.

The tip holder with the incorporated heater consists of a non-electrical and thermal insulating substrate, with 3 strips of copper sheets laminated onto it, attached to a screw (see Figure 3-5d). The middle strip is used for mounting the tip and the other two as electrical contacts for the surface mounted 1kOhm resistor. In this way the resistor which acts as a heater is thermally attached to the middle strip and thus to the tip. In addition, a thermocouple is glued exactly where the tip is soldered on the tip holder or on the resistor to monitor the temperature (see Appendix C for details on the temperature calibration).

3.2.3 STM electronics

In Figure 3-6a schematic of the electronics of the RT STM is shown. The STM is controlled by a computer through a multifunctional card, NI PCI-7833R, with 8 analogue inputs, 8 analogue outputs and an FPGA module. The analogue inputs read all the necessary signals from the STM and the analogue outputs provide the signals for controlling the piezotube. The control signals for the piezotube are amplified by a Nanonis HVA4 high voltage amplifier. The feedback loop that controls the tip-sample distance is digitally implemented in the FPGA module of the NI PCI-7833R card, which receives the tunneling signal from a current amplifier.

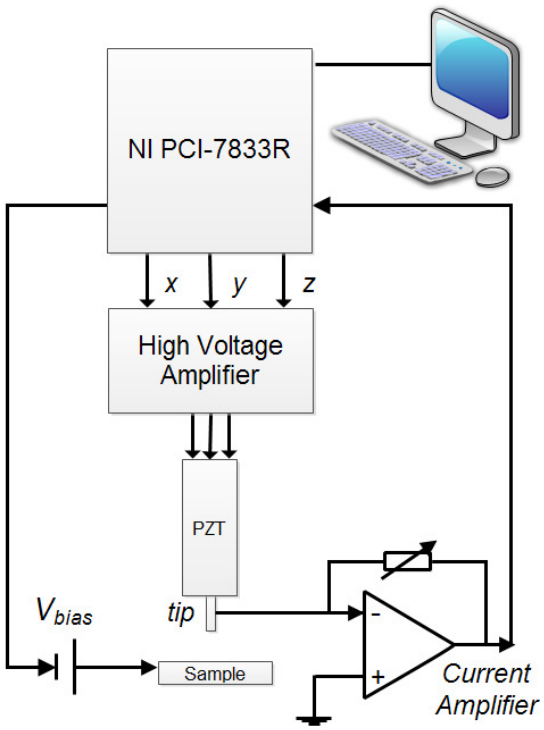

Figure 3-6: Schematics of the function of a STM.

3.2.4 Current to voltage amplifier

A very important part of the electronics of an STM is the current to voltage amplifier (current amplifier), which amplifies the current signal of the STM and converts it to a voltage. In the following experiments we used 3 different current to voltage amplifiers:

1. Homebuilt, two-channel current amplifier, which amplifies the current signal in two stages (Figure 3-7a)
2. One-channel current amplifier with variable gain (10^4-$10^9\Omega$) built in the workshop of Universidad Autonoma de Madrid (SEGAINVEX) (Figure 3-7b)
3. Keithley 428 one-channel current amplifier with variable gain (10^3-$10^9\Omega$)

The two-channel current amplifier has the advantage of recording the current value in a wide range (6 orders of magnitude). The one-channel amplifiers give the advantage of higher speed, more stability and less noise in the measurements.

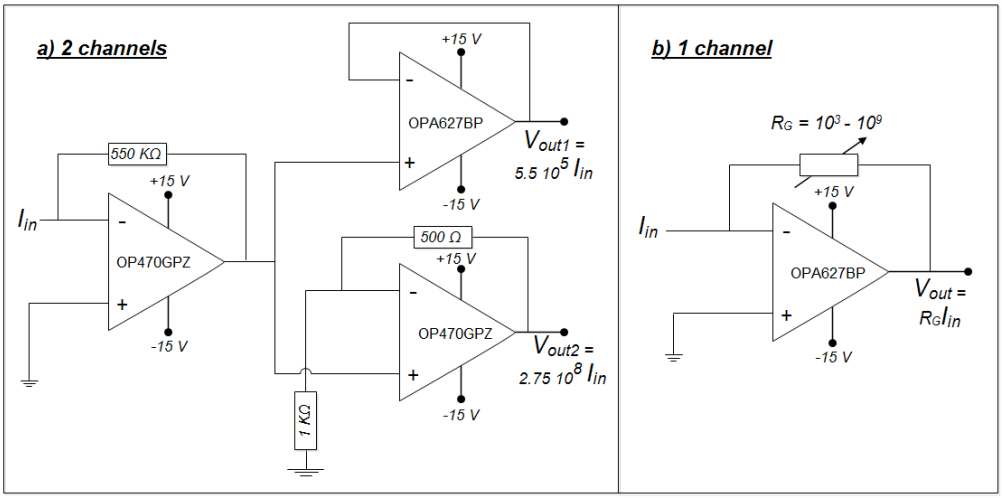

Figure 3-7: Circuits of the current amplifiers used in the experiments. (a) Two-channel current amplifier: the current is amplified and then is directed to another amplifier and a buffer (b) One-channel current amplifier: the input current is amplified with a variable gain amplifier.

3.3 Low temperature STM

Some of the results of this thesis were obtained at room temperature by the homebuilt Low temperature STM. This STM is designed to function at low temperatures. It is less stable and has more drift than the RT STM. It is a compact STM made of titanium and relatively smaller than the Room Temperature one. It is mainly composed of three parts; the STM body, the slider where the tip is fixed and the $x - y$ table where the sample is placed.

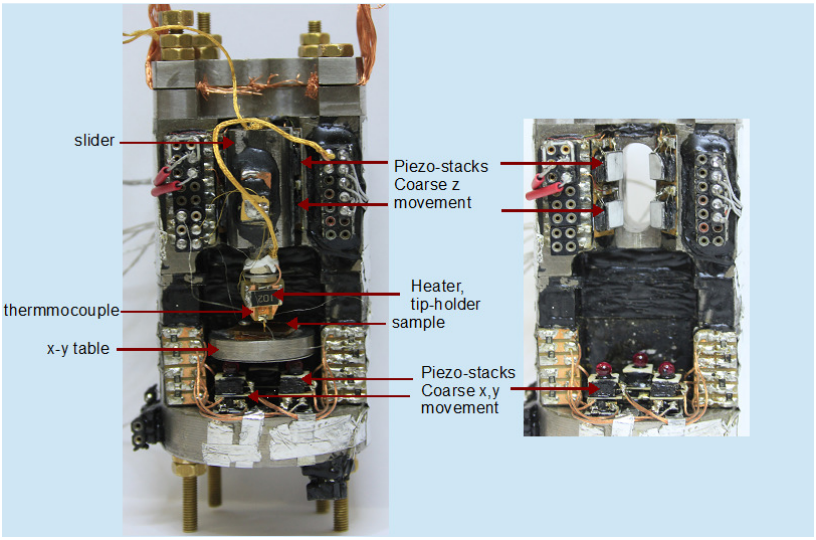

Figure 3-8: The Low Temperature STM used for the experiments.

A mobile slider is held against four piezo stacks with an adjustable spring. In addition, a piezotube responsible for the fine movement of the tip, is placed on the slider. The four piezo stacks are responsible for the vertical coarse and fine movement of the tip, using the stick-slip motion. As in the RT STM at the end of the piezotube, one flat disk with central nut is glued, where we can screw on the tip holder. In this way, by keeping the same configuration in both the RT STM and the

LT STM, we can adjust the same tip holders on both (one with incorporated heater and one without).

The $x - y$ table is a mobile disk with an alumina lamina glued on its base and it's held against the piezo stacks with an adjustable spring. Each stack is composed of a pair of piezostacks oriented in the x and y direction, and they are responsible for the coarse and fine movement in the x and y direction.

Each piezo stack is built up from four piezoelectric plates and copper sheets in between them glued by silver epoxy. On top of each piezo stack, an alumina lamina has been glued by epoxy (Stycast). Additionally, for the $x - y$ stacks, a small sphere is glued on top of the alumina for a more stable contact with the xy table. In our experiments we used the piezo-stacks to control the $x - y - z$ coarse movement and the piezotube for the $x - y - z$ fine movement.

A detailed description of the specific STM and the function of the piezo-stacks is already presented in ref. [Arroyo2010]. We did not change the metallic parts but we had rebuilt the piezo-electric elements.

References

[Arroyo2010] Arroyo, C. (2010). Electron transport and phonons in atomic wires and single molecule junctions.

[Binnig1982] Binnig, G., H. Rohrer, C. Gerber and E. Weibel (1982). "Tunneling through a controllable vacuum gap." Applied Physics Letters **40**(2): 178-180.

[Wiesendanger1994] Wiesendanger, R. (1994). Scanning Probe Microscopy and Spectroscopy: Methods and Applications, Cambridge University Press.

Simultaneous Thermopower and Conductance Measurement Technique

The characterization of a junction at the molecular or atomic level requires monitoring of its conductance during formation and subsequent breaking. In this thesis we developed a novel technique for measuring thermopower in nanoscale junctions which, in contrast to previously reported techniques, allows for the simultaneous measurement of thermopower and conductance.

4.1 Introduction

A complete characterization of a nanojunction (molecular junction or metallic atomic contacts) needs the conductance (G) to be measured during the whole evolution of the junction. The most used STM based technique up to now is STM Break-Junction technique demonstrated by N.J. Tao [Xu2003] which is based on the technique for atomic metallic contacts [Agraït1993]. In this technique the STM tip is driven in and out of contact with a substrate covered with molecules. Tip and substrate material is usually gold. Once the contact between tip and surface is made, the tip is withdrawn, and the conductance is recorded (Figure 4-1a). One or more molecules that are present, may bind at both the tip and the sample, and when the metallic contact breaks, the main charge transport pathway across the junction will be through the one or more molecules. This results in a conductance plateau in the $G - z$ (z is the tip movement in the vertical direction) trace upon

further separation of the electrodes (Figure 4-1c). If no molecules bind then the $G - z$ curves show an exponential dependence (Figure 4-1e). In this technique there is always an uncertainty about the number of molecules participating in the junction, so that histograms of conductance are needed to be plotted in order to get the most probable value for the conductance (see conductance histograms Figure 4-1b,d,f for the cases described above).

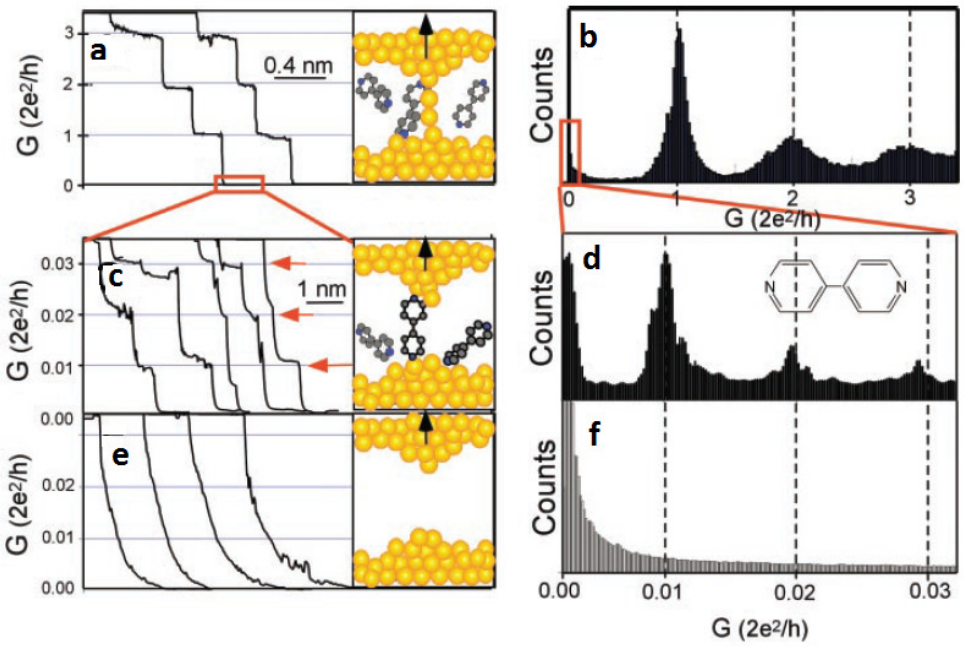

Figure 4-1: STM Break Junction technique as presented by Tao. [Xu2003].(a) Conductance of a gold contact formed between a gold STM tip and a gold substrate decreases in quantum steps near multiples of G_0 as the tip is pulled away from the substrate. (b) A corresponding conductance histogram constructed from 1000 conductance curves. (c) When the contact shown in (a) is completely broken, corresponding to the collapse of the last quantum step, a new series of conductance steps appears if molecules such as are present. These steps are due to the formation of the stable molecular junction between the tip and the substrate electrodes. (d) A conductance histogram obtained from 1000 measurements as shown in (c). (e,f) In the absence of molecules, no such steps or peaks are observed within the same conductance range.

The experimental techniques for measuring the thermopower in molecular junctions reported up to now are usually implemented in the STM-BJ technique. Reddy et al. used the modified STM setup shown in Figure 4-2a. When the tip approaches the hot Au-substrate with the molecules deposited on it, a tip-substrate bias voltage is applied and the conductance is monitored continuously. When the conductance reaches a preset threshold of high conductance, the bias voltage and the current amplifier are disconnected, the tip is grounded and a voltage amplifier is connected. Then the tip is retracted to a large distance while the output voltage of the junction is monitored but the conductance is not. During retraction, if a molecule is trapped between the tip and the substrate with a temperature difference ΔT, a thermoelectric voltage ΔV is expected to be generated. They firstly studied the length dependence of thermopower of benzenedithiol (BDT) molecules with one two and three units, and they found an increase with length [Reddy2007]. Then they studied how thermopower is affected with the chemical composition, by modifying the 1,4-benzenedithiol (BDT) molecule by the addition of electron-withdrawing or -donating groups [Baheti2008]. They also studied the effect on the thermopower by varying the position of intramolecular energy levels relative to the work function of metallic electrodes [Yee2011].

Venkataraman et al. on the other hand, measured the thermopower at one specific point during the evolution of the junction while conductance is being recorded. The tip is brought in contact with the heated Au-substrate where the molecules are deposited while the conductance is monitored. The tip is then withdrawn to a preset distance where it remains for some time and then further retracted. During the whole cycle the current and the voltage of the junction are continuously measured. For a time interval, within the period when the tip-substrate distance is constant, the bias voltage is set to zero. If a molecule is trapped between the tip and the substrate a thermoelectric voltage will appear. The current before and after this time interval should be similar in order to prove that the molecule was wired. They used thermopower as a tool for determining whether the transport of the molecules is HOMO or LUMO dominated [Widawsky2011]. They investigated the molecular length dependence of the thermopower as well, with the use of trimethylstannylmethyl-terminated oligophenyls with 1−4phenyl rings and trimethylstannyl terminated alkanes [Widawsky2013].

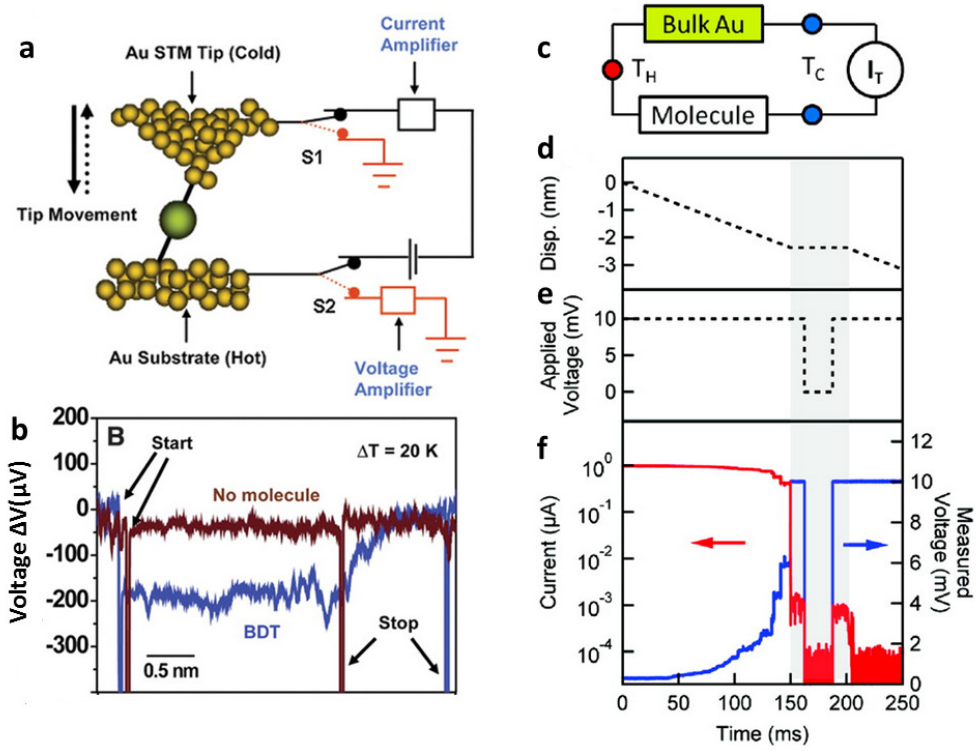

Figure 4-2: Techniques reported for measuring the thermopower of molecular junctions. (a,b) Description of the technique used by Reddy et.al to measure thermopower [Reddy2007]: (a) Schematic of the experimental setup. When the conductance reaches a threshold, the voltage bias and the current amplifier are disconnected. A voltage amplifier is then used to measure the induced thermoelectric voltage, ΔV, and the tip is gradually pulled away from the substrate. (b) A plot of the thermoelectric voltage measured as a function of the tip-sample distance when a temperature differential $\Delta T = 20\,\mathrm{K}$ is applied for a BDT molecule. The red curve shows a control experiment performed on a clean gold substrate. (c-f) Description of the technique used by Venkataraman et.al to measure thermopower [Widawsky2011]: (c) Diagram illustrating measurement of thermoelectric current (d) Piezo ramp used, including a "hold" portion between 150 and 200 ms. (e) External applied voltage across the leads which drops to zero during the center of the "hold" portion. (f) Sample trace. The measured current is shown in red and the voltage measured across the junction is shown in blue.

The above techniques measure the thermopower of molecular junctions but they don't succeed in monitoring the conductance and the thermopower simultaneously during the whole evolution of the junction. In Reddy's technique the conductance

and the thermopower are not measured in the same junction, while in Vencataraman's technique they are, but the thermopower is measured just at one point of the junction. In contrast to these previous experiments, we developed a new technique that makes possible to measure thermopower and conductance simultaneously during the whole evolution of the molecular junction. The technique is described in the following section.

4.2 The technique

A temperature difference between the tip and the substrate is established by heating the tip and keeping the substrate at room temperature (further information about heating the tip can be found in Appendix C). The temperature stabilizes after 15 minutes while the minimization of the drift takes several hours. During an approach-retraction cycle of the tip (see Figure 4-3a-c) the bias voltage is maintained at a fixed value V_{bias} and every few picometers the tip motion stops (see Figure 4-3e) and the voltage is swept between $\pm\Delta V_0$ (Figure 4-3f). In each closing-opening cycle, several hundred current versus voltage curves, or $I-V$ curves, are acquired. The corresponding $I-V$ curves, show a Temperature-dependent thermal voltage V_{th} (see Figure 4-3g).

When a temperature difference ΔT is applied across the material, an electric potential difference $\Delta V = -S\Delta T$ appears in response (Seebeck effect), where S is the Seebeck coefficient. The thermovoltage V_{th}, consists of a contribution from the junction $S(T_h - T_c)$ and a contribution from the tip-connecting lead $S_{lead}(T_c - T_h)$, where S and S_{lead} are the thermopower of the junction and the lead, respectively.

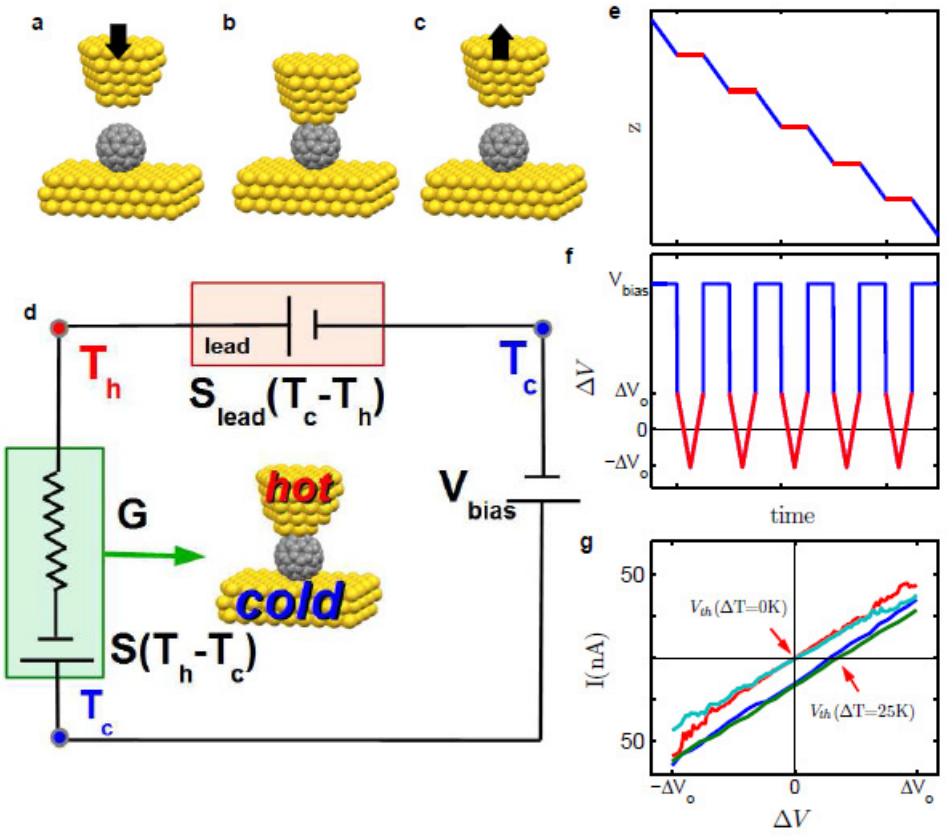

Figure 4-3: Simultaneous thermopower and conductance measurements technique. (a-c) schematic representation of an approach-retraction cycle on a C_{60} isolated molecule. With black arrows the direction of the tip movement is demonstrated. (d) Equivalent thermal circuit of the setup for the calculation of the thermopower. The substrate and body of the STM are at ambient Temperature T_c while the tip is heated to a temperature of $T_h = T_c + \Delta T$ above ambient temperature. S is the thermopower of the molecular junction and S_{lead} is the thermopower of the tip connecting lead. V_{bias} is the bias voltage imposed by the control electronics of the STM. (e,f) Tip displacement z and applied bias voltage ΔV, respectively, as a function of time. The bias voltage is maintained at a fixed value V_{bias} during the tip motion and every few picometers it is swept between $\pm\Delta V_0$ while the tip is stationary. (g) Experimental $I-V$ curves acquired on C_{60} molecule showing the thermal voltage due to the temperature difference.

Considering the equivalent circuit (Figure 4-3d), we can write:

$$\frac{I}{G} = V_{bias} - V_{th} = V_{bias} - S(T_h - T_c) - S_{lead}(T_c - T_h) \\ = V_{bias} - S\Delta T + S_{lead}\Delta T, \qquad \text{Equation 4-1}$$

where V_{bias} is the bias voltage, T_c is the temperature of the sample and $T_h = T_c + \Delta T$ is the temperature of the tip.

Taking into account that when $V_{bias} = V_{th}$ the current vanishes, and from Equation 4-1 we can write

$$V_{th} = -S\Delta T + S_{lead}\Delta T = -(S - S_{lead})\Delta T. \qquad \text{Equation 4-2}$$

Thus by measuring an $I - V$ curve, we can obtain simultaneously the thermopower S and the conductance G: the zero crossing yields V_{th} (and thence we can obtain S) and the slope gives G. Further information for the estimation of S_{lead} value can be found in Appendix D.

4.3 Thermopower circuit -voltage offsets

The magnitude the thermopower we want to measure is very small and consequently a dynamical calibration of the electronics is required. Various electronical offsets have a tendency to drift in time during the experiment. Here we describe the offsets appearing and the calibration procedure.

- The bias voltage offset (V_a): the bias voltage is applied by a digital-to-analogue converter (DAC), which has a small offset.
- The current amplifier input offset voltage (V_e): voltage offset in the STM current circuit due to the current amplifier whose virtual ground is not exactly at zero volts.

- Current offset (I_{off}): Offset in the current measured at the output of the Op-Amp when $V = 0$ V are applied to the inputs because of the output offset Voltage ($V_{oc} = -R_G I_{off}$) [Terrell1996].

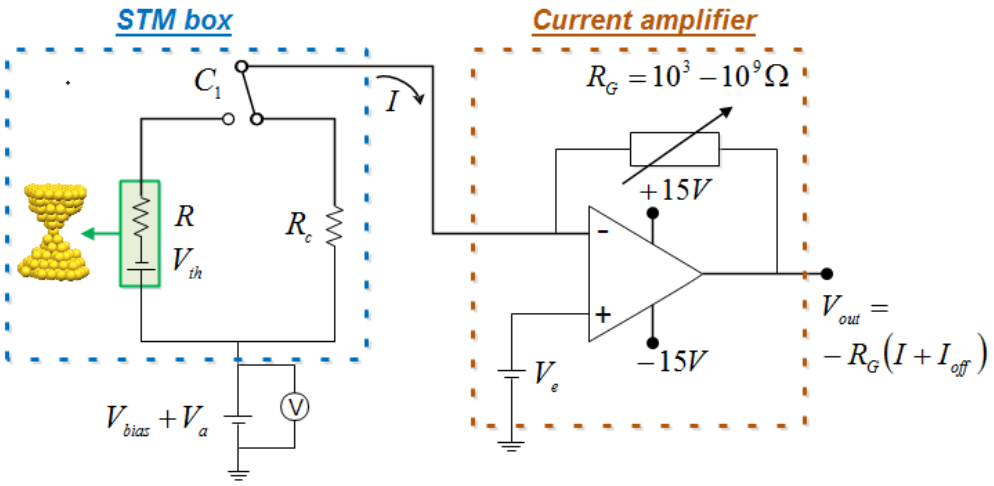

Figure 4-4: Effective circuit of the STM. Within the blue dashed line is the junction and within the brown dashed line, the current amplifier. The offset V_e and the thermovoltage $V_{th} = (S - S_{lead})\Delta T$ are drawn as voltage sources and the direction of the current I is indicated with an arrow.

We consider the effective circuit of Figure 4-4 where the offset V_e and the thermovoltage $V_{th} = (S - S_{lead})\Delta T$ are drawn as voltage sources for simplicity. The Equation 4-1 can be written:

$$\frac{I}{G} = V_{bias} + V_a - V_{th} - V_e. \qquad \text{Equation 4-3}$$

The condition $I = 0$ implies that the thermovoltage is given by

$$V_{th} = V_{bias} + V_a - V_e. \qquad \text{Equation 4-4}$$

V_a is directly measured with a voltmeter (see Figure 4-4) at the end of every approach-retraction cycle.

The current offset (I_{off}) is measured at the end of every approach-retraction cycle by retracting the tip far enough from the substrate, so that tunneling current, I, is zero.

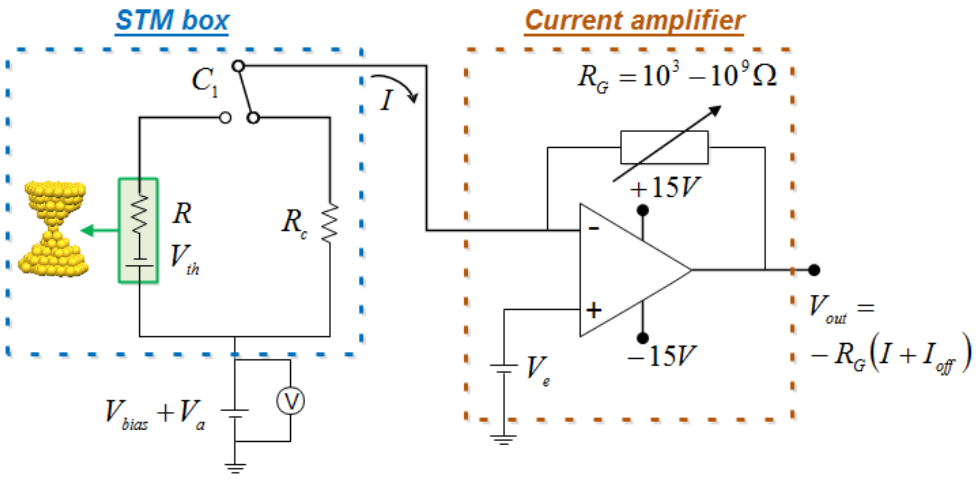

Figure 4-5: Configuration for measuring the offset V_e. Within the blue dashed line are the junction and the circuit of a known resistor, inside the STM box. Within the brown dashed line is the current amplifier. With switch C_1 we can switch the input of the current amplifier from the junction to the resistor.

To obtain V_e we switch using C_1 (see Figure 4-5) from the junction to a known resistor $R_c = 1/G_c$. In this case we have

$$IR_c = V_{bias} + V_a - V_e \,. \qquad \text{Equation 4-5}$$

By setting $V_{bias} = 0$ V we get

$$V_e = V_a - IR_c \,.^{1} \qquad \text{Equation 4-6}$$

[1] $V_{out} = -R_G(I + I_{off}) = -R_G\left(I + {}^{V_{oc}}/_{R_G}\right) \Rightarrow I = (V_{oc} - V_{out})/R_G$

The resistor should be of similar value to the resistance of the junction being measured and is installed inside the STM box in parallel to the STM-circuit. We switch to the known resistor and measure the current amplifier input offset voltage, V_e, at the end of every 50-100 approach-retraction cycles.

As shown above the electronical offsets are related to the operational amplifier (Op-Amp) of the current to voltage amplifier. In order to minimize these offsets is better using a one channel current amplifier which just uses one Op-Amp in contrast to the two channel current amplifier which uses two Op-Amps. For further information for the Op-Amps see Appendix E.

References

[Agraït1993] Agraït, N., J. G. Rodrigo and S. Vieira (1993). "Conductance steps and quantization in atomic-size contacts." Physical Review B **47**(18): 12345-12348.

[Baheti2008] Baheti, K., J. A. Malen, P. Doak, P. Reddy, S.-Y. Jang, et al. (2008). "Probing the Chemistry of Molecular Heterojunctions Using Thermoelectricity." Nano Letters **8**(2): 715-719.

[Reddy2007] Reddy, P., S.-Y. Jang, R. A. Segalman and A. Majumdar (2007). "Thermoelectricity in Molecular Junctions." Science **315**(5818): 1568-1571.

[Terrell1996] Terrell, D. (1996). Op Amps: Design, Application, and Troubleshooting: Design, Application, and Troubleshooting, Elsevier Science.

[Widawsky2013] Widawsky, J. R., W. Chen, H. Vázquez, T. Kim, R. Breslow, et al. (2013). "Length-Dependent Thermopower of Highly Conducting Au–C Bonded Single Molecule Junctions." Nano Letters **13**(6): 2889-2894.

[Widawsky2011] Widawsky, J. R., P. Darancet, J. B. Neaton and L. Venkataraman (2011). "Simultaneous Determination of Conductance and Thermopower of Single Molecule Junctions." Nano Letters **12**(1): 354-358.

[Xu2003] Xu, B. and N. J. Tao (2003). "Measurement of Single-Molecule Resistance by Repeated Formation of Molecular Junctions." Science **301**(5637): 1221-1223.

[Yee2011] Yee, S. K., J. A. Malen, A. Majumdar and R. A. Segalman (2011). "Thermoelectricity in Fullerene–Metal Heterojunctions." Nano Letters **11**(10): 4089-4094.

Part II: Experimental Results

5 Engineering the Thermopower of Fullerene Molecular Junctions

In this chapter we investigate the thermoelectrical properties of C_{60} molecular junctions at room temperature in ambient conditions. C_{60} is a promising candidate for future electronic devices due to its physical properties - mainly its electron-acceptor capability [Guldi2000; Langa2007]. Electronic properties of C_{60}, mostly on Cu substrates, have been widely studied with STM, especially in low temperatures and ultrahigh vacuum; however, its thermoelectric properties remain largely unexplored. In the first section of this chapter we characterize single- and double-C_{60} junctions. The second section focuses on the thermopower measurements of these junctions and demonstrates the possibility of engineering the thermopower of a molecular junction by nanoscale manipulations.

5.1 Conductance characterization of single- and double-C_{60} junctions

Since the first reported conductance measurements of molecular junctions [Xu2003] the electronic transport trough molecules and the way that it is affected by different factors have been studied extensively. For example the dependence of conductance with conjugation variations (eg. OPE-OPV) [Huber2007], with the differennt ancoring groups used to bind the metalic contacts (eg. Alkanes families) [Arroyo2011; Cheng2011], with the length [Moreno-García2013] and with the

oxidation state [Chen2005]. In all these studies the STM Break-Junction technique and the Mecanically Controlled Break Junction (MCBJ) technique have been used [van Ruitenbeek1996]. However, using the break-junction techniques it remains difficult to wire precisely one molecule, due to the lack of imaging possibilities and the large number of molecules close to the junction. Thus, the conductance can vary significantly from one junction to the next, and no obvious way exists to differentiate one-molecule from multi-molecule related effects [Songmei2008; Reuter2011; Reuter2012]. Statistics are required to obtain a most probable conductance value from such measurements which may correspond to more than one wired molecule [Arroyo2011] [French2012].

C_{60} is a relatively large molecule and that makes it possible to image it with STM when deposited on metallic surface. Single pristine C_{60} molecules contacted between metallic contacts have been fairly extensively studied on gold [Joachim1995] and copper substrates [Néel2007; Néel2008; Schulze2008; Arnau2011]. C_{60} dimers where formed in situ as well [Schull2009; Hauptmann2012]. All the above studies on C_{60} junctions have been done under UHV-STM conditions. We have found that it is possible by using the image capability of the STM to target individual isolated molecules and form stable single- and double-molecular junctions in ambient conditions.

5.1.1 Single-C_{60} molecular junctions

We deposit the C_{60} molecules on flamed annealed gold surfaces by drop casting using 1,2,4-trichlorobenzene (TCB) solution of concentration circa $10^{-7} - 10^{-8}$ M and then we let it dry for several hours (further information about deposition can be found in Appendix F). The STM images show small clusters and isolated molecules immobilized at monoatomic steps or sometimes on the gold terraces, as shown in Figure 5-1a. In order to focus on a particular single isolated

molecule, we first select one from a large scale image. The effect of thermal drift[2] and piezoelectric creep is counteracted by taking progressively smaller scale images and increasing the tip positioning precision as shown in Figure 5-1a-e. At the scale at which the molecule occupies the scan area (Figure 5-1e), the tip is placed directly above the molecule (Figure 5-1f) and we begin the approach from a setpoint conductance slightly above the instrument noise level (a little above $10^{-6}\ G_0$ at $0.1\ \mathrm{V}$) and gently touch the C_{60} (Figure 5-1g) while monitoring the conductance. We retract the tip before the conductance reaches $1\ G_0$ so as to avoid making a metallic contact. Finally, we rescan the area (Figure 5-1i) to see if the molecule remains on the surface.

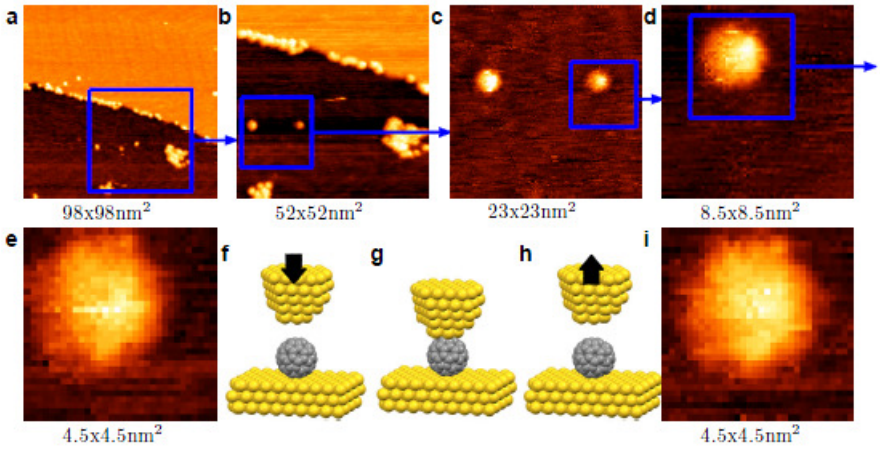

Figure 5-1: Tip positioning on C_{60} molecule. (a) Large area scan of sample of C_{60} deposited on Gold (111) from 1,2,4-trichlorobenzene (TCB) solution of concentration 10^{-7} - 10^{-8} M. (b-e) Progressively smaller images (b-d) up to the selected molecule covers the whole scan area (e). (f-h) Schematics showing: the tip positioned on top of the selected molecule (f) , contact formation after approach (g), final retraction at the initial vertical position (h). The direction of the tip movement is indicated by black arrows. During the whole cycle the current and the vertical position of the tip is recorded. (i) Image of the same area after the approach-retraction cycle, showing that the targeted molecule remained on the surface.

[2] Thermal drift for our STM is typically 0.01- $0.1\ \mathrm{nm/min}$. More details about drift determination can be found in the Appendix B.

We performed numerous approach-retraction cycles on several individual molecules and typical examples of approach (blue) - retraction (red) curves are shown in Figure 5-2 (pair of curves 1-4). Approach curves over a C_{60} before contact are linear (in semilog plot) for conductance values less that $10^{-3}\,G_0$ indicating exponential dependence of G with distance z. The apparent tunneling barrier, derived from the slope (see Equation 1-14), differs from the apparent tunneling barrier measured over C_{60} in vacuum of circa 4 eV [Schull2009]. We typically obtain an apparent tunneling barrier height close to 1.5 eV. This value is somewhat higher than the one we measure on clean gold surfaces. For comparison, an approach-retraction curve on a molecule free area of the sample is also shown in Figure 5-2(pair of curves 1-4). The decrease of the apparent tunneling barrier for an STM experiment in ambient conditions can be attributed to the existence of humidity (or contaminants) in the junction [Hahn1998].

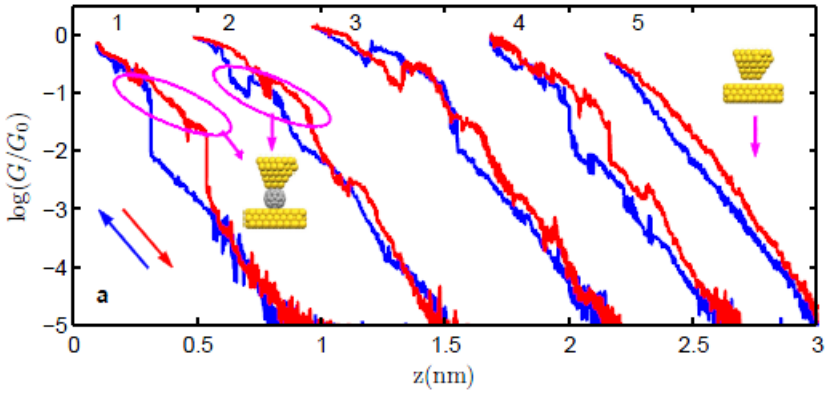

Figure 5-2: Approach-retraction conductance traces of single-C_{60} junction. Examples of approach (blue) and retraction (red) conductance curves for a bare gold tip on isolated C_{60} molecules (pairs of traces 1-4) and for a bare gold tip on bare gold (pair of traces 5). The point of contact for a single-C_{60} is shown for the first and second pair of traces.

Between approximately $10^{-3}\,G_0$ and $10^{-2}\,G_0$, the conductance traces tend to fluctuate more and the slope begins to decrease. This is again in contrast to the traces from the vacuum experiments over C_{60}, which do not show these tendencies,

and which is possibly due to adsorbates being trapped between the tip and the fullerene. As we press further we see a jump, or a sharp rise, in conductance and following this, the traces tend to rise gradually and subsequent jumps appear. The retraction curve shows similar features with a small hysteresis.

The jumps in a conductance curve over a C_{60} molecule described above, can easily understood in terms of elastic deformation stages followed by nanoscale rearrangements, as in the case of atomic sized metallic contacts which has been studied extensively in previous works [Agraït1995; Agraït1996; Rubio1996]. In the case of C_{60} at conductance values between $10^{-3}\ G_0$ and $10^{-2}\ G_0$, an adsorbate layer is trapped between the tip and the molecule and deforms elastically causing a measurable change in the slope of the conductance. Further approach of the tip will cause this layer to yield producing a jump in the conductance to $0.1\ G_0$. Above this value the traces again rise gradually due to elastic deformation.

We built the 2D-histogram by combining all the approach (see Figure 5-3a) and retraction (see Figure 5-3b) traces separately. For comparison a 2D-histogram of approach curves on gold in which the tip did not touch to the surface is plotted in Figure 5-3c. Where z is the relative movement of the STM tip. In order to plot a 2D-histogram a common reference point for measuring the z is needed for all the curves. We select a G value (G_a), for which the curves have a common feature, and we set $z = 0$. In order to avoid the creation of a discontinuity in the 2D-histogram, instead of selecting just a single point for alignment, we fit a straight line for a conductance interval around the G_a and then we shift them according to G_a of the fitted curve. The 2D-histograms of the approach and the retraction curves on C_{60} molecules has the same characteristics as the individual curves proving the reproducibility of the approach – retraction process.

We built the conductance histogram of all approach (blue), and retraction (red) curves shown in Figure 5-3e. We use a $logG$ representation [González2006], calculating the histogram out of the logarithm of conductance. The conductance histogram representing the conductance values when contact is established between a single C_{60} and the Au-tip is plotted in cyan. In this case we select points spanning $0.1\ \mathrm{nm}$ after the abrupt jump or marked change of slope in the conductance during approach for several approach curves (cyan) as shown in Figure

5-3d. This gives a histogram with mean conductance value of $0.1\ G_0$. Comparison of this contact conductance histogram (cyan) with the standard conductance histogram (blue), which takes into account the whole conductance traces, shows that they differ strongly. None of the peaks in the whole conductance histogram (blue curve) corresponds to the Au-C_{60}-Au contact formation. A comparison of the contact conductance for the approach and retraction curves (cyan and magenta curve in Figure 5-3 respectively) shows that the conductance value for the retraction curves is slightly shifted to lower values. This is due to hysteresis between the approach and retraction curve, possibly due to the elastic deformation of the gold tip.

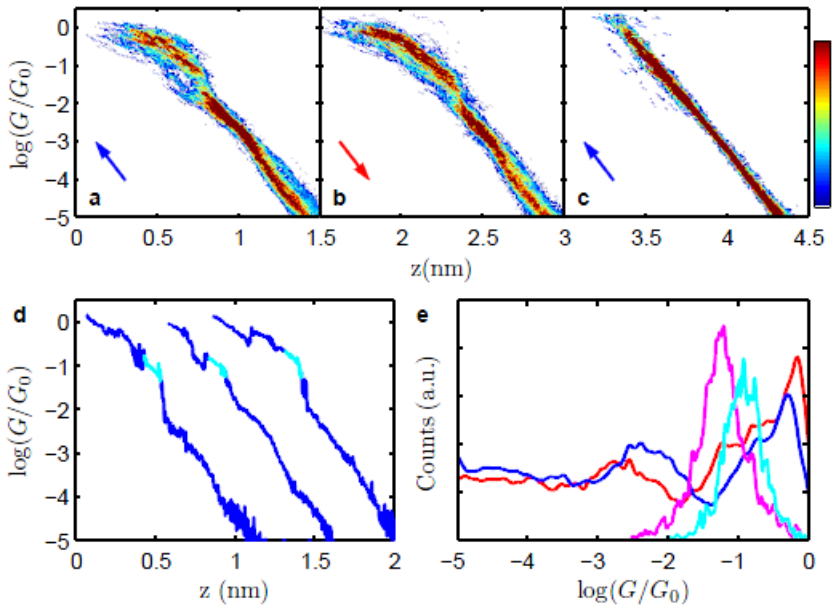

Figure 5-3: Conductance histograms of Au-C_{60}-Au junctions. (a-c) 2D-histograms of: 107 approach curves on isolated C60 (a), corresponding 107 retraction curves (b) and 52 approach curves on gold. (d) Approach curves for a bare gold tip on three different isolated C_{60} molecules (blue). Contact points are plotted in cyan. (e) Conductance histogram for the complete conductance approach (blue) retraction (red) traces and for the contact points of the approach (cyan) and retraction (magenta).

The contact conductance value for a C_{60} molecule between gold electrodes is in close agreement with observed values measured in ultrahigh vacuum (UHV) and at low temperatures with the mechanically controlled break junction technique [Böhler2007]. To the best of our knowledge there is no data for contacting a gold STM tip onto C_{60} adsorbed on a gold surface apart from that of Joachim et al [Joachim1995]. In the case of C_{60} on copper, quoted values of the contact conductance lie between 0.13 to $1.5\ G_0$ [Néel2007; Schulze2008; Arnau2011]. On a lead substrate a value of approximately $0.1\ G_0$ has been reported [Franke2009].

5.1.2 Double-C_{60} molecular Junctions

Contacting a C_{60} molecule often results in the molecule being transferred to the tip. The probability of transferring the molecule to the tip increases by stopping the tip motion at fixed intervals during the approach-retraction cycle, and ramping the bias voltage applied at the substrate. In Figure 5-4 an example of lifting a C_{60} is shown. Images a-c are progressively smaller scale images of zooming to a single molecule, before an approach-retraction cycle and images f-d the corresponding scans at the same areas after the cycle. We see that the molecule targeted is not on the surface anymore and is transferred to the tip. Once the C_{60} is transferred to the tip, we confirm that indeed the molecule is on the apex of the tip by one of three different ways which are summarized as following.

First by performing approach – retraction cycles of the C_{60} tip on the gold surface, and checking if they have the characteristic features of Au-C_{60}-Au junction (see examples in Figure 5-4g,j). We observed that there is a difference in the approach-retraction curves depending on the geometry of the gold surface. Contacting a flat gold terrace with a C_{60} tip results in conductance curves with less pronounced features than contacting o protrusion on the gold surface. This can be seen in the 2D-histograms of the approach and the retraction curves on flat surface (Figure 5-4h,l) and on protrusion (Figure 5-4k,l). This is possibly due to the adsorbate layer which trapped between the flat substrate and the C_{60}.

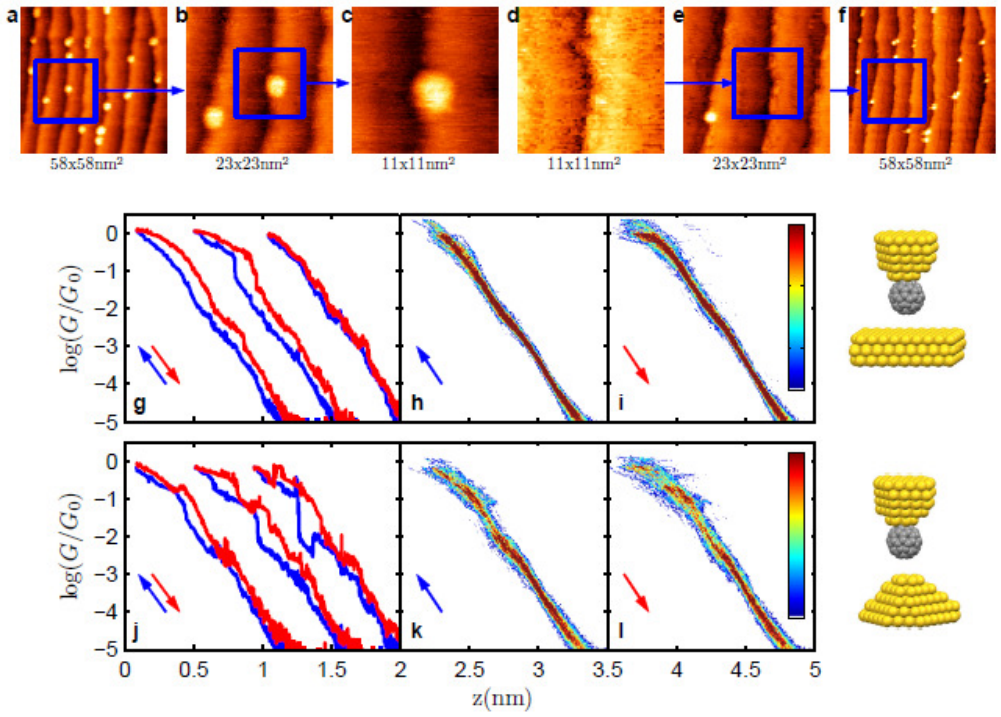

Figure 5-4: Transferring a C_{60} molecule on the tip. (a-c) Scan of a large area (a) and progressively smaller images to zoom on an individual C_{60} molecule (b,c). (d-f) Images taken after one C_{60} molecule was transferred to the tip, at the same areas as images (a-c). Note that the target molecule is missing from images (d-f). (g,j) Examples of approach (blue) and retraction (red) conductance curves for a C_{60} tip on: atomically flat gold surfaces (g) and on a gold protrusion created by crashing the bare gold tip on the gold surface (j). (h,i) 2D-histogram of: 127 approach (h) and 127 retraction (i) conductance curves for a C_{60} tip on atomically flat gold surface. (k,l) 2D-histogram of: 107 approach (k) and 107 retraction (l) conductance curves for a C_{60} tip on a protrusion of the gold surface.

A second way of checking if the C_{60} is on the apex of the tip is by imaging. It is a well-known effect that imaging with molecular tips results in increased image resolution [Nishino2005; Repp2005]. In Figure 5-5 examples of images taken by a bare gold tip a-d and C_{60} tip e-h are shown. The pairs of images b-f, c-g are scans of the same size areas and images a and b are exactly the same area. With the C_{60} tip the details of the arrangement of the molecules in the islands can be seen. The diameter values, for C_{60} molecules in images taken by C_{60} tips, have values between

1 and 1.1 nm which is the theoretical Van der Walls diameter of a C_{60} molecule [Qiao2007], while the diameter on images taken with a bare gold tip vary between $2-3$ nm. The shape of the tip for a topographic STM image with large scale structures like the C_{60}s is known to be important [Wiesendanger1994]. A gold tip has an unknown shape probably much wider than a C_{60} tip. In contrast, for atomic resolution images on flat surfaces where the tip terminates in a single atom the macroscopic shape of the tip is not important. Imaging individual C_{60}s with a C_{60}-tip, we sometimes see their structure (see Figure 5-5h). By imaging the structure of the molecules through time we see that the individual molecules immobilized at the monoatomic gold steps are stable and they do not rotate as has been reported for experiments in ultra-high vacuum [Gardener2009; Tang2011]. In contrast, the C_{60} on terraces are more mobile.

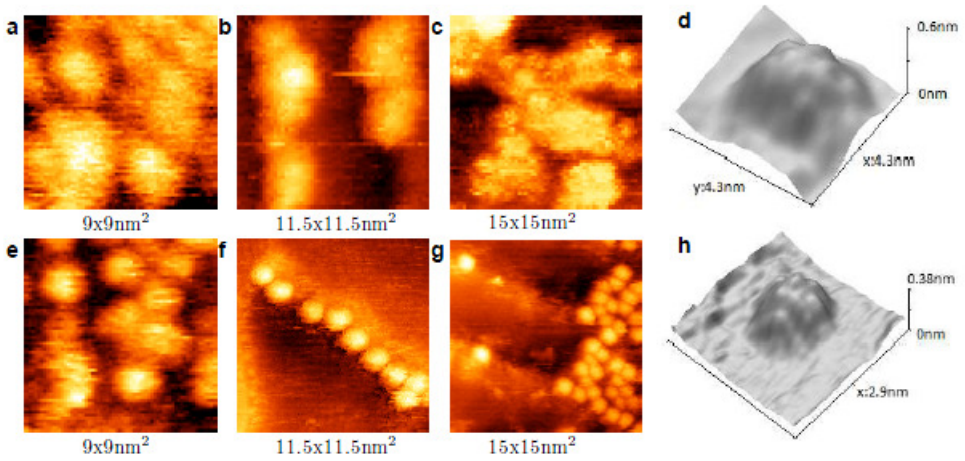

Figure 5-5: Imaging with a C_{60} and a bare Au tip. (a-c,e-g) Topographic images of small clusters of C_{60} taken by bare gold tip (a-c) and by C_{60} tip (e-h). Images a-b and e-f have the same size. Image a and e is the same area. (d,h) 3D images of individual C_{60} molecules imaged by bare-Au tip (d) and C_{60} tip (h).

The third way of checking if the C_{60} is on the apex of the tip is a current-voltage curve ($I-V$), which can unambiguously show the position of the molecule (tip or substrate). In Figure 5-4a, the approach (blue) – retraction (red) curve and the

points (circles) where each $I-V$ curve was recorded is shown. In Figure 5-4b examples of $I-V$ curves recorded before (black) and after (magenta) the C_{60} molecule was transferred to the tip are plotted.

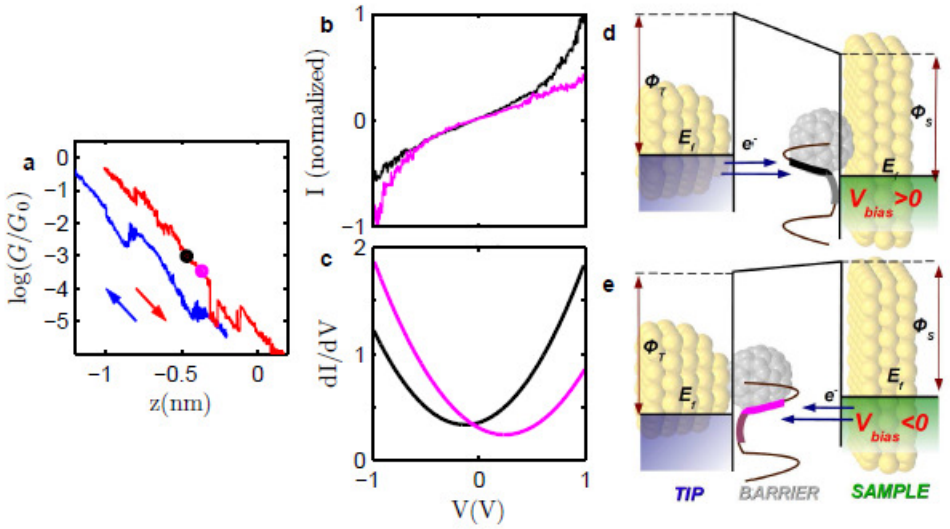

Figure 5-6: $I-V$ curves on top of a C_{60} molecule with Au tip and on top of Au with a C_{60} tip. (a,b) Approach (blue) - retraction (red) trace of Au tip on a C_{60}. During this cycle the molecule is transferred to the tip (a). Circles with different colors on the retraction curve correspond to the points where we stop and the corresponding $I-V$ curves were taken (b). The current of the $I-V$ curves is normalized to the absolute highest current value of each curve. A strong increase of the current at positive bias voltage indicates that the C_{60} is on the surface, while an increase at negative bias voltage indicates that the C_{60} is on the tip. (c) Numerical derivative of a fitted cubic polynomial curve to the $I-V$ curves which reflects the electronic density of states as drawn on (d) and (e). Black corresponds to the black and grey bold line of the molecular levels at (d) and magenta to the magenta and dark magenta bold line at (e).

With an $I-V$ curve we can determine the electronic states of the sample (occupied or unoccupied) contributing to the tunneling current [Wiesendanger1994]. The $I-V$ curves on top of a C_{60} show that the Fermi energy is closed to LUMO, because they are asymmetric with the tunneling current increasing for positive V_{bias} meaning that electrons tunnel from the occupied states of the Au-

tip to the unoccupied states of the C_{60}. If the molecule is on the tip the $I-V$ curve will be asymmetric with the tunneling current increasing for negative V_{bias} meaning that electrons tunnel from the occupied states of the substrate to the unoccupied states of the C_{60} on the tip (see Figure 5-4b). The differential conductance (see Figure 5-4c) will give us the electronic density of states [Schull2009]. The part of the density of states that is probed is drawn on the energy level diagrams of Figure 5-4d,e. The black curve of differential conductance corresponds to the black (for positive bias voltage) and the grey (for negative bias voltage) bold line on the molecular energy levels on Figure 5-4d. The magenta curve of differential conductance corresponds to the magenta (for negative bias voltage) and the dark magenta (for positive bias voltage) bold line on the molecular energy levels on Figure 5-4e.

Once we are sure that we have a C_{60} tip we performed numerous approach - retraction cycles on several individual C_{60} molecules. A typical example of approach (blue) - retraction (red) curves is shown in Figure 5-7a. A tunneling region between $10^{-5}\ G_0$ and $10^{-3}\ G_0$ is present when the C_{60} tip approaches the molecule without physical contact. The apparent tunneling barrier, derived from the slope, differs from the typical apparent tunneling barrier we measured with gold tip over C_{60} or bare gold and has values between $3-4$ eV. This increased apparent barrier height is possibly an indication for the existence of less adsorbates on the C_{60} molecules than on gold. In addition, it might also be one reason for the increased resolution of the images taken with C_{60} tips and the increased apparent height of the C_{60} molecules in the images. At conductance values around $10^{-3}\ G_0$ the approach curve has a characteristic shoulder indicating the formation of the Au-C_{60}-C_{60}-Au junction. Usually some drops of the conductance appear on the characteristic shoulder due to the sliding of the one C_{60} across the other as a consequence of the subsequent squeezing of the junction. When one of the C_{60} molecules is expelled out of the junction, there is a drop in conductance followed by a tunneling region while the C_{60} in the junction approaches the gold surface. The apparent tunneling barrier of this region is the typical one we observed for a gold tip on a C_{60}. Further pressing the junction results in an abrupt jump or change of slope in the conductance curve, signaling the formation of an Au−C_{60}−Au junction. The retraction curve is the characteristic curve we get for Au−C_{60}−Au junction.

The expulsion of the one C_{60} out of the junction can be proved as well by $I-V$ curves during junction formation. Figure 5-7b shows another example of an approach $G-z$ curve of a C_{60} tip on a single C_{60} where $I-Vs$ (see Figure 5-7c) were recorded before and after the drop in conductance. The $I-V$ curve before (black) the drop in conductance is symmetric with a strong increase of the current both at positive and negative bias voltages indicating that the junction is symmetric (Au-C_{60}-C_{60}-Au). The $I-V$ curve (magenta) recorded after the conductance drop is asymmetric with the current increasing strongly for positive bias voltage, showing that in the junction only the molecule on the tip remains.

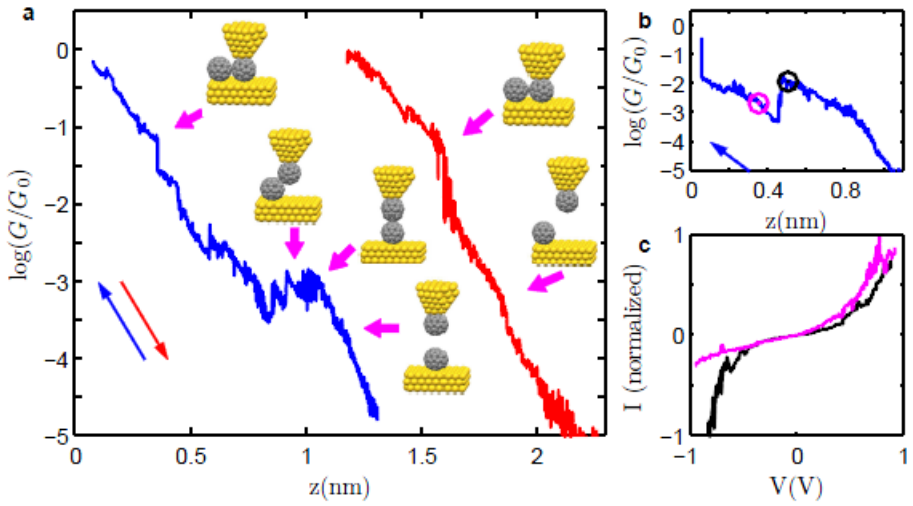

Figure 5-7: Formation of Au-C_{60}-C_{60}-Au junction. (a) Traces of approach (blue) - retraction (red) cycle of a C_{60} tip on a C_{60} molecule. The explanation of the different features of the curves are shown with the schematics. (b,c) Example of $I-V$ curves (c) recorded before (black) and after (magenta) the sharp drop of the conductance of an approach trace (b). The $I-V$ curve is symmetric before the drop in the conductance and asymmetric after, indicating that the one C_{60} is expelled from the junction.

In Figure 5-8a further examples of experimental approach (red) - retraction (red) cycles on individual C_{60} molecules with C_{60} tips are shown, as well as the 2D-histograms of 45 approach curves and the corresponding retraction curves (Figure

5-8b,c respectively). In the 2D-histograms the curves are aligned in the tunneling regime ($10^{-5} - 10^{-4}\ G_0$). The shoulder on the 2D-histogram, characteristic of the Au-C_{60}-C_{60}-Au junction formation, has a high dispersion of conductance values. The length of the shoulder varies as well, depending on when the one C_{60} is expelled from the junction (see individual curves and the 2D-histograms of approach curves). In a few cases the C_{60} that is expelled from the junction while approaching the tip reenters the junction during the retraction of the tip. In this case the retraction curve has the characteristic shoulder (see Figure 5-8a approach - retraction curve number 4).

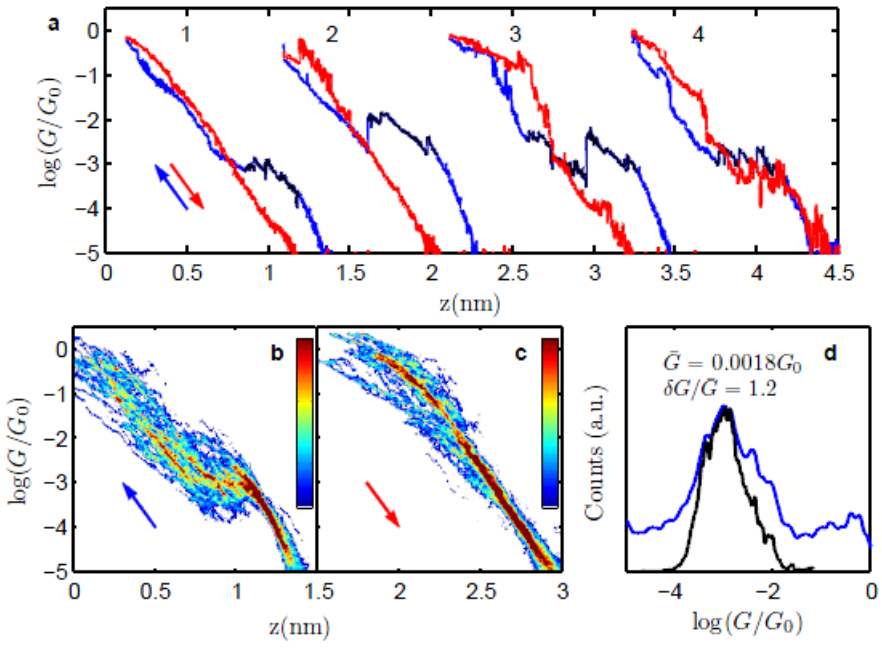

Figure 5-8: Approach-retraction conductance curves and conductance histograms of Au-C_{60}-C_{60}-Au Junction. (a) Examples of approach (blue) and retraction (red) conductance curves for a C_{60} tip on isolated C_{60} molecules (pairs of traces 1-4). Contact points for Au-C_{60}-C_{60}-Au are plotted in black. (b,c) 2D-histograms of: 45 approach curves on isolated C_{60} (b), and corresponding 45 retraction curves (c). (d) Conductance histogram for the whole approach conductance traces (blue) and for the contact points (black).

From the 2D-histogram of retraction curves we see that the appearance of the typical retraction curve of one C_{60} (see the high density red region of the histogram) is more frequent.

We selected the data points from the shoulder of the approach curves up to the point where the conductance starts increasing again as illustrated by the black part of the approach curves in Figure 5-8a and out of these values we plotted the conductance histogram in Figure 5-8d (black curve). For comparison, in the same figure we plotted the standard conductance histogram by taking in to account the whole conductance approach traces (blue curve). The peaks of both histograms coincide, while for the Au-C_{60}-Au junction, as mentioned in the previous section, the peaks differ a lot (Figure 5-3e). The average conductance of this C_{60} dimer is approximately $10^{-3}\ G_0$. The conductance of C_{60} dimers has been previously reported using Cu electrodes, and as in the case of a single C_{60} between Cu electrodes, higher values were found ($\sim 10^{-2}\ G_0$) [Schull2009].

We repeated the same approach-retraction cycles with C_{60} tips, on individual C_{60} molecules in organized and disorganized clusters. 2D-histograms of approach curves with C_{60} tips on single C_{60}s that are isolated, in clusters and in organized clusters are shown in Figure 5-9a,b,c respectively. From the 2D-histograms it can be seen that the conductance of the characteristic shoulder of the Au-C_{60}-C_{60}-Au junction increases for clusters and even more for organized clusters. Molecules in a cluster are less mobile than the isolated ones, thus the Au-C_{60}-C_{60}-Au junction formed is more stable and the coupling between the two C_{60}s is better, thus the conductance reaches higher values. Furthermore, in an organized island, molecules are very stable and a bigger force is needed to expel them from the junction. In addition, the target molecule on the surface in a cluster is attached to other C_{60}s and new paths for electronic transport through the neighbouring molecules appear. As an analogy we can think of a circuit with parallel resistors. The conductance value for a C_{60} dimer on an organized island is close to the values reported on Cu by Shull et al. [Schull2009]. Finally, it is worth mentioning here that for a single-C_{60} junction of molecules in clusters, we did not observe any difference in the conductance.

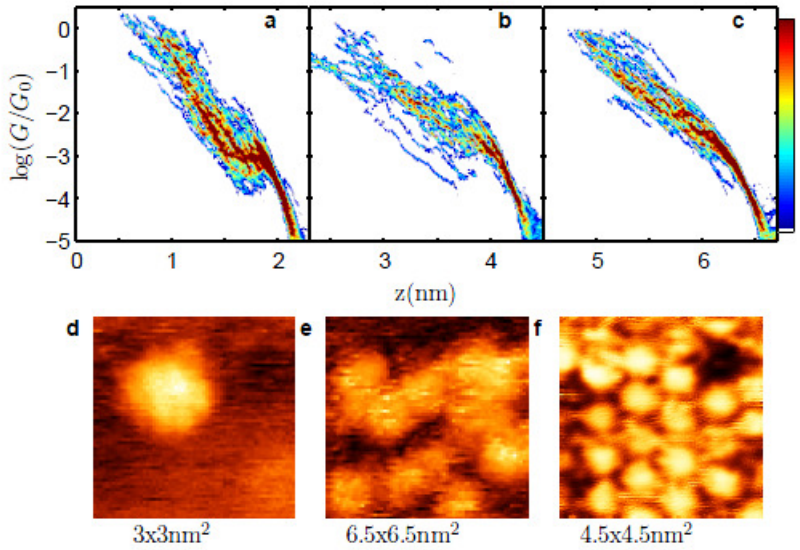

Figure 5-9: Double C_{60} junctions of isolated C_{60} and C_{60}s in clusters. (a-c) 2D-histograms of: 45 approach curves of C_{60} tips on isolated C_{60}s (a), 24 approach curves of C_{60} tips on C_{60}s in clusters (b), 28 approach curves of C_{60} tips on C_{60}s in organized clusters (c). (d-f) Characteristic images taken with C_{60} tip of: individual C_{60} (d), cluster of C_{60} (e), organized cluster of C_{60} (f).

5.2 Conductance of double-C_{60} junctions using DFT theory

To analyze the underlying transport mechanisms and to understand better the dimer junction formation and the dispersion of the conductance values, we performed large-scale quantum transport calculations on double-C_{60} junctions, based on density functional theory (DFT) [Rocha2006], using the ab-initio code SMEAGOL [Alexandre2005] which combines the Hamiltonian provided by the DFT code SIESTA [Soler2002] with the non-equilibrium Green's function formalism. Further details about the above computation methods are given in Appendix K. These calculations were performed together with K. Gillemot during my secondment at the group of Prof. C.J. Lambert at Lancaster University.

First, we examined the geometry shown in Figure 5-10a. The electrodes were assigned flat gold <111> surfaces to realistically model the large surface areas of

STM tips and the substrates. The orientation of the C_{60}s towards the Au was chosen such that a hexagon was closest to the Au surface and they were fixed at a distance of 0.22 nm. The C_{60}s were facing each other by a hexagon as well. Then we allowed vertical movement of the top complex (Upper C_{60} and Au-electrode) by systematically running the calculations over a range of different distances d (center to center distance for the two C_{60}s) between the two C_{60}s varying between 0.76 and 1.16 nm.

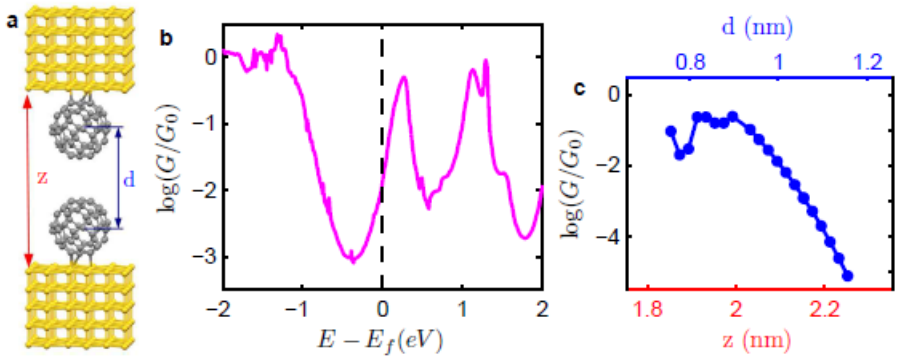

Figure 5-10: Quantum transport calculations for Au-C_{60}-C_{60}-Au junction. (a) Geometrical setup for the calculations. The arrows show the moving variables z and d. The C_{60}s were fixed to the electrodes with 0.22 nm separation. The top complex was lowered on to the bottom until the center to center distance of the two C_{60} reached 0.76 nm. (b) Example of a transmission curve of a C_{60} dimer. The black vertical dashed line indicates the position of Fermi energy obtained by DFT. (c) Theoretical calculated (from the Fermi energy obtained from DFT) approach conductance curve for a C_{60} dimer versus separation distance d of the centers of the two C_{60}s (top X axes) and the distance between the two Au electrodes z (bottom X axes).

We computed the curves of $T(E)$ (see Figure 5-10b for an example) for a range of electrode separations and evaluated the conductance for each electrode separation and for the DFT value $E_F = 0$ obtained from SIESTA. Out of these results we built the theoretical approach conductance curve shown in Figure 5-10c. The transport through the dimer is LUMO dominated. The theoretical approach conductance trace presents an increase in conductance as the two C_{60}s come closer. For conductance values close to $10^{-1}\ G_0$ with dimer center to center distance between

0.756 and 0.956 nm it forms a plateau with some drops in conductance indicating that for such separation distances the junction is compressed and deformed.

However, compressing the junction too much is not realistic. It is rather possible that by pressing the dimer junction, apart from a small deformation of the electrodes, one of the C_{60}s will be expelled from the junction. In order to model the expulsion of the one C_{60} out of the junction, we followed the model described above with the only difference that when the center to center distance of the two C_{60}s (d) reach a preset value α ($d = \alpha$), the top C_{60} moves sideways and slides across the lower C_{60}, while lowering the top electrode. This geometry is illustrated in Figure 5-11a-e. In order to estimate the probable distance that the one C_{60} starts sliding across the other we relaxed the system (minimizing the interatomic forces) of just the two C_{60}s, without the electrodes, first by local density approximation and second by taking in to account the Van der Walls (VDW) interactions between the atoms. In Figure 5-11f the final separation distances are plotted after relaxation by taking in to account the VDW interactions (red open squares) and without (blue open circles). The initial separation distance that was set for the system before relaxation is plotted with black stars. As can be seen the system has energy minima with VDW interaction for 1 nm separation and without 0.96 nm and another common minimum at 0.82 nm. The value of $d = 1$ nm is close to the center to center distance for a C_{60} lattice (1.014 nm) [Fleming1992]. Below this value the forces between the two C_{60}s are repulsive, thus further compression of the junction will cause its deformation and expulsion of the one C_{60} out of it.

We calculated the theoretical conductance approach curve with four different separation distances ($\alpha = 0.86, 0.96, 1.01, 1.06$ nm) in which the sliding of the one C_{60} starts and are shown in Figure 5-11g. The sliding of the C_{60} leads to a plateau in the conductance trace similar to the one we observed in the experiment (see examples in Figure 5-8a), with conductance that depends strongly on the separation of the two C_{60}s. While the separation of the dimer decreases, the conductance of the plateau increases.

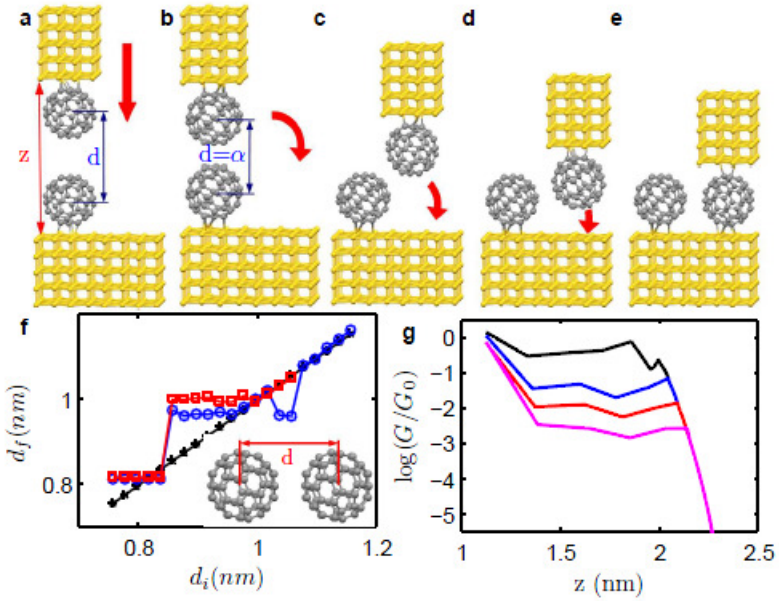

Figure 5-11: Quantum transport calculations for Au-C_{60}-C_{60}-Au junction while C_{60} sliding with respect to each other. (a-e) Geometrical setup for the calculations. The C_{60}s were fixed to the electrodes with separation of 0.22 nm. The movement of the top complex (Au-electrode and C_{60}) is shown by red arrows. The top complex was lowered on to the bottom (a) until a separation of the two C_{60} reached a preset value $d = \alpha$ (b). The top C_{60} moves sideways and slides across the lower C_{60} while lowering the top electrode (c,d), until it reaches 0.22 nm distance from the bottom electrode (e). (f) initial separation distance (d_i) of the two C_{60}s versus final (d_f), one after relaxation of the system by taking in to account the VDW interactions between the atoms (red open squares) and one without (blue open circles). For comparison, with black stars the separation distance without any relaxation. (g) Theoretical calculated approach traces. The top C_{60} with the top electrode starts sliding when distance $d = 0.86$ nm (black), $d = 0.96$ nm (blue), $d = 1.01$ nm (red), $d = 1.06$ nm (magenta).

Another factor that we expect to affect the conductance of the plateau is the variations in the orientations of the C_{60}s towards the Au surface and to each other [Néel2008]. To explore that, we computed curves of $T(E)$ for 13 different orientations with the two C_{60}s facing each other, shown in Figure 5-12a, for the geometry shown in the inset and constant separation of the two C_{60}s. Such variations cause the HOMO and LUMO peaks to be shifted relative to the E_F. The

conductance values for the E_F obtained from the DFT calculations can vary more than two orders of magnitude.

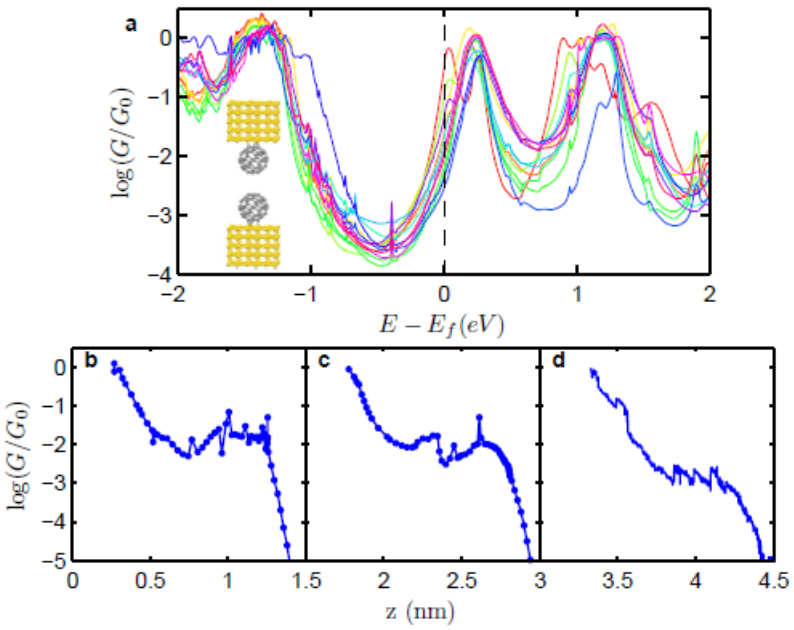

Figure 5-12: Quantum transport calculations for Au-C_{60}-C_{60}-Au junction for different orientations of the C_{60}s. (a) Transmission curves for the geometry shown in the inset for 13 different orientations of the two C_{60}s facing each other. The black vertical dashed line indicates the position of Fermi energy obtained by DFT. (b,c) Theoretical calculated approach traces for the geometry of Figure 5-11a-e for two different orientations of the two C_{60}s facing each other before starting sliding: (b) Hexagon – hexagon and (c) hexagon-atom. (d) Experimental approach trace of a C_{60} tip on an isolated individual C_{60}.

We calculated the theoretical conductance approach trace for the geometry shown in Figure 5-11a-e for two different orientations of the two C_{60}s facing each other before starting sliding at separation distance $d = 1.01$ nm. In Figure 5-12b they initially face each other with atom-hexagon and in Figure 5-12c with hexagon-hexagon. By changing the initial facing orientation, the whole facing orientation during the sliding of the two C_{60}s will change and thus the conductance plateau will

be different. Although these calculations overestimate the values for the conductance, they do reproduce the experimental trends as can be seen from the experimental approach curve shown in Figure 5-12d.

In conclusion the DFT calculations show that the conductance of a Au-C_{60}-C_{60}-Au junction can vary up to two orders of magnitude depending on the orientation of the molecules and the two C_{60}s separation distance in agreement with the high dispersion of conductance values of the shoulder on the experimental 2D-histogram.

5.3 Simultaneous *S* and *G* measurements of single- and double-C_{60} junctions

Thermopower of C_{60}s sandwiched between gold substrate and Pt, Au, and Ag tips have been reported by Yee et al [Yee2011]. Their technique is described in chapter 4. They measure the thermopower just at one specific point during the evolution of the junction and reported an average thermopower value. In contrast to these experiments, with our technique we are able to measure thermopower and conductance simultaneously during the whole evolution of the molecular junction, thereby achieving a complete characterization at the single molecule level.

Once we target an isolated individual molecule we start the approach of the tip, and the motion is stopped at fixed intervals of $20 - 30\,\mathrm{pm}$. The bias voltage is maintained at $100\,\mathrm{mV}$ during the tip motion and swept between $\pm 5\,\mathrm{mV}$ ($I-V$ curve) while the tip is stationary. In each approach – retraction cycle, $50 - 100$ $I-V$ traces are acquired. We have measured the thermopower at two temperature differences between the tip and the sample $\Delta T = 12\,\mathrm{K}$ and $25\,\mathrm{K}$ for a total of 119 single-C_{60} junctions (61 at $\Delta T = 12\,\mathrm{K}$ and 58 at $\Delta T = 25\,\mathrm{K}$) and 23 C_{60} dimers (8 at $\Delta T = 12\,\mathrm{K}$ and 15 at $\Delta T = 25\,\mathrm{K}$). Further details on the technique can be found in chapter 4

In Figure 5-13a-h, we show four examples of conductance and thermopower approach - retraction traces measured simultaneously on a single C_{60} molecule. Figure 5-13a,c,e,g shows the conductance (blue) and thermopower (green) approach traces and Figure 5-13b,d,f,h the corresponding conductance (red) and thermopower (magenta) retraction traces. Contact formation in the approach curves is clearly indicated by the abrupt jump (see Figure 5-13c,e,g) or change of slope (see Figure 5-13a) in the conductance which results in an abrupt jump in the thermopower. The subsequent jumps in the conductance observed in conductance due to the atomic rearrangements are also reflected in jumps in the thermopower, demonstrating the sensitivity of thermopower to atomic details. During retraction the curves remain almost the same indicating that the junction was unaltered.

In Figure 5-15a,b we plotted the 2D-historgram of the thermopower with conductance for temperature difference of $\Delta T = 12\,\mathrm{K}$ and $\Delta T = 25\,\mathrm{K}$ respectively, which gives information on the probability of a thermopower values to appear at certain conductance values.

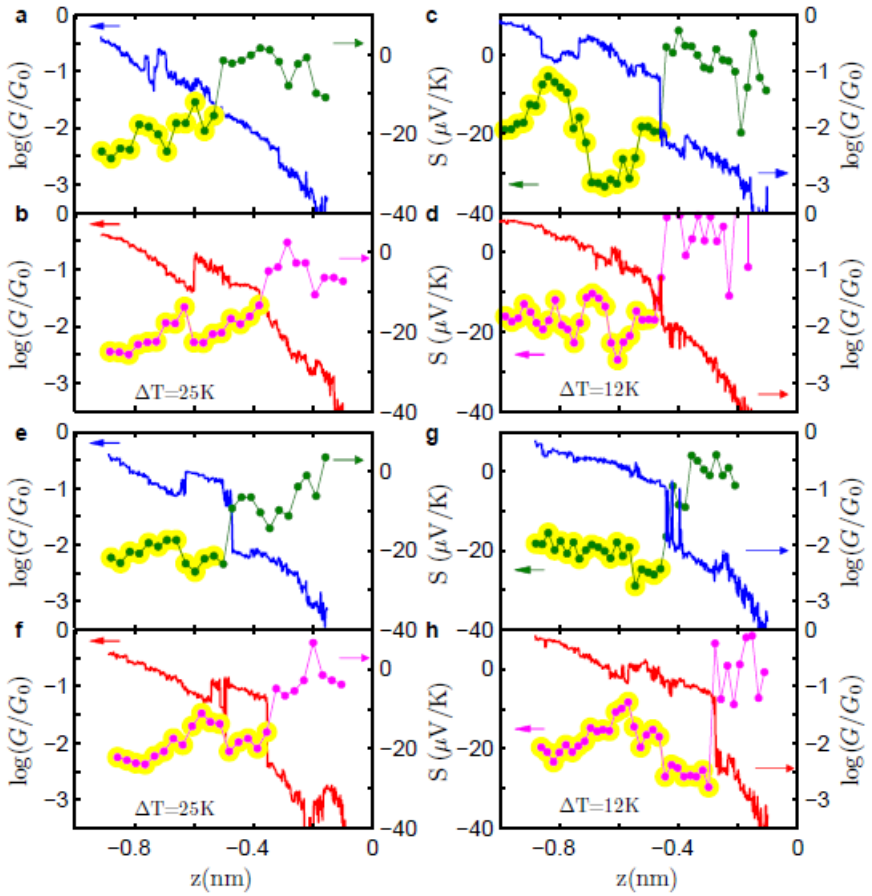

Figure 5-13: Approach and retraction traces of simultaneous conductance thermopower measurements of Au-C_{60}-Au junctions. (a,c,e,g) Conductance (blue) and thermopower (green) acquired during approach of a gold tip on individual C_{60} molecules. (b,d,f,h) Conductance (red) and thermopower (magenta) acquired during the retraction following the approach shown in a, c, e, g respectively. The temperature difference was $\Delta T = 25$ K (a-b,e-f,g-h) and $\Delta T = 12$ K for (c-d). The thermopower points corresponding to the Au-C_{60}-Au contact have been highlighted in yellow.

There are two main regions where the frequency of values is higher. The first is for conductance values between 10^{-3} and 10^{-2} G_0 where there is no physical contact between the Au tip and the C_{60} and the thermopower varies between 0 and -15 $\mu V/K$, indicating that the thermopower is sensitive in the tunneling region as well.

The second region is for conductance values higher than $10^{-1}\ G_0$ corresponding to the Au-C_{60}-Au junction and thermopower is higher, up to $-40\ \mu V/K$. Between these two regions there is a transition region for conductance between 10^{-2} and $10^{-1}\ G_0$ where the thermopower increases. This is the region where the contact of the Au tip with the C_{60} is formed.

In Figure 5-14a-h, we show three examples of conductance and thermopower approach-retraction traces measured simultaneously on a C_{60} dimer. Figure 5-14a,c,e,g shows the conductance (blue) and thermopower (green) approach traces and Figure 5-14b,d,f,h the corresponding conductance (red) and thermopower (magenta) retraction traces. The formation of the dimer is clearly identified by the already mentioned shoulder in the conductance. We can observe that a corresponding shoulder is present in the thermopower with values in the range of -25 to $-50\ \mu V/K$ for these particular dimers. On the characteristic shoulder some drops in the conductance appear while squeezing the junction and the two C_{60}s are sliding with respect to each other. These drops are also reflected in the thermopower (see Figure 5-14e) indicating the sensitivity of thermopower on the coupling of the dimer. When the one C_{60} is expelled from the junction the conductance drops with a subsequent increase up to the formation of an Au-C_{60}-Au junction indicated by the abrupt jump or change of slope while the thermopower drops to low values ($0 - 10\ \mu V/K$) and remains constant up to the formation of the Au-C_{60}-Au junction where it increases up to $-30\ \mu V/K$ for the specific examples in Figure 5-14a,e. In example Figure 5-14c,d we retract before forming the Au-C_{60}-Au junction. In most cases the retraction curves of conductance and thermopower are the typical retraction curves we observed for an Au-C_{60}-Au junction (Figure 5-14b,f). In some cases the retraction conductance curve presents the same characteristic shoulder as the approach curve indicating that the expelled C_{60} reenters the junction. Similarly the characteristic shoulder exists on the thermopower curve (Figure 5-14d,h).

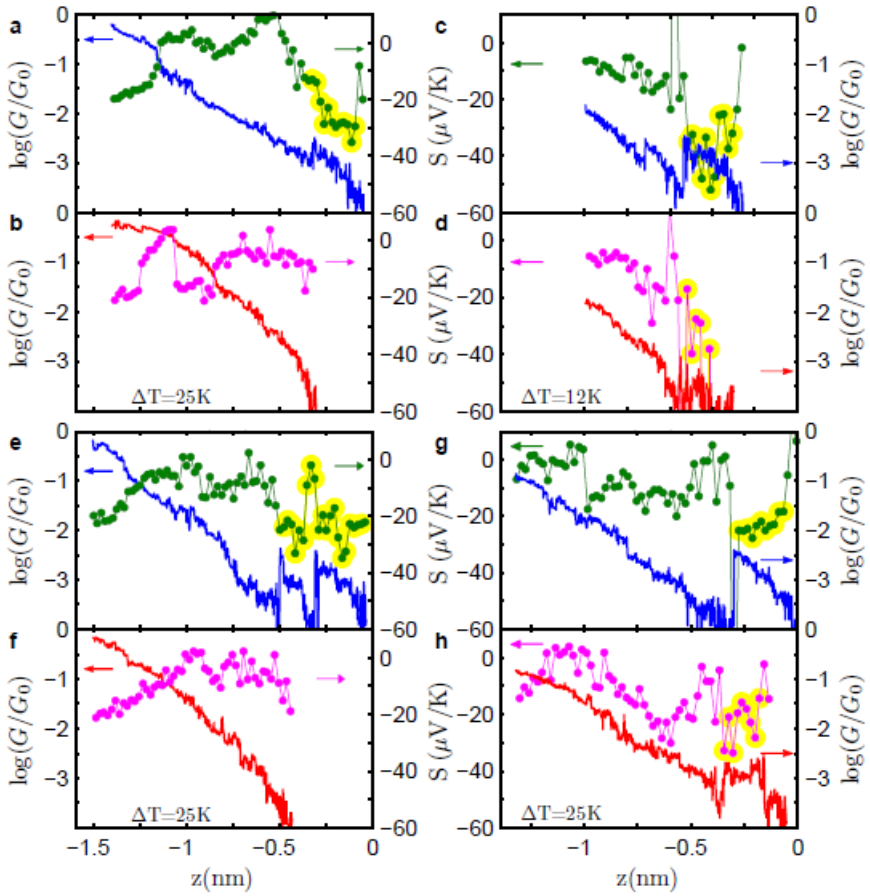

Figure 5-14: Approach and retraction traces of simultaneous conductance thermopower measurements of Au- C_{60}-C_{60}-Au junctions. (a,c,e,g) Conductance (blue) and thermopower (green) acquired during approach of a C_{60} tip on individual C_{60} molecules. (b,d,f,h) Conductance (red) and thermopower (magenta) acquired during the retraction following the approach shown in a, c, e, g respectively. The temperature difference was $\Delta T = 25$ K (a-b, e-f, g-h) and $\Delta T = 12$ K for (c-d). The thermopower points corresponding to the Au-C_{60}-C_{60}-Au contact have been highlighted in yellow. Retraction thermopower and conductance curves b,f are the typical retraction curves for Au-C_{60}-Au junction indicating that the one C_{60} was expelled from the junction, while retraction curves d,h present the characteristic shoulder of Au-C_{60}-C_{60}-Au junction indicating that C_{60} is reentering the junction.

In Figure 5-15c,d we plotted the 2D-historgram of the thermopower with conductance for temperature difference of $\Delta T = 12$ K and $\Delta T = 25$ K

respectively for Au-C_{60}-C_{60}-Au junctions. For conductance values between 5×10^{-4} and $5 \times 10^{-3}\ G_0$, which is the region of the Au-C_{60}-C_{60}-Au junction, the values of thermopower are between 0 and -70 $\mu V/K$.

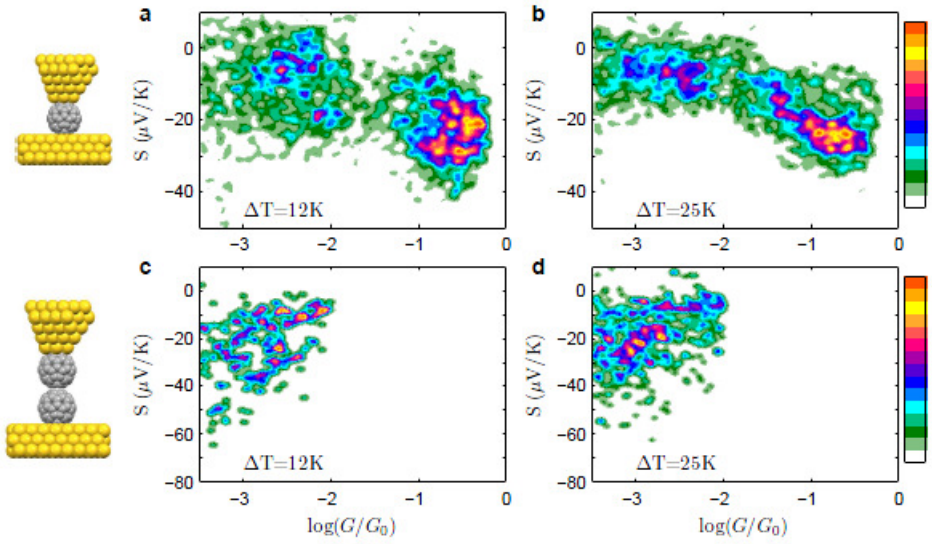

Figure 5-15: 2D-histograms of conductance with thermopower. (a) 58 approach curves of bare gold tip on C_{60} for $\Delta T = 12$ K, (b) 61 approach curves of bare gold tip on C_{60} for $\Delta T = 25$ K, (c) 8 approach curves of C_{60} tip on individual C_{60} molecules for $\Delta T = 12$ K and (d) 15 approach curves of C_{60} tip on individual C_{60} molecules for $\Delta T = 25$ K.

The thermopower for all the measured Au-C_{60}-Au junctions are in the range of -40 to $0\ \mu V/K$ with a mean value of $-18\ \mu V/K$ (see histogram of Figure 5-17a). The maximum value that we have measured for a C_{60} dimer is $-72\ \mu V/K$, and the mean value $-33\ \mu V/K$ (see histogram of Figure 5-17d). These values of S for the C_{60} dimer are almost double those for the single C_{60} and among the highest values measured to date for organic materials.

At the only measurements reported up to now [Yee2011] for the thermopower of C_{60} junction, STM-break junction technique was used for monitoring the

conductance, and the thermopower was measured at one specific point during the evolution of the junction. Due to the uncertainty in the number of molecules participating in the junction, they used statistical analysis to obtain the most probable conductance and thermopower value ($5 \times 10^{-4}\ G_0$ and $-14.5\ \mu V/K$ respectively). In contrast, we measured the conductance and thermopower of single- and double-C_{60} junctions during the whole evolution of the junction. The mean thermopower value for single-C_{60} junctions we observed is somewhat higher, while the conductance is more than two orders of magnitude higher than their value. The mean conductance and thermopower that they observed is an average for junctions with different number of C_{60}s. Formation of junctions with more than one C_{60} is possible since there is no control on the number of molecules participating in the junction in contrast to our approach, where we can distinguish the different junctions.

Further DFT calculations were performed by Prof. C.J. Lambert's group, for better understanding of the thermopower of single- and double-C_{60} junctions. An example of theoretical approach conductance and thermopower trace of single- and double-C_{60} junction is shown in Figure 5-16b,e respectively. For comparison, experimentally obtained curves are also plotted in Figure 5-16a,d. The theoretical approach curves indeed reproduce the characteristic trends of the experimentally observed ones for single- and double-C_{60} junctions. In addition Figure 5-16c,f shows curves of the figure of merit ZT, which are inaccessible in our experiments.

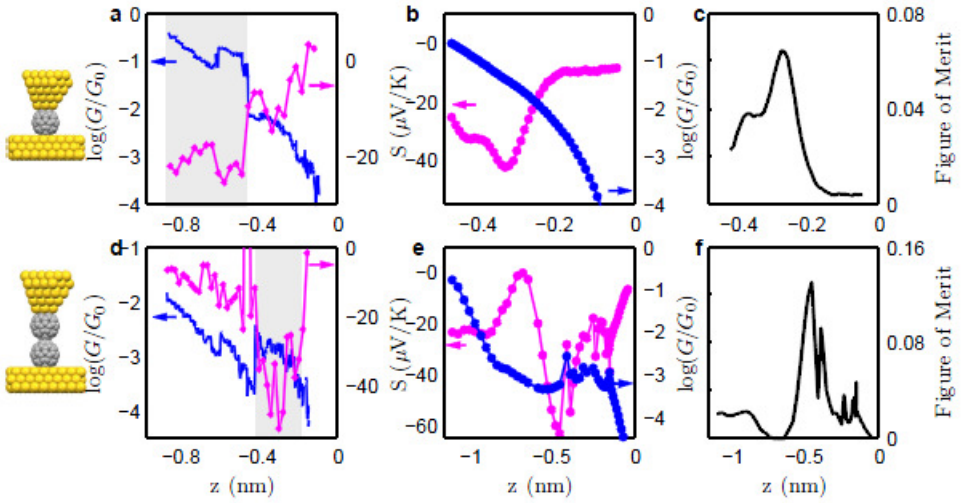

Figure 5-16: DFT calculated results of thermopower and figure of merit for single- and double-C_{60} junctions. (a) Conductance at 100 mV (blue) and thermopower (magenta), simultaneously acquired, for approach on a single C_{60} molecule. In this measurement the temperature difference was $\Delta T = 25$ K. The shaded area indicates the range of z for which the Au–C_{60}–Au junction is already formed. (b) Theoretical conductance (blue) and thermopower versus distance for a single C_{60}. (c) Calculated figure of merit ZT for a single C_{60}. (d) Conductance at 100 mV (blue) and thermopower (magenta), simultaneously acquired, during the formation of the C_{60} dimer. In this measurement, the temperature difference was $\Delta T = 12$ K. The shaded area indicates the range in which the C_{60} dimer is in the junction. (e) Theoretical conductance (blue) and thermopower versus distance for the C_{60} dimer. (f) Calculated figure of merit ZT for a C_{60} dimer.

In addition to the single- and double-C_{60} junctions, in the theoretical calculations, the thermopower values for a triple C_{60} junction were extracted. For single-, double- and triple-C_{60} junctions Figure 5-17b,e,g shows the histograms from these theoretical curves across a range of electrode separations and a range of different positions for the Fermi energy. Further information on the construction of the histograms can be found in ref. [Evangeli2013]. Although these calculations overestimate the values for the thermopower and the conductance, they do reproduce the experimental trends and support all the main conclusions from the experiments. The main discrepancy with the experiment is associated with uncertainty in the junction geometry, since the precise atomic-scale configuration

of the electrodes is not known and is likely to vary both between and along pulling curves.

The theoretical calculations also found that the average thermopower for a chain of two C_{60}s is approximately 100% higher than that of a single C_{60} with a further doubling predicted for a chain of three C_{60}s. From the theoretical histograms of Figure 5-17c,f,h, we find that the average value for ZT is also enhanced by introducing more on-the-tip C_{60}s and tuning the coupling between them. For a single C_{60}, theoretical calculations predict the average $ZT = 0.1$, for two C_{60}s $ZT = 0.4$, while for the 3 C_{60}s $ZT = 1.65$, which represents a 4-fold and a 16-fold increase, respectively. This suggests that C_{60} films with weakly coupled layers have the potential to be competitive with the best available values for inorganic materials, although it should be noted that the predictions for ZT include only the electronic contribution to the thermal conductance, which ignores parasitic contributions from phonons and therefore represents an upper bound.

In agreement with refs [Malen2010] and [Dubi2011], the relative fluctuation in the thermopower is found to be smaller than that of the conductance and, furthermore, this trend becomes more pronounced for multi-C_{60} junctions. For example for the C_{60} dimer, experimentally, we find $\delta S/\bar{S} = 0.36$, whereas $\delta G/\bar{G} = 1.2$ and theoretically for a triple-C_{60}s $\delta S/\bar{S} = 0.62$, and $\delta G/\bar{G} = 5$, where δS and δG are the standard deviations and $\bar{S}$ and $\bar{G}$ the mean values. Since the sensitivity of S to atomic-scale fluctuations is lower than that of electrical conductance, thermopower is a particularly attractive property for investigation and optimization at a molecular scale.

The increase in the thermopower observed by tuning the intermolecular coupling between identical molecules differs from various intramolecular approaches to tuning S reported up to now, including varying the chemical composition,[Baheti2008] varying the position of intramolecular energy levels relative to the work function of metallic electrodes,[Yee2010; Yee2011] systematically increasing the single molecule lengths within a family of molecules,[Malen2009] and systematically varying the conformation of molecules [Finch2009].

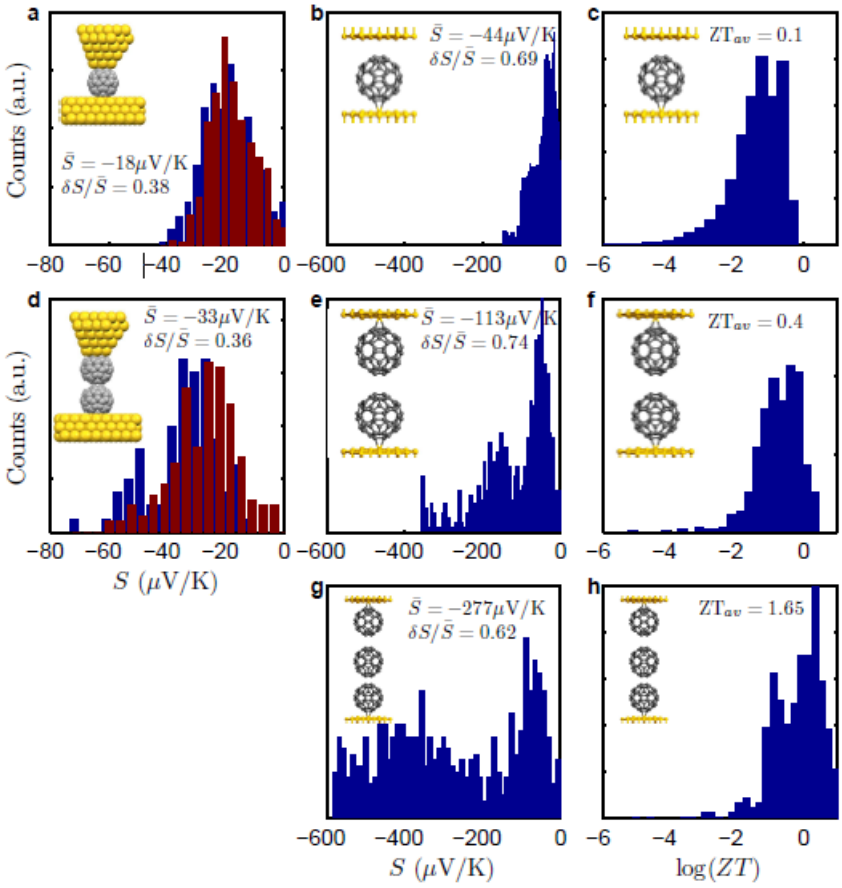

Figure 5-17: Histograms of thermopower obtained experimentally and with DFT calculations. (a) Histogram of experimental thermopower values at contact for a single C_{60} molecule, measured at $\Delta T = 12$ K (blue) and 25 K (red). (b,c) Histograms of the theoretically computed thermopower and figure of merit, respectively, for a single C_{60}. (d) Histogram of experimental thermopower values at contact for a C_{60} dimer, measured at $\Delta T = 12$ K (blue) and 25 K (red). (e,f) Histograms of the theoretically computed thermopower (e) and figure of merit (f), respectively, for a C_{60} dimer. (g,h) Histograms of the theoretically computed thermopower (g) and figure of merit (h) for a C_{60} trimer. $\bar{S}$ is the mean value of the thermopower, δS is the standard deviation.

5.4 Conclusions

In this chapter we studied the thermopower and conductance of C_{60} junctions. In contrast to previously reported experimental results, by imaging the sample prior to junction formation, the exact number of molecules in the junction is known. We formed single- and double-C_{60} junctions controllably and we measured simultaneously, the thermopower and conductance during the whole evolution of the junction. We observed that the thermopower of a C_{60} molecule can be doubled by coupling two C_{60} molecules. DFT-based calculations by Prof. C.J. Lambert's group show that the thermopower can be further doubled by coupling to a third C_{60}. The figure of merit ZT shows a 4-fold and a 16-fold increase, for two and three C_{60}s respectively with respect to one C_{60}. Our results demonstrate the possibility of engineering the thermopower of a molecular junction by mechanical manipulation.

References

[Agraït1995] Agraït, N., G. Rubio and S. Vieira (1995). "Plastic Deformation of Nanometer-Scale Gold Connective Necks." Physical Review Letters **74**(20): 3995-3998.

[Agraït1996] Agraït, N., G. Rubio and S. Vieira (1996). "Plastic Deformation in Nanometer Scale Contacts†." Langmuir **12**(19): 4505-4509.

[Alexandre2005] Alexandre, R. R., M. G.-s. Víctor, W. B. Steve, J. L. Colin, F. Jaime, et al. (2005). "Towards molecular spintronics." Nature Materials **4**(4): 335-339.

[Arnau2011] Arnau, A., R. Berndt, T. Frederiksen, G. Schull and D. Sánchez-Portal (2011). "Atomic-scale engineering of electrodes for single-molecule contacts." Nature Nanotechnology **6**: 23-27.

[Arroyo2011] Arroyo, C. R., E. Leary, A. Castellanos-Gómez, G. Rubio-Bollinger, M. T. González, et al. (2011). "Influence of Binding Groups on Molecular Junction Formation." Journal of the American Chemical Society **133**(36): 14313-14319.

[Baheti2008] Baheti, K., J. A. Malen, P. Doak, P. Reddy, S.-Y. Jang, et al. (2008). "Probing the Chemistry of Molecular Heterojunctions Using Thermoelectricity." Nano Letters **8**(2): 715-719.

[Böhler2007] Böhler, T., A. Edtbauer and E. Scheer (2007). "Conductance of individual C_{60} molecules measured with controllable gold electrodes." Physical Review B **76**(12): 125432.

[Chen2005] Chen, F., J. He, C. Nuckolls, T. Roberts, J. E. Klare, et al. (2005). "A Molecular Switch Based on Potential-Induced Changes of Oxidation State." Nano Letters **5**(3): 503-506.

[Cheng2011] Cheng, Z. L., SkoutaR, VazquezH, J. R. Widawsky, SchneebeliS, et al. (2011). "In situ formation of highly conducting covalent Au-C contacts for single-molecule junctions." Nat Nano **6**(6): 353-357.

[Dubi2011] Dubi, Y. and M. Di Ventra (2011). "Colloquium: Heat flow and thermoelectricity in atomic and molecular junctions." Reviews of Modern Physics **83**(1): 131-155.

[Evangeli2013] Evangeli, C., K. Gillemot, E. Leary, M. T. González, G. Rubio-Bollinger, et al. (2013). "Engineering the Thermopower of C60 Molecular Junctions." Nano Letters **13**(5): 2141-2145.

[Finch2009] Finch, C. M., V. M. García-Suárez and C. J. Lambert (2009). "Giant thermopower and figure of merit in single-molecule devices." Physical Review B **79**(3): 033405.

[Fleming1992] Fleming, R. M., B. Hessen, T. Siegrist, A. R. Kortan, P. Marsh, et al. (1992). Crystalline Fullerenes. Fullerenes, American Chemical Society. **481:** 25-39.

[Franke2009] Franke, K. J., G. Schulze and J. I. Pascual (2009). "Excitation of Jahn−Teller Active Modes during Electron Transport through Single C60 Molecules on Metal Surfaces." The Journal of Physical Chemistry Letters **1**(2): 500-504.

[French2012] French, W. R., C. R. Iacovella and P. T. Cummings (2012). "Large-Scale Atomistic Simulations of Environmental Effects on the Formation and Properties of Molecular Junctions." ACS Nano **6**(3): 2779-2789.

[Gardener2009] Gardener, J. A., G. A. D. Briggs and M. R. Castell (2009). "Scanning tunneling microscopy studies of C_{60} monolayers on Au(111)." Physical Review B **80**(23): 235434.

[González2006] González, M. T., S. Wu, R. Huber, S. J. van der Molen, C. Schönenberger, et al. (2006). "Electrical Conductance of Molecular Junctions by a Robust Statistical Analysis." Nano Letters **6**(10): 2238-2242.

[Guldi2000] Guldi, D. M. and M. Prato (2000). "Excited-State Properties of C60 Fullerene Derivatives." Accounts of Chemical Research **33**(10): 695-703.

[Hahn1998] Hahn, J. R., Y. A. Hong and H. Kang (1998). "Electron tunneling across an interfacial water layer inside an STM junction: tunneling distance, barrier height and water polarization effect." Applied Physics A **66**(1): S467-S472.

[Hauptmann2012] Hauptmann, N., F. Mohn, L. Gross, G. Meyer, T. Frederiksen, et al. (2012). "Force and conductance during contact formation to a C60 molecule." New J. Phys **14**.

[Huber2007] Huber, R., M. T. González, S. Wu, M. Langer, S. Grunder, et al. (2007). "Electrical Conductance of Conjugated Oligomers at the Single Molecule Level." Journal of the American Chemical Society **130**(3): 1080-1084.

[Joachim1995] Joachim, C., J. K. Gimzewski, R. R. Schlittler and C. Chavy (1995). "Electronic Transparence of a Single C_{60} Molecule." Physical Review Letters **74**(11): 2102-2105.

[Langa2007] Langa, F., J. F. Nierengarten and R. S. o. Chemistry (2007). Fullerenes: Principles and Applications, Royal Society of Chemistry.

[Malen2009] Malen, J. A., P. Doak, K. Baheti, T. D. Tilley, A. Majumdar, et al. (2009). "The Nature of Transport Variations in Molecular Heterojunction Electronics." Nano Letters **9**(10): 3406-3412.

[Malen2010] Malen, J. A., S. K. Yee, A. Majumdar and R. A. Segalman (2010). "Fundamentals of energy transport, energy conversion, and thermal

properties in organic–inorganic heterojunctions." Chemical Physics Letters **491**(4–6): 109-122.

[Moreno-García2013] Moreno-García, P., M. Gulcur, D. Z. Manrique, T. Pope, W. Hong, et al. (2013). "Single-Molecule Conductance of Functionalized Oligoynes: Length Dependence and Junction Evolution." Journal of the American Chemical Society **135**(33): 12228-12240.

[Néel2007] Néel, N., J. Kröger, L. Limot, T. Frederiksen, M. Brandbyge, et al. (2007). "Controlled Contact to a C_{60} Molecule." Physical Review Letters **98**(6): 065502.

[Néel2008] Néel, N., J. r. Kröger, L. Limot and R. Berndt (2008). "Conductance of Oriented C60 Molecules." Nano Letters **8**(5): 1291-1295.

[Nishino2005] Nishino, T., T. Ito and Y. Umezawa (2005). "A fullerene molecular tip can detect localized and rectified electron tunneling within a single fullerene–porphyrin pair." Proceedings of the National Academy of Sciences of the United States of America **102**(16): 5659-5662.

[Qiao2007] Qiao, R., A. P. Roberts, A. S. Mount, S. J. Klaine and P. C. Ke (2007). "Translocation of C60 and Its Derivatives Across a Lipid Bilayer." Nano Letters **7**(3): 614-619.

[Repp2005] Repp, J., G. Meyer, S. M. Stojković, A. Gourdon and C. Joachim (2005). "Molecules on Insulating Films: Scanning-Tunneling Microscopy Imaging of Individual Molecular Orbitals." Physical Review Letters **94**(2): 026803.

[Reuter2012] Reuter, M. G., M. C. Hersam, T. Seideman and M. A. Ratner (2012). "Signatures of Cooperative Effects and Transport Mechanisms in Conductance Histograms." Nano Letters **12**(5): 2243-2248.

[Reuter2011] Reuter, M. G., T. Seideman and M. A. Ratner (2011). "Molecular Conduction through Adlayers: Cooperative Effects Can Help or Hamper Electron Transport." Nano Letters **11**(11): 4693-4696.

[Rocha2006] Rocha, A. R., V. M. García-Suárez, S. Bailey, C. Lambert, J. Ferrer, et al. (2006). "Spin and molecular electronics in atomically generated orbital landscapes." Physical Review B **73**(8): 085414.

[Rubio1996] Rubio, G., N. Agraït and S. Vieira (1996). "Atomic-Sized Metallic Contacts: Mechanical Properties and Electronic Transport." Physical Review Letters **76**(13): 2302-2305.

[Schull2009] Schull, G., T. Frederiksen, M. Brandbyge and R. Berndt (2009). "Passing Current through Touching Molecules." Physical Review Letters **103**(20): 206803.

[Schulze2008] Schulze, G., K. J. Franke, A. Gagliardi, G. Romano, C. S. Lin, et al. (2008). "Resonant Electron Heating and Molecular Phonon Cooling in Single C_{60} Junctions." Physical Review Letters **100**(13): 136801.

[Soler2002] Soler, J. M., E. Artacho, J. D. Gale, A. García, J. Junquera, et al. (2002). "The SIESTA method for ab initio order-N materials simulation." J. Phys.: Condens. Matter **14**(2745).

[Songmei2008] Songmei, W., G. Maria Teresa, H. Roman, G. Sergio, M. Marcel, et al. (2008). "Molecular junctions based on aromatic coupling." Nature Nanotechnology **3**(9): 569-574.

[Tang2011] Tang, L., Y. Xie and Q. Guo (2011). "Complex orientational ordering of C60 molecules on Au(111)." The Journal of Chemical Physics **135**(11): -.

[van Ruitenbeek1996] van Ruitenbeek, J. M., A. Alvarez, I. Piñeyro, C. Grahmann, P. Joyez, et al. (1996). "Adjustable nanofabricated atomic size contacts." Review of Scientific Instruments **67**(1): 108-111.

[Wiesendanger1994] Wiesendanger, R. (1994). Scanning Probe Microscopy and Spectroscopy: Methods and Applications, Cambridge University Press.

[Xu2003] Xu, B. and N. J. Tao (2003). "Measurement of Single-Molecule Resistance by Repeated Formation of Molecular Junctions." Science **301**(5637): 1221-1223.

[Yee2010] Yee, S., J. Malen, P. Reddy, R. Segalman and M. A. (2010). "Thermoelectricity at the Organic-Inorganic Interface." Proceedings of the 14th International Heat Transfer Conference IHTC14, Washington, DC, August 7–13, 2010 **IHTC14-22690**: 845-855.

[Yee2011] Yee, S. K., J. A. Malen, A. Majumdar and R. A. Segalman (2011). "Thermoelectricity in Fullerene–Metal Heterojunctions." Nano Letters **11**(10): 4089-4094.

Quantum Thermopower of Metallic Nanocontacts

The advent of experimental techniques like the STM and the mechanically controlled break junctions (MCBJs) has allowed investigation of the transport properties of metallic atomic-size contacts. These atomic wires have turned out to be ideal systems where quantum theories of charge and energy transport have been thoroughly tested [Agraït2003]. However, thermoelectricity in these contacts has received little attention so far due to experimental challenges and it is still unclear what determines the thermoelectricity in a metallic atomic-size contact [Ludoph1999]. In this chapter we study the thermopower of gold and platinum atomic metallic contacts by measuring simultaneously thermopower and conductance. We show that the thermopower in the nanoscale is governed by quantum effects that are radically different from the mechanisms that govern thermoelectrics in macroscopic systems.

6.1 Introduction

As seen in chapter 2 the room temperature thermopower in bulk metals is qualitatively understood since the pioneering work of Sir N. F. Mott [Mott1936]. Its sign and magnitude ($0 - 10\ \mu\mathrm{V/K}$) depend on the energy dependence of the conductivity around the Fermi energy, which in turn depends on the inelastic relaxation time and the effective mass. Thus, for instance, the relatively large magnitude and negative sign of the thermopower of transition metals (like Ni, Pd or Pt) is attributed to the increasing relaxation time with energy due to their

characteristic density of states. This is clearly at variance with noble metals (Cu, Ag and Au), which exhibit a smaller and positive thermopower [Blatt1976]. This picture is valid only in the case of bulk metals and a different picture emerges at the nanoscale due to quantum effects.

The first measurements of the thermopower of an atomic-size contact were reported using gold MCBJs at $12\ \mathrm{K}$ [Ludoph1999]. The thermopower was found to be different in each experimental realization, and to have a very small average value, while its fluctuations were explained in terms of interference effects due to the presence of impurities near the contact region. However, in very recent experiments [Tsutsui2013] the room temperature thermopower of gold atomic-size contacts has been shown to have a non-zero average value and to exhibit oscillations as a function of the contact size that were attributed to quantum confinement. This apparent contradiction has renewed the interest in the basic question of how the thermopower of atomic-scale metallic wires depends on the material, the size of the contacts and their geometry.

6.2 Simultaneous thermopower and conductance measurements of Au and Pt contacts

To address these questions, we have studied the thermopower of Au-Au and Pt-Pt atomic-size contacts. The gold (single crystal, 99.999% purity) and platinum (99.99% purity) surfaces are flamed annealed. In addition, Pt is chemically etched with aqua regia (HNO_3:HCl 1:3). We use mechanically cut Au and Pt tips and the contacts are formed by controlled indentation of the substrate with the STM tip and subsequent separation [Agraït1995]. The STM tip is heated and the substrate is kept at room temperature and we use the technique described in chapter 4 to measure simultaneously the thermopower and the conductance of the atomic contacts. Briefly, the bias voltage V_{bias} was set to a value less than $5\ \mathrm{mV}$ and while retracting after the indentation to the substrate, the tip was stopped every $4 - 120\ \mathrm{pm}$ and the voltage is ramped between $\pm\Delta V_0 = \pm V_{bias}$. Measurements were performed with a tip-sample temperature gradient (ΔT) of $20\ \mathrm{K}$ and $40\ \mathrm{K}$.

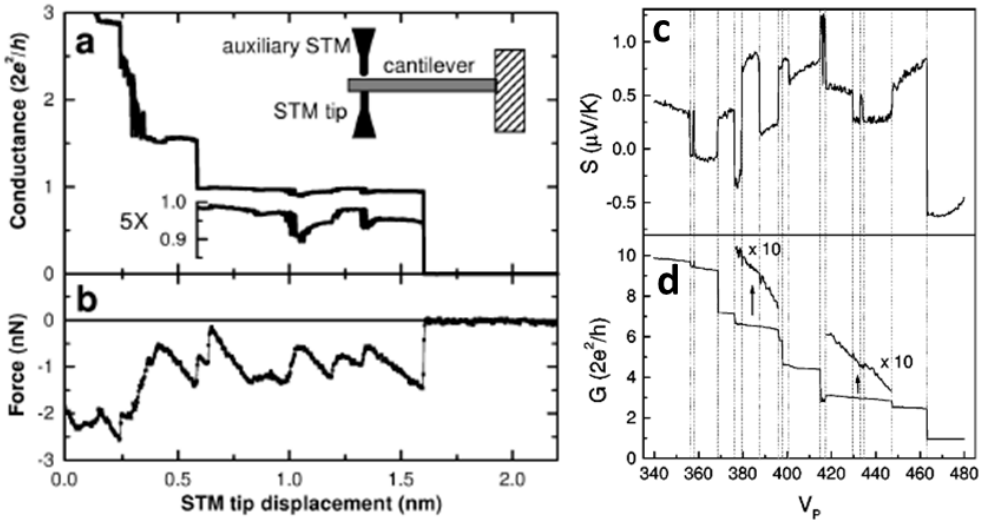

Figure 6-1: Previous measurements on conductance and thermopower of Au atomic contacts. (a,b) Simultaneous conductance (a) and force (b) measurements during chain fabrication and breaking. Inset: schematic drawing of the experimental setup. The conductance in the last plateau has been zoomed to show detailed variations [Rubio2001]. (c,d) Typical conductance G and thermopower S versus piezovoltage V_p [Ludoph1999].

As is well-known for Au contacts [Agraït1993], the conductance decreases in a step-like manner due to atomic rearrangements in the contact [Rubio1996; Rubio2001] with a tendency to exhibit plateaus close to multiples of the conductance quantum, $G_0 = 2e^2/h$, where e is the absolute value of the electron charge, and h is the Planck constant (see Figure 6-1a,b). The thermopower is also known (see Figure 6-1c,d) to present plateaus separated by abrupt variations in response to atomic rearrangements but evolves in a more complicated fashion [Untiedt1997; Ludoph1999] (see Figure 6-1c,d).

In Figure 6-2a-d we show some characteristic examples our simultaneous measurements of the conductance G and thermopower S in the last stages of the breaking of Au wires. We observed predominantly negative values, but also positive ones. In particular, we observe that in the quantized conductance plateaus, the thermopower tends to be partially suppressed. This is particularly clear for junctions

with $G \approx G_0$, which correspond to single-atom contacts or short atomic chains [Yanson1998](see Figure 6-2b).

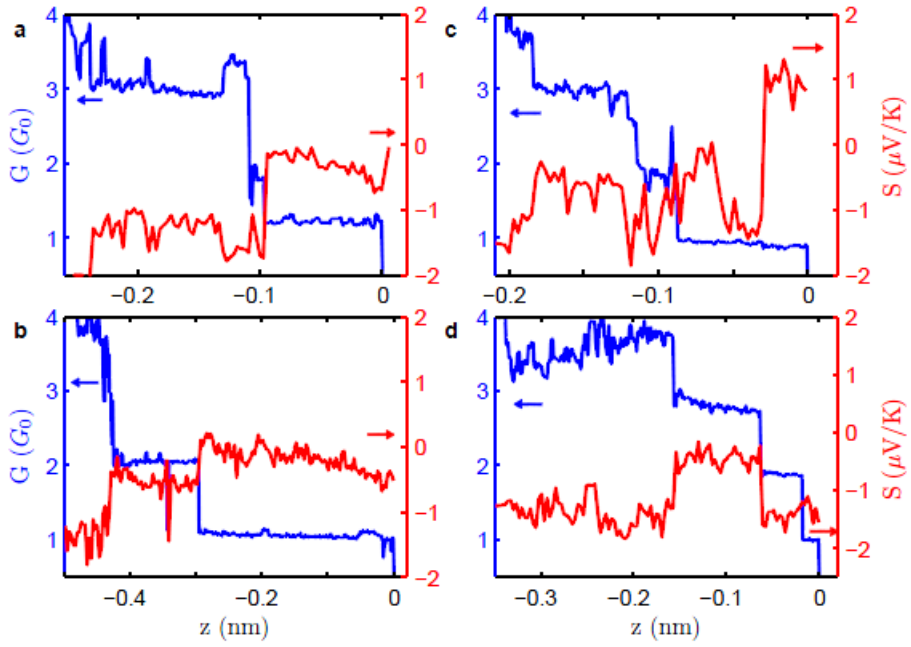

Figure 6-2: Simultaneous measurement of the conductance and thermopower of metallic atomic-size contacts. (a-d) Three characteristic examples of the conductance (blue curves) and thermopower (red curves) in the last stages of the breaking of a Au wire at room temperature. Both conductance and thermopower are very sensitive to atomic rearrangements at the junction. In some cases an atomic rearrangement that produces just a small change in the conductance results in a huge change in the thermopower, as illustrated in c.

In Figure 6-3 we show some characteristic examples of the simultaneous measurement of conductance and thermopower in the last stages of the breaking of Pt wires. As is well-known for Pt contacts [Agraït2003], the conductance tends to show a last plateau for a value around $1.5\ G_0$. For the thermopower, it evolves in a more complicated fashion, exhibiting predominantly positive values, but also

negative ones (see Figure 6-3d). In any case, both conductance and thermopower are sensitive to small changes in the junction structure.

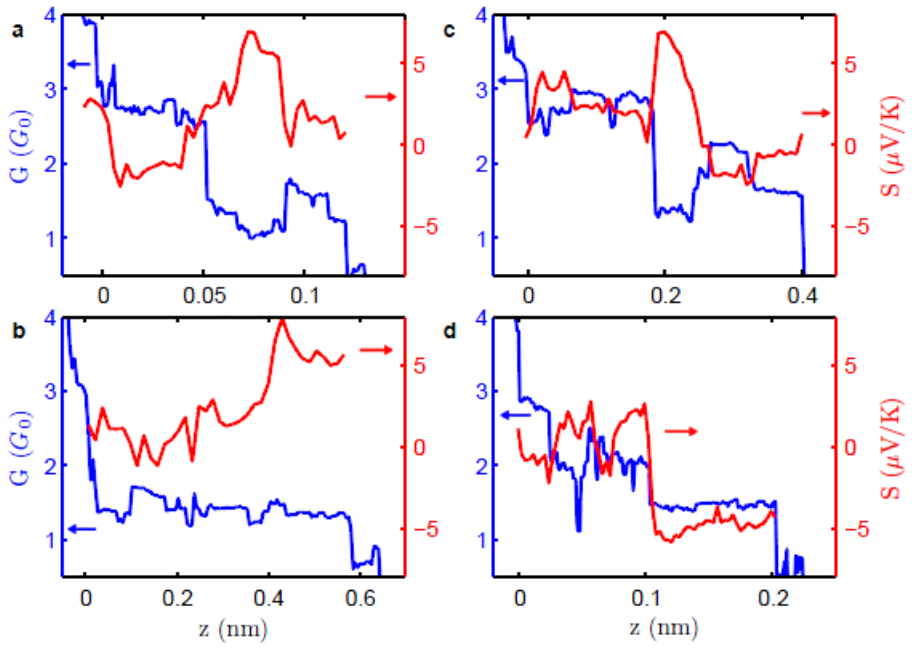

Figure 6-3: Simultaneous measurement of conductance and thermopower of Pt atomic-size contacts. (a-d) Four characteristic examples of the conductance (blue curves) and thermopower (red curves) in the last stages of the breaking of a Pt wire at room temperature.

To establish the characteristic behaviour of the thermopower we have carried out a systematic statistical analysis collecting the data of a few hundreds of contact breakings of Au and Pt. Focusing on Au and for few-atom contacts with $G < 10\ G_0$, see Figure 6-4a, we find that the thermopower fluctuates from contact to contact, but its average value is negative independently of the conductance. Moreover, for the smallest contacts ($G < 4\ G_0$), the thermopower magnitude exhibits minima coinciding with the maxima of the conductance histogram (see Figure 6-4b,c), which are close to multiples of G_0.

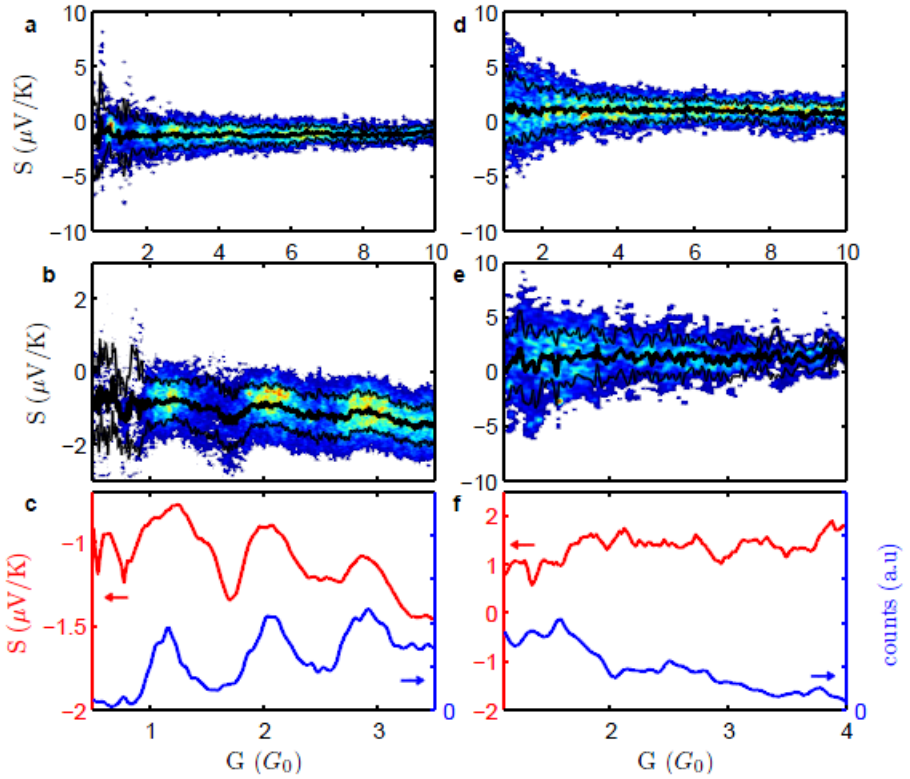

Figure 6-4: Thermopower of Au and Pt atomic-size contacts. (a,d) Thermopower density plots for small contacts up to 10 G_0 of 674 and 385 breakings of Au (a) and Pt (d) contacts respectively. Black thick lines show the average thermopower value and the black thin lines, the region around the average value within the standard deviation. The mean value of thermopower is negative for Au and positive for Pt. The sign of the mean thermopower changes from negative (positive) for small atomic contacts of Au (Pt) to positive (negative) for large contacts. (b,e) Density plots of the thermopower versus conductance for few-atom contacts ($G < 4\ G_0$) of 909 retraction curves on Au (b) and 216 retraction curves on Pt (e). Black thick lines show the average thermopower value and the black thin lines, the region around the average value within the standard deviation. (c,f) Conductance histogram (blue) and average thermopower (red) for few atom contacts of the same breaking curves as in b on Au (c) and the same retraction curves as in e on Pt (f). For (b) and (c) The thermopower of Au exhibits minima coinciding with the maxima of the conductance histogram, while for Pt there is not any pronounced feature.

These conductance maxima are shifted to slightly higher values than a typical conductance histogram [Rubio1996; Rubio2001]. This is due to the small size of the

indentations of the substrate. In that way a more stable configuration of the atoms surrounding the constriction is established, and as result they contribute to the transport by vacuum tunneling, increasing the conductance value of the contact. Further information can be found in Appendix I .

Turning now to the results for Pt contacts, we observe, as one can see in Figure 6-4d, Pt few-atom contacts exhibit an average positive thermopower with fluctuations that are around several times larger than for Au. Finally, for the smallest contacts there is not a simple correlation between the thermopower and the conductance (see Figure 6-4e,f).

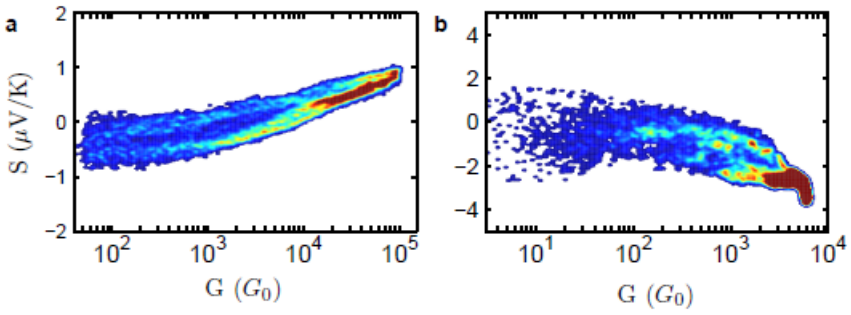

Figure 6-5: Transition of the thermopower from atomic to large Au and Pt contacts. (a,b) Density plots of the thermopower with conductance for very large contacts (up to $G > 10^4 - 10^5 G_0$) of 73 approach-retraction cycles on Au (a) and 59 on Pt (b).

Surprisingly, the sign of thermopower of atomic contacts of Au and Pt differs from that of bulk wires. In order to explore this transition we performed very large contacts ($G > 10^4\ G_0$) and then recorded the conductance and thermopower while breaking the contact. In the density plot of Figure 6-5a for Au, starting from very large contacts with $G > 10^4\ G_0$, where $S \approx +1\ \mu\mathrm{V/K}$ is in fair agreement with bulk measurements reported of $1.94\ \mu\mathrm{V/K}$ [Cusack1958], we observe a crossover to negative values as the contact size is reduced. For Pt contacts, the thermopower changes from large negative values of $S \approx -4\ \mu\mathrm{V/K}$, close to the known bulk result

of $-5.28\,\mu V/K$ [Cusack1958], to positive values as the contact size diminishes (see Figure 6-5b).

6.3 Theoretical calculations on the *S* and *G* of Au and Pt atomic contacts

To elucidate the origin of the behaviour of the thermopower of atomic-size contacts, the transport properties of these nanowires within the Landauer-Büttiker approach to coherent transport [Scheer2010] were calculated by the group of Prof. J.C. Cuevas. First classical molecular dynamics (MD) simulations were carried out to describe the formation of the atomic contacts. These simulations were performed with the code LAMMPS [Plimpton1995] within the embedded atom method [Sheng2011]. Then, once the geometries of the atomic wires were determined, the transmission coefficients were computed by combining a tight-binding model [Fong1998] for the electronic structure and Green's function techniques [Pauly2006; Pauly2011; SchirmC2013]. 100 stretching events for Au and Pt wires at 300 K in the $\langle 100 \rangle$ direction were simulated to obtain a reliable statistics. The main theoretical results for the thermopower and the conductance of Au and Pt contacts are summarized in Figure 6-6.

As one can see in Figure 6-6a,d, the thermopower changes from realization to realization with a negative average value for Au and positive for Pt, irrespective of the conductance value. Moreover, for Au contacts the magnitude of the thermopower exhibits minima correlated with the conductance maxima (Figure 6-6b) and, in particular, it is largely suppressed close to $1\,G_0$. The analysis of the transmission coefficients (Figure 6-6c) shows that this suppression is due to the fact that the transport is dominated by a single fully open conduction channel due to the Au 6*s* orbitals [Scheer1998]. Thus, the transmission reaches a maximum at the Fermi energy, which leads to a very small thermopower value at $1\,G_0$. In the case of Pt, there is no noticeable structure in the thermopower related to the main peak in the conductance histogram $\sim 1.9\,G_0$, (seeFigure 6-6e) and, in general, the fluctuations are several times larger than in Au contacts.

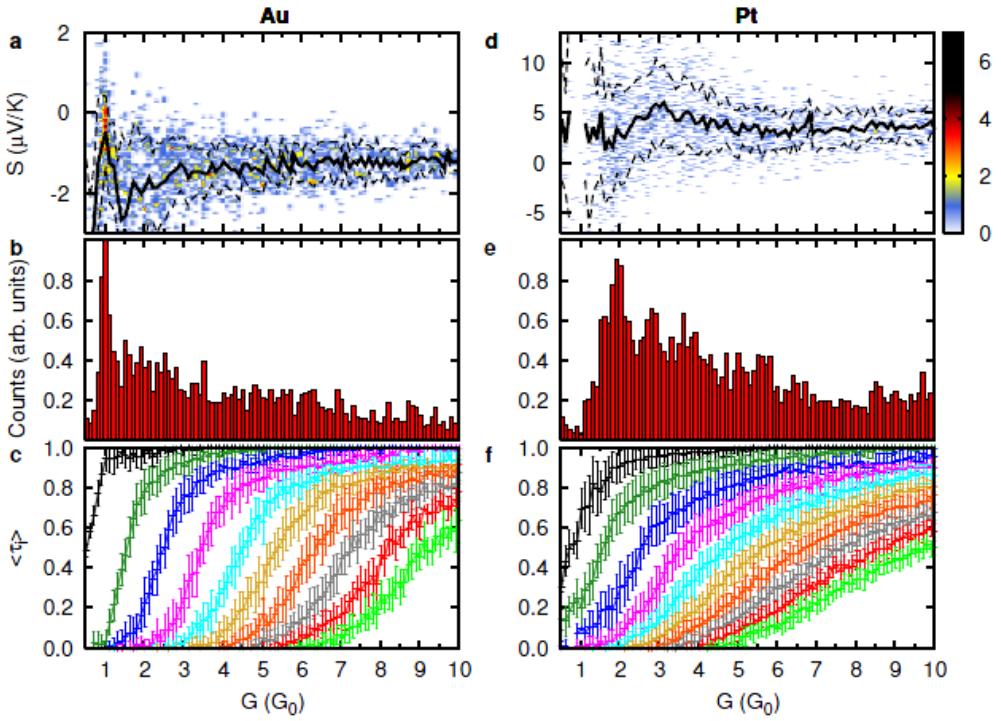

Figure 6-6: Computed thermopower and conductance of Au and Pt atomic contacts. (by Prof. J.C. Cuevas' group)**.** (a) Density plot of the thermopower as a function of the conductance computed from 100 simulations of the stretching of Au contacts at room temperature. The solid black line indicates the average value, while the dashed lines delimit the region around the average value within the standard deviation. Notice that the average value of *S* is negative. (b) The corresponding computed conductance histogram for Au contacts. The most salient feature is the appearance of a peak close to $1\ G_0$. (c) The 10 largest transmission coefficients as a function of the conductance. The lines correspond to the average values and the bars to the standard deviations. Notice that the region close to $1\ G_0$ is dominated by a single fully open channel. (d-f) The same as in panels a-c but for Pt. Notice that the average thermopower is positive. The conductance histograms exhibits a peak at around $1.9\ G_0$, which corresponds to single-atom contacts and short atomic chains. This conductance region is dominated by 4 conductions channels.

We attribute these features to the fact that the transport in Pt contacts is dominated by the 5*d* orbitals [Pauly2006]. This implies that several partially open channels contribute to the transport even in single-atom contacts, see Figure 6-6f. Thus, the transmission does not reach an extremum at the Fermi energy and the

thermopower is not suppressed. Moreover, the *d* orbitals are anisotropic and thus much more sensitive to local disorder than the s orbitals, which leads to larger fluctuations in the thermopower for Pt [Pauly2011]. Overall, these results are in very good qualitative agreement with our experimental findings.

Let us now discuss about the origin of the sign of the thermopower. In Figure 6-7a,c we show the total transmission as a function of energy for Au and Pt few-atom contacts obtained along the same stretching simulation. Notice that while the slope around the Fermi energy, E_F, is typically positive for the Au contacts, leading to a negative thermopower, it is mainly negative in the case of Pt, which results in a positive thermopower. This different behaviour can be traced back to the different electronic structures of these two metals. In the case of Au, E_F lies on a region dominated by the 6*s* orbitals with smaller contributions from the 6*p* bands. The density of states (DOS) for these orbitals, which are responsible for the transport, tends to slightly increase with energy. This is illustrated in Figure 6-7b where we show the local DOS projected onto the different orbitals of a central atom in a two-atom contact. Contrary, for Pt E_F lies close to the edge of the 5*d* bands, a region where the transmission typically diminishes with increasing energy. This reflects in turn the typical behaviour of the local DOS, as we show in Figure 6-7d for a single-atom contact.

It is worth comparing with previous results. For Au our results are in qualitative agreement with those recently reported in ref [Tsutsui2013], while the interpretation is clearly at variance. To explain their results, invoked simple free-electron models meant to describe ballistic quantum point contacts. However, these models only predict a negative sign for the thermopower and they are thus unable to explain the appearance of positive values in some Au contacts or the typical behavior of the Pt contacts. This shows that our results cannot be simply explained in terms of quantum confinement. On the other hand, the claim in ref [Ludoph1999] that the thermopower of Au contacts vanishes on average is due to the fact that those experiments were performed at a much lower temperature (12 K) and thus, the thermopower is expected to be around 30 times smaller than in our case [Pauly2011]. Moreover, the role of the impurities advocated in that work to explain the behavior of the thermopower fluctuations is certainly important, but in

addition one has the intrinsic contribution of the metal's electronic structure that dominates the average behavior and it is responsible, in particular, for the characteristic sign of the thermopower.

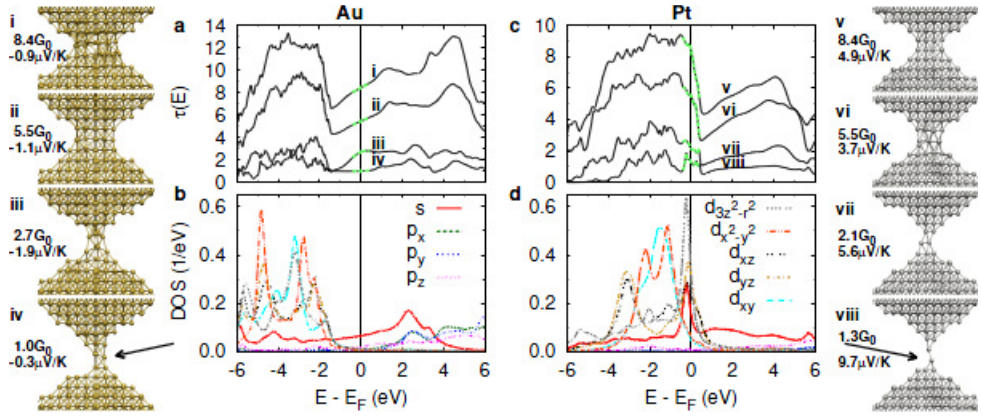

Figure 6-7: Origin of the sign of the thermopower. (by Prof. J.C. Cuevas' group). (a) Total transmission as a function of energy for the four Au contacts shown in the left column (i-iv), which correspond to different stages of the breaking of the same wire. The dashed green lines indicate the relevant energy used to compute the thermopower according to equation (2). Notice that the slope around the Fermi energy is positive, which leads to a negative thermopower. The values of the conductance and thermopower of those contacts are indicated next to the geometries. (b) Local density of states (DOS) as a function of energy projected onto the different atomic orbitals of the atom indicated with an arrow in the lower geometry. The legend is split into panels b and d. Here, *z* corresponds to the direction of the contact axis (or transport direction). Notice that the DOS is dominated by the *s* and p_z orbitals for which it exhibits a positive slope around the Fermi energy. (c-d) The same as in panels (a-b) for the Pt geometries shown in the right column (v-viii). Notice that in this case the transmission tends to exhibit a negative slope around the Fermi energy, which leads to a positive thermopower, while the local DOS is dominated by the 5*d* orbitals for which it decreases with increasing energy.

6.4 Conclusions

In this chapter, we investigated the thermopower of Au and Pt metallic contacts in the nanoscale. This system offers the unique possibility of investigating how thermoelectricity is continuously modified from bulk all the way down to the atomic scale where quantum effects dominate. We found that the thermopower, changes not only its magnitude but also its sign when the contact size dimensions are reduced to the size of a single atom. Moreover, we find that in the case of gold, the thermopower of a few-atom contact exhibits a series of minima correlated with the maxima of the conductance, in marked contrast with the platinum wires where such oscillations are absent. Coherent transport theoretical calculations by Prof. J.C. Cuevas' group, demonstrate that the different behaviour of the two metals can be explained in terms of their different electronic structure.

References

[Agraït1993] Agraït, N., J. G. Rodrigo and S. Vieira (1993). "Conductance steps and quantization in atomic-size contacts." Physical Review B **47**(18): 12345-12348.

[Agraït1995] Agraït, N., G. Rubio and S. Vieira (1995). "Plastic Deformation of Nanometer-Scale Gold Connective Necks." Physical Review Letters **74**(20): 3995-3998.

[Agraït2003] Agraït, N., A. L. Yeyati and J. M. van Ruitenbeek (2003). "Quantum properties of atomic-sized conductors." Physics Reports **377**(2–3): 81-279.

[Blatt1976] Blatt, F. J. (1976). Thermoelectric Power of Metals, Plenum Press.

[Cusack1958] Cusack, N. and P. Kendall (1958). "The Absolute Scale of Thermoelectric Power at High Temperature." Proceedings of the Physical Society (1960) **72**(5): 898-901.

[Fong1998] Fong, C. (1998). Topics in Computational Materials Science, World Scientific.

[Ludoph1999] Ludoph, B. and J. M. v. Ruitenbeek (1999). "Thermopower of atomic-size metallic contacts." Physical Review B **59**(19): 12290-12293.

[Mott1936] Mott, N. F. and H. Jones (1936). The Theory of the Properties of Metals and Alloys, Clarendon Press.

[Pauly2006] Pauly, F., M. Dreher, J. K. Viljas, M. Häfner, J. C. Cuevas, et al. (2006). "Theoretical analysis of the conductance histograms and structural properties of Ag, Pt, and Ni nanocontacts." Physical Review B **74**(23): 235106.

[Pauly2011] Pauly, F., J. K. Viljas, M. Bürkle, M. Dreher, P. Nielaba, et al. (2011). "Molecular dynamics study of the thermopower of Ag, Au, and Pt nanocontacts." Physical Review B **84**(19): 195420.

[Plimpton1995] Plimpton, S. (1995). "Fast Parallel Algorithms for Short-Range Molecular Dynamics." Journal of Computational Physics **117**(1): 1-19.

[Rubio1996] Rubio, G., N. Agraït and S. Vieira (1996). "Atomic-Sized Metallic Contacts: Mechanical Properties and Electronic Transport." Physical Review Letters **76**(13): 2302-2305.

[Rubio2001] Rubio, G., S. R. Bahn, N. Agraït, K. W. Jacobsen and S. Vieira (2001). "Mechanical Properties and Formation Mechanisms of a Wire of Single Gold Atoms." Physical Review Letters **87**(2): 026101.

[Scheer2010] Scheer, E. (2010). Molecular Electronics: An Introduction to Theory and Experiment, World Scientific Publishing Company Pte Limited.

[Scheer1998] Scheer, E., N. Agrait, J. C. Cuevas, A. L. Yeyati, B. Ludoph, et al. (1998). "The signature of chemical valence in the electrical conduction through a single-atom contact." Nature **394**(6689): 154-157.

[SchirmC2013] SchirmC, MattM, PaulyF, J. C. Cuevas, NielabaP, et al. (2013). "A current-driven single-atom memory." Nat Nano **8**(9): 645-648.

[Sheng2011] Sheng, H. W., M. J. Kramer, A. Cadien, T. Fujita and M. W. Chen (2011). "Highly optimized embedded-atom-method potentials for fourteen fcc metals." Physical Review B **83**(13): 134118.

[Tsutsui2013] Tsutsui, M., T. Morikawa, A. Arima and M. Taniguchi (2013). "Thermoelectricity in atom-sized junctions at room temperatures." Sci. Rep. **3**.

[Untiedt1997] Untiedt, C., G. Rubio, S. Vieira and N. Agraït (1997). "Fabrication and characterization of metallic nanowires." Physical Review B **56**(4): 2154-2160.

[Yanson1998] Yanson, A. I., G. R. Bollinger, H. E. van den Brom, N. Agrait and J. M. van Ruitenbeek (1998). "Formation and manipulation of a metallic wire of single gold atoms." Nature **395**(6704): 783-785.

7 Enhancing the Thermopower of OPE Molecular Junctions

In this chapter we explore how thermopower maybe enhance by structural modification of the molecular level. In particular, we investigate the addition of electron-rich groups to the Oligophenylene ethylene (OPE) molecular backbone. We also study the evolution of thermopower during stretching of the molecular junction.

7.1 Introduction

In chapter 5 we have demonstrated that the thermopower (S) of molecular junctions can be enhanced by tuning the intermolecular coupling between C_{60} molecules. Improving S in molecular junctions has been shown in several ways up to now, by varying the position of intramolecular energy levels relative to the work function of metallic electrodes [Yee2010; Yee2011], systematically increasing the single-molecule lengths within a family of molecules [Malen2009; Widawsky2013] and varying the chemical composition [Baheti2008]. For molecular junctions, it has also been predicted that extremely high figure of merit, ZT, values can be reached if the transmission spectrum contains a Fano resonance close to the Fermi level [Bergfield2009; Finch2009; Bergfield2010]. As far as we know, however, examples have not been demonstrated experimentally.

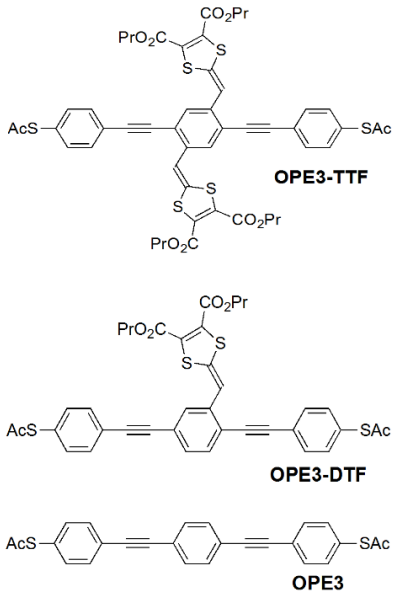

Figure 7-1: Chemical structures of the three OPE compounds. The basis for the wires is the same OPE3 backbone (3 indicating the total number of phenyl rings). The parent compound (labeled OPE3) contains no DTF units, whilst the molecules labeled OPE3-DTF and OPE3-TTF contain one and two units respectively on the central ring.

Oligo(phenylene ethylene)s (OPEs), is a family of π -conjugated molecules whose transport properties have been extensively studied in recent years [Tour2001; Huber2007]. Adding electron-rich dithiafulvalene (DTF) moieties to the robust OPE3 backbone (where '3' is the number of phenyl rings) substantially reduces the molecular oxidation potential, which should mean a significant shift of the frontier molecular orbitals towards the Fermi level. In addition, interference phenomena may appear due to the lateral groups added to the molecular backbone. We decided to examine the influence of sequentially incorporating one and two DTF units to the central ring of OPE3 backbone (OPE3-DTF and OPE3-TTF respectively) on their thermopower and conductance (G). The molecules were synthesized by the group of Prof. M. Nielsen at the University of Copenhagen and their structures are shown in Figure 7-1.

7.2 Conductance characterization of the OPE derivatives

We used commercial gold substrates on quartz, which were flame-annealed with a butane flame, and freshly cut $0.25\ \mathrm{mm}$ gold wire (99.99%) as tips. All samples were prepared by immersing the annealed gold into a $0.1\ \mathrm{mM}$ solution of the relative compound in dichloromethane (DCM) for 5 minutes, followed by a rinsing step with ethanol. Finally the sample was blown dry under nitrogen before mounting in the STM.

Conductance measurements of the OPE derivatives were performed by E. Leary using the STM Break-Junction (STM BJ) technique. During the break-junction experiment, the tip is moved vertically (z direction), in and out of contact with the substrate to form and break gold contacts, whilst the conductance $G = IV$ of the circuit was measured with a two channel current amplifier with window of $\sim 5 \times 10^{-6} - 5\ G_0$. When any of these molecules binds to both the tip and surface, a region of relatively constant conductance is produced in the $G(z)$ traces which we term the 'plateau region'. The disadvantage of this technique is the uncertainty on the number of molecules participating in the junction.

In order to analyze these events, we generate both conductance and 2D-histograms of the traces to determine both the most probable conductance values and how the conductance evolves with electrode separation. In Figure 7-2 we can see log normal conductance histograms from two different experimental runs for each compound, each run being carried out on freshly prepared gold substrates and the plateaus being selected from 10-20,000 individual traces. For all compounds, each run resulted in a peak centered slightly above $1 \times 10^{-4}\ G_0$. By fitting each histogram with a Gaussian, we found the weighted mean peak positions over both runs of $1.47 \times 10^{-4}\ G_0$, $1.46 \times 10^{-4}\ G_0$ and $1.56 \times 10^{-4}\ G_0$ for the OPE3, OPE3-DTF and OPE3-TTF respectively.

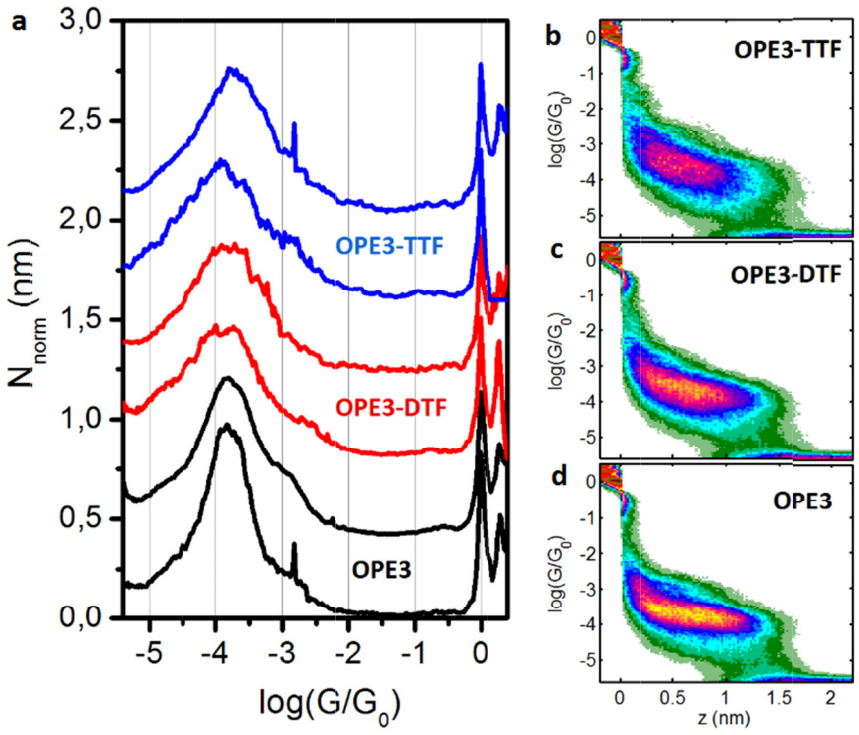

Figure 7-2: Conductance measurements on the OPEs derivatives. (a) Conductance histograms of two separate experimental runs with samples prepared from scratch for each compound. The number of plateaus in each histogram is as follows (starting from the lowest histogram); OPE3: 343 (9%), 2696 (35%), OPE3-DTF: 2179 (22%), 467 (16%), OPE3-TTF: 1603 (9%), 563 (7%). The full width at half maximum (FWHM) for each (in units of $\Delta log(G/G_0)$) is; 0.82, 1.16, 1.39, 1.5, 1.66, 1.76. (b-d) 2D-histograms for the runs with most plateaus for OPE3-TTF (b), OPE3-DTF (c) and OPE3 (d).

The conductance and 2D-histograms reveal a correlation between the degree of broadening and the number of DTF units on the backbone. From the 2D-histograms in Figure 7-2, which show the data from the runs with the highest numbers of plateaus, we see that the main protuberance is flatter for the OPE3, and becomes progressively more diffuse as the number of DTF units is increased. This behaviour can be explained if these groups interact with the electrodes during the stretching,

which would cause the molecule to fluctuate more during stretching, and may also provide additional conductance pathways through the molecule.

7.3 Simultaneous thermopower and conductance measurements of the OPE derivatives

We measured the thermopower by implementing the technique described in chapter 4 in the STM BJ technique. During retraction we stop the tip motion every $50\ \mathrm{pm}$ and we ramp the voltage between $\pm 7\ \mathrm{mV}$. The bias voltage is set at $V_{bias} = 50\ \mathrm{mV}$. The range of the conductance monitored is limited between $1 \times 10^{-5} - 2 \times 10^{-3}\ G_0$, because for the thermopower measurements we use a one channel current amplifier in order to minimize the electronical offsets. (see chapter 4). Measurements were repeated for various tip-sample temperature gradients (ΔT), all around $20\ \mathrm{K}$ and $40\ \mathrm{K}$.

In Figure 7-3 we show some characteristic examples of simultaneous G and S measurements during the stretching for OPE3, OPE3-DTF and OPE3-TTF molecular junctions. When a molecule binds to both the tip and the surface, the conductance, $G(z)$ (blue traces), and thermopower, $S(z)$ (red traces), remain relatively constant forming plateaus whose mean thermopower value varies from junction to junction. The largest values of the mean thermopower for individual plateaus can be as high as 25 $\mu\mathrm{V/K}$ (curve 2 Figure 7-3c) for OPE3-TTF, $22\ \mu\mathrm{V/K}$ for an OPE-DTF (curve 3 Figure 7-3b) and slightly less up to 18 $\mu\mathrm{V/K}$ for the OPE3 (curve 3 Figure 7-3a). We also found plateaus with very low thermopower around 2-3 $\mu\mathrm{V/K}$ (curve 1 Figure 7-3a and curve 4 Figure 7-3b).

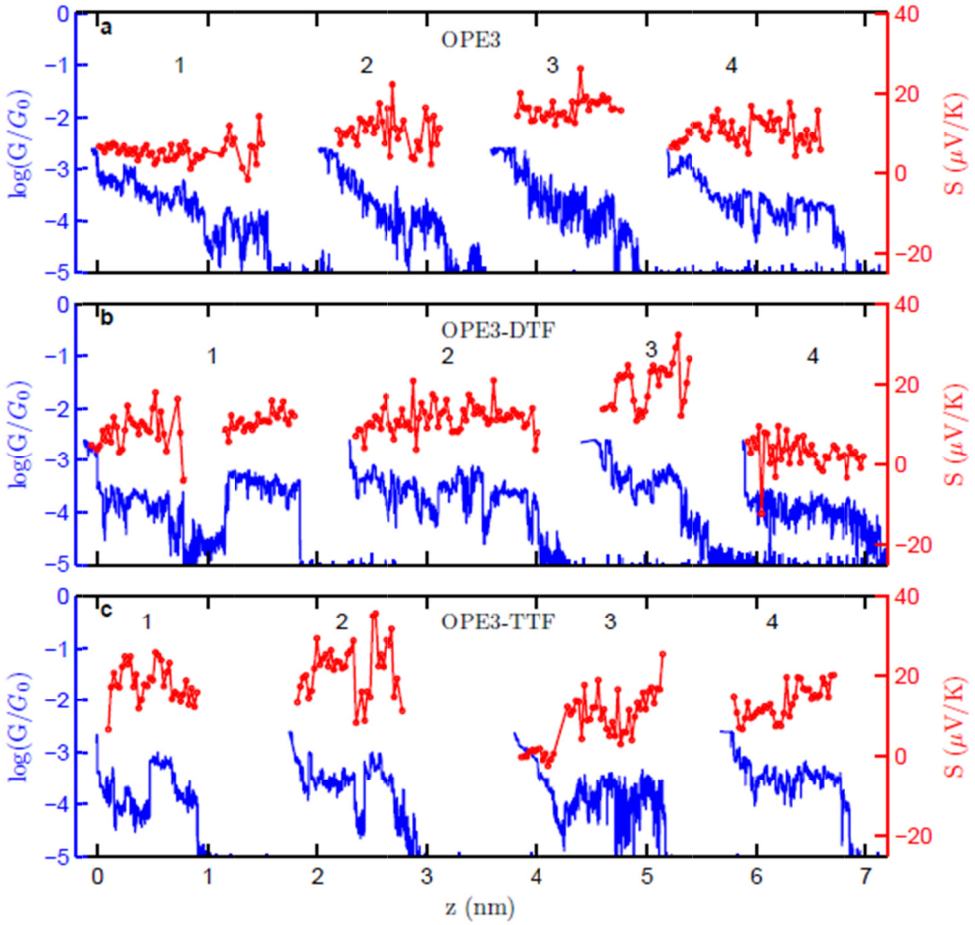

Figure 7-3: Conductance and thermopower simultaneous measurement of molecular junctions. Characteristic examples of individual retraction traces conductance (blue curves) and thermopower (red curves) acquired simultaneously for: OPE3 (a), OPE3-DTF (b) and OPE3-TTF (c). Temperature gradient across the junction was set to $\Delta T \approx 40$ K

We can observe in Figure 7-3 that some conductance plateaus appear after the conductance has dropped close to $10^{-5}\ G_0$ (see curve 3 Figure 7-3c and 1 in Figure 7-3b). These kinds of conductance jumps have been observed previously for amine terminated wires and have been ascribed to the binding and detachment of the

molecules during break-junction experiments [González2013]. This conclusion can be confirmed here by the switching of thermopower from zero to a plateau for the corresponding jump in conductance.

We generated the 2D-histograms for the $S(z)$ and $S(G)$ out of the data acquired from the $I-V$s for the three molecules in order to see how the thermopower evolves with the electrode separation and with conductance (see Figure 7-4). $G(z)$ 2D-histograms are also plotted. From the 2D-histograms for the $S(z)$ (Figure 7-4d-f) we see a high dispersion of the thermopower for all molecules. This is due to the fluctuations on individual plateaus and the variation from plateau to plateau of the average thermopower. The dispersion of thermopower increases with the number of DTF units. Conductance, on the other hand, has higher dispersion, varying more than one order of magnitude (see 2D-histograms $S(G)$ in Figure 7-4g-i) indicating the higher sensitivity of G than S to atomic-scale fluctuations.

For all the molecules we also see that thermopower generally increases (up to 25%) while stretching the molecular junction (see Figure 7-4d-f) and finally stabilizes at the end of the plateau. This sensitivity to stretching, which is more pronounced in the OPE3-TTF molecule (see Figure 7-4f), is possibly due to shifting and narrowing of the energy levels since the coupling of the molecule to the metallic electrodes is changing by stretching the junction. This effect has not been previously reported.

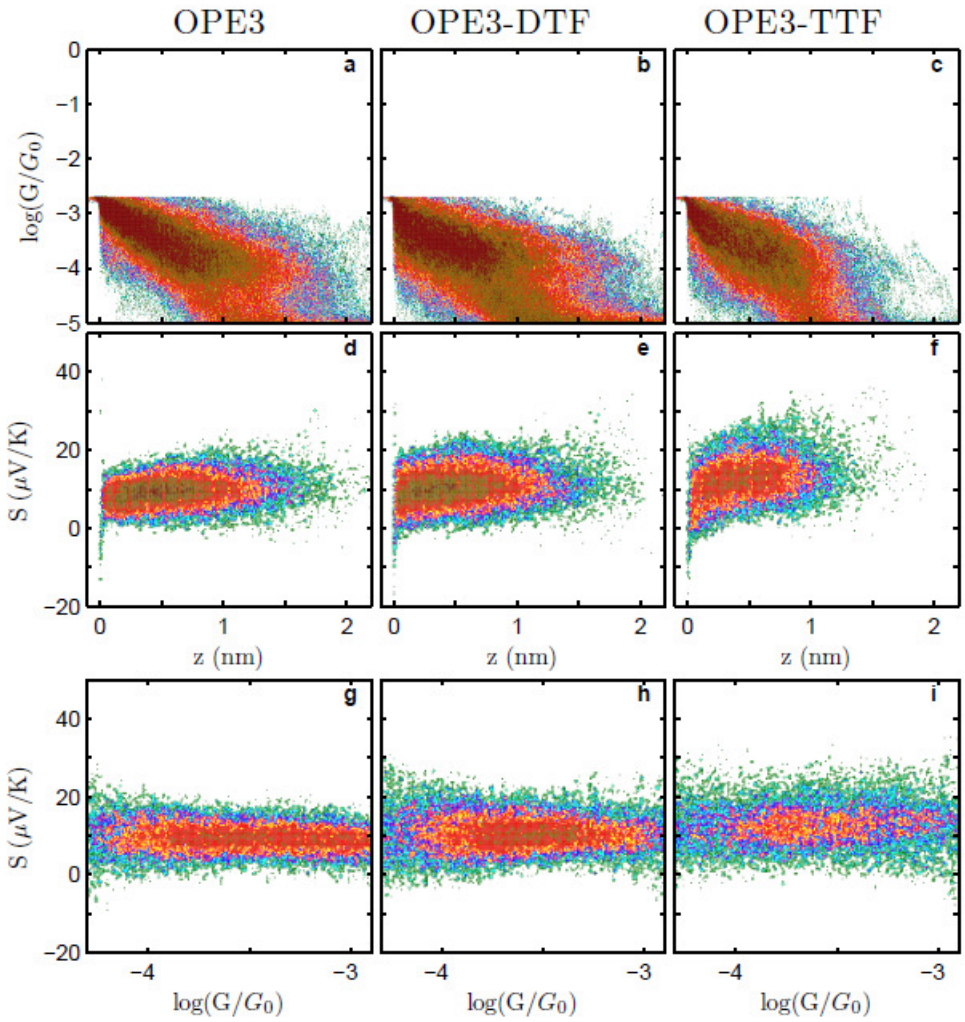

Figure 7-4: Density plots of conductance and thermopower for the OPEs derivatives. 419, 504, 367 curves for OPE3, OPE3-DTF, OPE3-TTF respectively acquired at $\Delta T = 39 - 43$ K. (a-c) Conductance with the electrode separation OPE3 (a), OPE3-DTF (b), and OPE3-TTF (c). These conductance values are obtained from the current measured at a bias voltage of 50 mV. (d-f) Thermopower with electrode separation OPE3 (d), OPE3-DTF (e), and OPE3-TTF (f). (g-I) Thermopower with Conductance OPE3 (g), OPE3-DTF (h), and OPE3-TTF (i).

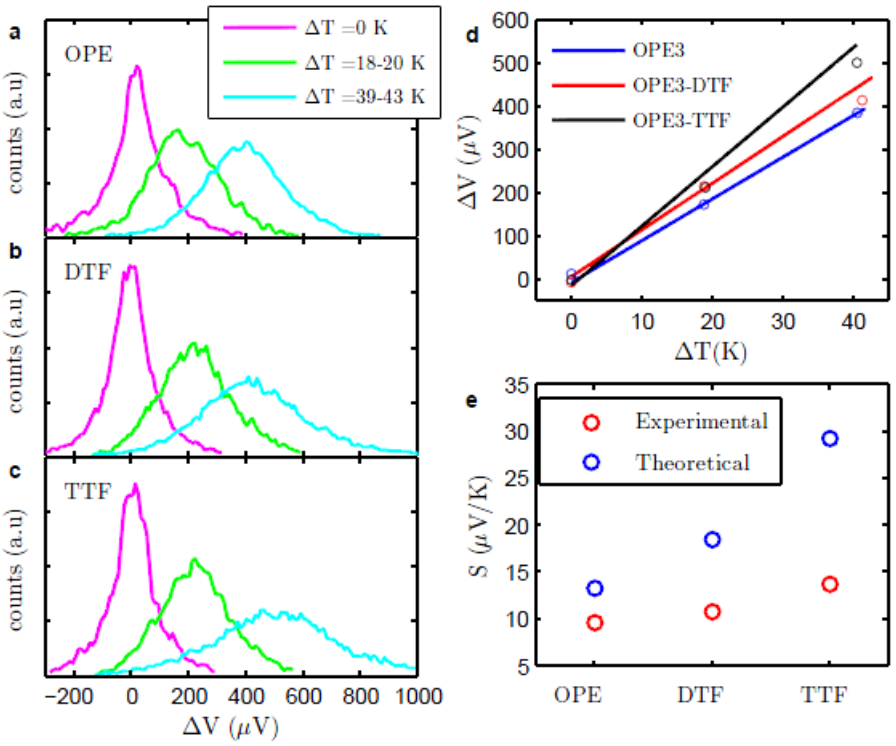

Figure 7-5: Average thermopower of the OPEs derivatives. (a-c) Histograms of the thermovoltages ΔV measured for different temperature gradients ΔT for OPE3 (a), OPE3-DTF (b) and OPE3-TTF (c). Thermovoltages are grouped for temperature gradient ranges $18-20$ K (green) and $39-43$ K (cyan) and for no temperature gradient (magenta). (d) Least squares linear fit of all ΔV vs ΔT acquired data for the three molecules, blue: OPE3, red: OPE3-DTF and black:OPE3-TTF. The slope gives the Seebeck coefficient S (experimental values at e) 9.7 ± 0.2, 10.9 ± 0.1, 13.9 ± 0.2 μV/K. (e) Experimental (red) values for thermopower extracted from the slopes of curves in panel d and the theoretical (blue) ones calculated with DFT theory.

To extract the average Seebeck coefficient of the different compounds, we measured the thermal voltage (ΔV) for hundreds of molecular junctions of each one, and for different temperature gradients (ΔT) around 20 and 40 K. The histograms of ΔV for each molecule are plotted in Figure 7-5a-c where we have grouped the data for temperature ranges of $18-20$ K and $39-43$ K. The average thermal voltage increases with the number of DTF units for the corresponding ΔT.

The least square linear fit of all the data of ΔV vs ΔT, for each molecule, is plotted in Figure 7-5d, and the slope of each curve gives the average Seebeck coefficient: 9.7 ± 0.2, 10.9 ± 0.1, 13.9 ± 0.2 $\mu V/K$ for OPE3, OPE3-DTF and OPE3-TTF respectively. While conductance of the three molecules remains unaltered, thermopower differs and shows an increase as the number of the DTF units increases. All molecules present a positive thermopower indicating that the transport is HOMO dominated (Fermi energy is close to the HOMO) in agreement with the DFT calculations by Prof. G. Solomon's group at University of Copenhagen (see Figure 7-6).

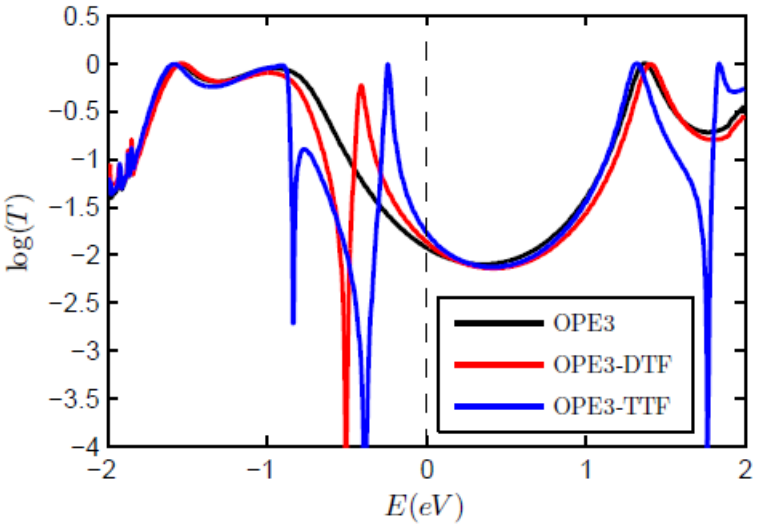

Figure 7-6: The logarithm of the transmission plotted against energy for OPE3, OPE3-DTF, and OPE3-TTF.

These DFT calculations show that adding one DTF moiety to the OPE3 (OPE3-DTF) produces a Fano resonance in the transmission spectrum ($T(E)$) which is shifted closer to the Fermi energy with the addition of a second DTF (OPE3-TTF). This shift is what is causing the increase in the observed thermopower. Despite the shifting of the resonance, it is still relatively far from the Fermi energy, thus no changes in the

conductance are observed. The thermopower, however, is related to the slope of the derivative of $lnT(E)$ at the Fermi energy and thus is more sensitive to small changes in the $T(E)$ than the conductance.

The shifting of the resonance by structural modification of molecules produces an overall 40% increase in the mean value of S with respect to the parent OPE3, whilst G remains constant. Chemical tuning of S has been demonstrated by Baheti [Baheti2008] by changing the substituents on a single benzenedithiol molecule. They found, however, only a 15% increase in S from 7.0 μ/VK for the parent molecule to 8.3 $\mu\mathrm{V/K}$ for the 2,5-dimethyl analogue.

7.4 Conclusions

In this chapter we showed that by chemically modifying an OPE molecule the Seebeck coefficient can be increased without affecting the conductance. More specifically, by incorporating a dithiafulvalene unit to the OPE backbone, we introduce a Fano resonance in the transmission spectrum close to the Fermi level. Introducing a second unit moves the Fano resonance closer to the Fermi level, enhancing the Seebeck coefficient. In contrast previous strategies suggested for improving the S were also causing modification of G. We have also observed, that the thermopower of a molecular junction is sensitive to strain, increasing as the molecule is stretched.

References

[Baheti2008] Baheti, K., J. A. Malen, P. Doak, P. Reddy, S.-Y. Jang, et al. (2008). "Probing the Chemistry of Molecular Heterojunctions Using Thermoelectricity." Nano Letters **8**(2): 715-719.

[Bergfield2010] Bergfield, J. P., M. A. Solis and C. A. Stafford (2010). "Giant Thermoelectric Effect from Transmission Supernodes." ACS Nano **4**(9): 5314-5320.

[Bergfield2009] Bergfield, J. P. and C. A. Stafford (2009). "Thermoelectric Signatures of Coherent Transport in Single-Molecule Heterojunctions." Nano Letters **9**(8): 3072-3076.

[Finch2009] Finch, C. M., V. M. García-Suárez and C. J. Lambert (2009). "Giant thermopower and figure of merit in single-molecule devices." Physical Review B **79**(3): 033405.

[González2013] González, M. T., A. Díaz, E. Leary, R. García, M. Á. Herranz, et al. (2013). "Stability of Single- and Few-Molecule Junctions of Conjugated Diamines." Journal of the American Chemical Society **135**(14): 5420-5426.

[Huber2007] Huber, R., M. T. González, S. Wu, M. Langer, S. Grunder, et al. (2007). "Electrical Conductance of Conjugated Oligomers at the Single Molecule Level." Journal of the American Chemical Society **130**(3): 1080-1084.

[Malen2009] Malen, J. A., P. Doak, K. Baheti, T. D. Tilley, A. Majumdar, et al. (2009). "The Nature of Transport Variations in Molecular Heterojunction Electronics." Nano Letters **9**(10): 3406-3412.

[Tour2001] Tour, J. M., A. M. Rawlett, M. Kozaki, Y. Yao, R. C. Jagessar, et al. (2001). "Synthesis and Preliminary Testing of Molecular Wires and Devices." Chemistry – A European Journal **7**(23): 5118-5134.

[Widawsky2013] Widawsky, J. R., W. Chen, H. Vázquez, T. Kim, R. Breslow, et al. (2013). "Length-Dependent Thermopower of Highly Conducting Au–C Bonded Single Molecule Junctions." Nano Letters **13**(6): 2889-2894.

[Yee2010] Yee, S., J. Malen, P. Reddy, R. Segalman and M. A. (2010). "Thermoelectricity at the Organic-Inorganic Interface." Proceedings of the 14th International Heat Transfer Conference IHTC14, Washington, DC, August 7−13, 2010 **IHTC14-22690**: 845-855.

[Yee2011] Yee, S. K., J. A. Malen, A. Majumdar and R. A. Segalman (2011). "Thermoelectricity in Fullerene–Metal Heterojunctions." Nano Letters **11**(10): 4089-4094.

Exploring Fullerenes as Linkers

In this chapter, we examine the wiring of single C_{60} dumbbell molecules, which consist of two terminal C_{60} groups connected through a fluorene backbone. The presence of the C_{60} groups allows us, through the formation of a highly diluted layer on Au surface, to target isolated single molecules and form single-molecule junctions.

8.1 Introduction

Molecules might be used as functional elements for future nano-scale circuits, in particular because they can be chemically modified in order to tune their properties. Of significant importance towards this goal is a fundamental understanding of the molecule-electrode contact through the chemical anchor group. The chemical anchor group binding the molecule to the electrodes can be changed systematically in order to explore factors such as binding strength, electrical coupling and conductance variability. The most commonly explored binding groups have been monodentate groups. These include thiol [Xu2003; Lörtscher2007; Leary2009; Arroyo2011; Valkenier2014], amino [Venkataraman2006; Arroyo2011; Hong2011] and pyridyl groups [Xu2003; Velizhanin2009; Wang2009; Hong2011], with nitro [Zotti2010] and cyano [Mishchenko2010] groups also scrutinized. These studies were performed using the Break-Junction technique. However, using the break-junction and related techniques [Xu2003; Nichols2010] two main problems exist. First, it remains

difficult to wire precisely one molecule. This is in part due to the lack of imaging possibilities and due to the large number of molecules close to the junction. This means that the most probable conductance value obtained statistically from such measurements may sometimes correspond to more than one wired molecule [Arroyo2011] [French2012]. Equally problematically, it remains difficult to control precisely how the anchor group binds to the electrodes and, hence, how the molecule(s) sits in the junction. These two effects lead to significant conductance variation from one junction to the next, and no obvious way exists to differentiate one-molecule from multi-molecule related effects [Songmei2008; Reuter2011; Reuter2012].

One solution may lie in the use of molecules with large area contacts such as fullerenes. In combination with a Scanning Tunneling Microscope (STM), which has the power to image single molecules before they are lifted [Kockmann2009; Lafferentz2009; Leary2011; Toher2011; Kumar2012; Matthias2012], such a strategy is highly appealing as larger molecules are easy to image and pinpoint precisely, even under ambient conditions. Our group has previously studied the 'jump into contact' of a different isolated dumbbell molecule between a gold surface and an STM tip [Leary2011]. C_{60} , though, remains relatively untested experimentally as an anchoring group, despite the theoretical effort [Wang2011; Bilan2012], with only a few examples found in the literature [Martin2008].

8.2 Formation of single-C_{60} dumbbell junctions

We examined the dumbbell molecule whose chemical structure is shown in Figure 8-1a. The molecule with only a single fluorene bridge between the fullerenes was synthesized by Prof. Nazario Martin's group at University Complutense of Madrid. Fluorene-based oligomers have been shown to possess excellent wire-like properties [Atienza-Castellanos2007]. The cyclopropane units are the connectors between the fluorene and the C_{60}s, which have been shown to improve communication between C_{60} and various addends [Eiermann1995; Kooistra2010].

We deposit the molecules on flamed annealed gold surfaces using 1,2,4-trichlorobenzene (TCB) solution of concentration circa 10^{-9} – 10^{-10} M with drop casting technique and then we let it dry for several hours (further information about deposition can be found in Appendix G). The STM images show individual molecules mainly located on the step edges (see Figure 8-1b). In order to focus on a particular single isolated molecule, we first select one from a large scale image. The effect of thermal drift[3] and piezoelectric creep is counteracted by taking progressively smaller scale images and increasing the tip positioning precision as shown in Figure 8-1b-d. At the scale at which the molecule occupies the scan area (Figure 8-1d), the tip is placed directly above the molecule (Figure 8-1e) and we start moving the tip towards the molecule to contact one of the fullerenes. Upon retraction of the tip, it is possible to determine whether the molecule has bound to the tip by searching for conductance plateaus in the retraction $G - z$ traces.

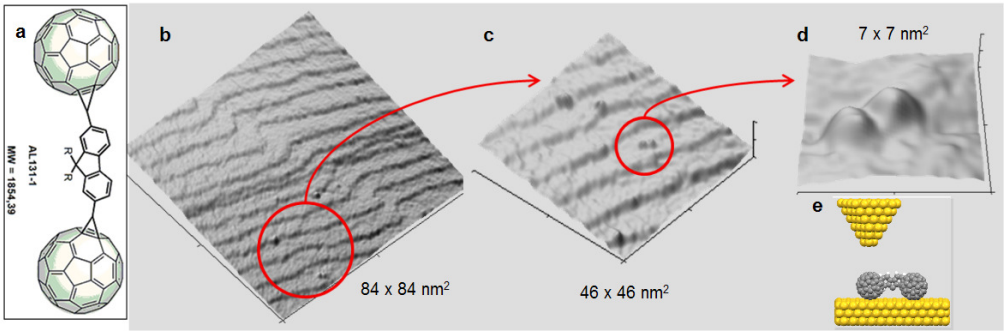

Figure 8-1: Tip positioning on an individual dumbbell molecule. (a) Chemical structure of the dumbbell molecule used. (b) Large area scan of a sample of the dumbbell molecule. (c) Further zoom in the same area. (d) Zooming on an individual molecule of the area of image (c). (e) Schematic representation of the experimental setup (to approximate scale) showing the positioning of the out-of-contact tip over the molecule.

[3] Thermal drift for our STM is typically 0.01- 0.1 nm/min. More details about drift determination can be found in the Appendix B.

A successful contact to the molecule was determined by a jump or change in the slope in the approach trace from the tunneling slope (out of contact) to a region of lesser slope (in contact), which is the typical approach curve over a C_{60} (see chapter 5). Following this, the tip was withdrawn several nanometers to an electrode separation greater than the molecular length. Re-examination of the area by imaging was always performed in order to know if the molecule remained on the surface after the first lift attempt.

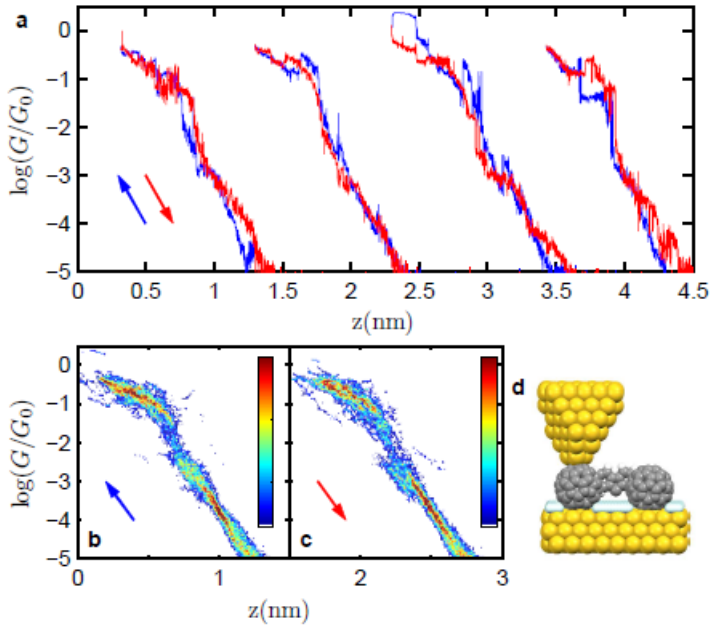

Figure 8-2 Approach-retraction conductance curves and 2D-histograms showing the tip contact to one C_{60} group. (a) Typical individual approach (blue) – retraction (red) cycle curves on the molecule on the surface. (b) 2D-histogram of successful approaches to the C_{60} group. The arrows indicate the direction of the movement of the tip. (c) 2D histogram of the retraction curves. (d) Schematic of molecule-electrode arrangement when in contact with the C_{60} linker. The adsorbates are shown in blue, and have been left off the tip, although both surfaces will be covered.

We performed numerous approach-retraction cycles on a specific molecule and typical examples of approach-retraction curves are shown in Figure 8-2a. The curves present the same characteristic features as for C_{60}s. Approach curves over a C_{60} before contact are linear (in semilog plot) and between approximately $10^{-3}\ G_0$ and $10^{-2}\ G_0$, the conductance traces tend to fluctuate more and the slope begins to decrease. As we press further we see a jump, or a sharp rise, in conductance and following this, the traces rise gradually and subsequent jumps appear (see chapter 5 for further explanation). Retraction, traces are very similar to the approach, and the conductance diminished below the noise level without an obvious plateau. The 2D-histogram of approach (Figure 8-2b) and retraction (Figure 8-2c) curves on C_{60} molecules has the same characteristics as the individual curves proving the reproducibility of the process.

Sometimes contacting the one fullerene, results in the molecule being transferred to the tip with usually, both C_{60}s attached to it. In this case is difficult to know the position of the molecule on the tip, and which part of it is on the apex. As in the case of C_{60} tip, the imaging resolution increases compare to bare gold tip. We followed the same procedure as in C_{60}, of wiring two dumbbell molecules, by moving the dumbbell tip towards the dumbbell molecule on the surface. The dumbbell as imaged with a dumbbell molecule tip before such an approach-retraction cycle and directly after is shown in Figure 8-3a,b respectively. Usually, the molecule moves from the initial position after contacting it with the dumbbell tip.

Figure 8-3c shows examples of individual approach (blue) and retraction (retraction) traces recorded above a particular molecule. The 2D-histogram of total 62 approach curves and of the corresponding retract curves (shifted along the x-axis to zero at a conductance of $0.0005\ G_0$) is plotted in Figure 8-3d,e respectively. The approach curves present a characteristic shoulder indicating the formation of an Au-dumbbell-dumbbell$_0$-Au junction. The subsequent squeezing out of the junction of one of the molecules results in a drop in conductance followed by an increase as an Au – dumbbell - Au junction forms. More often the retraction curve (center and rightmost red retraction curves) is similar to that of a single molecule (Figure 8-2a) indicating the effective expelling of one of the molecules from the junction. Less

frequently the retraction curve is similar to the approach curve with the characteristic shoulder (rightmost red curve).

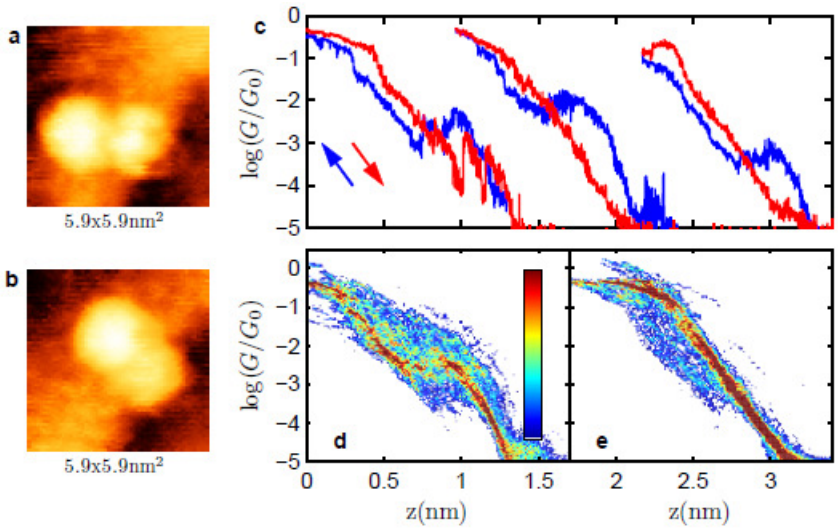

Figure 8-3: Au-dumbbell – dumbbell - Au junction. (a,b) Example of imaged of a dumbbell taken with a dumbbell tip before (a) and after (b) the approach-retraction cycle. (c) $G - z$ traces recorded over different dumbbells (blue trace = approach, red trace = separation) with dumbbell tip. The approach curve present the characteristic shoulder indicating the formation of Au-dumbbell-dumbbell-Au junction observed for C_{60}-dimer junctions. (d,e) 2D-histogram of 62 approach traces of dumbbell tip on a dumbbell (d) and of the 62 corresponding retraction curves (e).

For one specific case a dumbbell molecule was transferred to the tip at a vertically-wired configuration after approximately 40 approach and retraction cycles. Figure 8-4a-c shows successive images recorded between approach cycles to the specific individual molecule. Between Figure 8-4a,b, the entire molecule appeared to remain on the surface, despite the tip contact. Between Figure 8-4c,d the molecule was no longer visible on the surface, and the images contained streak lines due to nanometer vertical fluctuations of the tip (Figure 8-4d). From the image immediately before this dramatic change (Figure 8-4c) we can see that the tip made slight contact with the gold surface adjacent to the molecule, producing a small

protrusion, which also resulted in the molecule rotating slightly. This may have been sufficient to destabilize the molecule, allowing it to jump to the tip. We then recorded several thousand G vs z curves which are summarized in the following analysis.

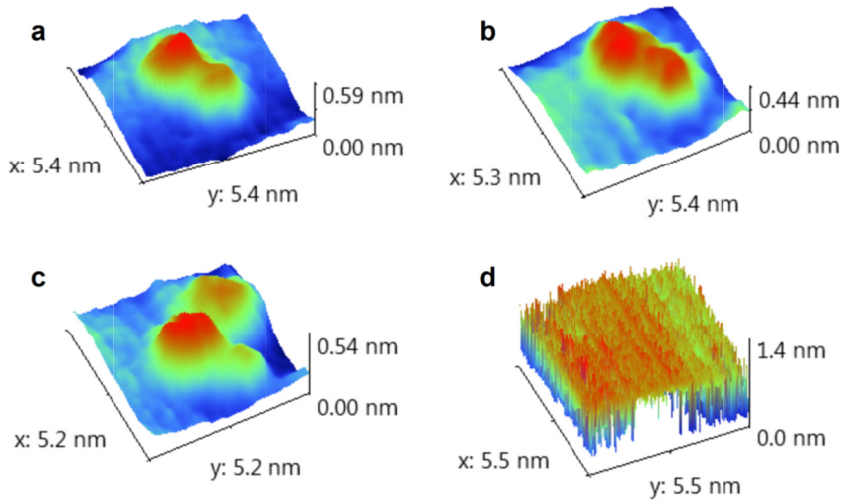

Figure 8-4: Images taken before and after the molecule transferred to the tip. (a-c) Images taken between approach-retraction cycles to contact the molecule. Between (a) and (b) the molecule maintains its position, whilst in c it has rotated slightly and a protrusion has appeared due to tip contact to the surface. (d) Image after the molecule transferred to the tip. The image is clearly much noisier, and the tip fluctuates vertically by more than $1\ \mathrm{nm}$.

From the example traces (blue) in Figure 8-5a we can see how the conductance behaves as the tip approaches the surface. We now find prominent plateaus in the region of conductance below $10^{-1}\,G_0$, which can be seen in both approach and retraction traces, which were not present before. Starting from the completely-open junction, with the current below the noise level (from $6 \times 10^{-6}\,G_0$ at $0.1\ \mathrm{V}$ bias used in this experiment), we observe a sudden jump from below the noise to a value in the vicinity of $10^{-4}\,G_0$. We interpret this as the molecule making physical contact and, hence, the beginning of the molecular junction. This is followed by a

plateau region in which the conductance rises gradually by less than one order of magnitude over a distance of 6-8 Å. This we call the low-conductance state, above which we see the conductance behaving in one of several ways. Following the plateau, mostly we observe a sharp increase in the slope, which becomes equal to that above the dumbbell-free areas of gold (blue curve 4 in Figure 8-5a). Alternatively, with less frequency we see a jump from the low-conductance region to a second, higher plateau region of conductance where the slope is also low (blue curves 1,3 in Figure 8-5a). Above this region there is also a clear tunneling region which extends, in some cases, beyond $1 \times G_0$.

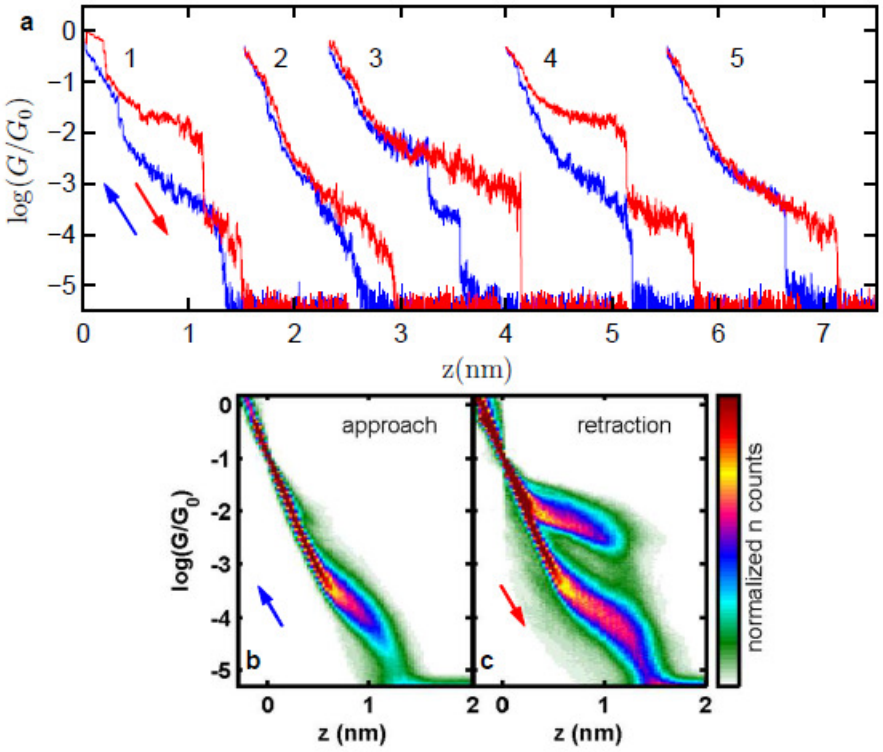

Figure 8-5 : Data showing the dumbbell, suspended from the tip, approaching and retracting from the surface. (a) Examples of typical approach traces (blue) and retraction traces (red). (b) 2D-histogram combining all 3700 approach traces. (c) 2D-histogram combining all 3700 retraction curves. Bias voltage = 0.1 V.

Upon retracting the tip, we also observe different breaking sequences (see red traces in Figure 8-5a). In those cases in which the high-conductance state was present in the approach, we always observe a plateau in the same high-conductance region in the retraction. The plateaus are, however, significantly longer than in the approach. At the end of these plateaus, the conductance drops sharply, either directly to the noise (red curve 3 Figure 8-5a), or, as in the majority of cases, to a lower region of conductance similar to that observed on initial contact in the approach (red curve 1,3 Figure 8-5a). Upon further retraction, these traces extend several more Angstroms in the low-conductance state before, finally, the molecular junction breaks and the conductance drops sharply below the noise. When there was no jump to the high-conductance state in the approach trace, the subsequent retraction traces either appear identical to the approach (curve 2 in Figure 8-5a), containing only the low-conductance plateaus, or they also contain a plateau in the high-conductance state (curve 4 in Figure 8-5a).

In total 3,700 complete approach-retraction cycles were performed, until the signal disappeared, indicating that the molecule had become displaced from the tip. We have compiled all the approach and retraction traces for which the molecule was suspended from the tip into separate 2D-histograms without any selection, which are shown in Figure 8-5b,c respectively. The traces were shifted to zero along the x-axis at a conductance of $10^{-1}\,G_0$ before building the histograms. The histogram of the approach traces (Figure 8-5b) shows clearly that in the majority of approaches, the conductance increase monotonically above the low conductance state as far as $1\,G_0$. The high conductance state is visible as a small green protrusion around $10^{-2}\,G_0$, highlighting its low probability in the approach. Contrastingly, the 2D-histogram of the retraction traces (Figure 8-5c) shows that the high conductance state is much more prominent when retracting the tip. The histogram highlights that the high state tends to decrease slightly in conductance with increasing electrode separation, as does the low state.

Clearly, these results show that there are two stable states of the junction which are not totally dependent on the absolute tip-position, as the hysteresis shows, but that they do not occur at any random position. From the appearance of the image in Figure 8-4d, we can infer that one side of the molecule is strongly bonded to the

tip, leaving the other weakly bonded or freely suspended. This implies that the binding to the tip is relatively constant from one curve to another, so that the process responsible for the two states most likely takes place on the surface side of the junction.

Next, above the regions of conductance where plateaus develop (in both the approach and retraction traces), the tunneling region of the traces extends past $0.1\ G_0$, even going slightly above $1\ G_0$ in some cases. This is the range of conductance seen for the Au-C_{60}-Au junctions, as shown in Figure 8-2a-e, when we made contact to the fullerene anchor. However, with the molecule now located on the tip, there is no evidence of the formation of such junctions. This strongly suggests that the molecule is indeed not at the very apex of the tip, but situated just to one side. This binding geometry would allow the molecule to bind to the surface, but also allow Au-Au tunneling to dominate at close distances, as the molecule becomes squashed.

Due to the fact that the conductance beyond $0.1\ G_0$ is dominated by Au-Au tunneling, we can, therefore, estimate that the electrode separation at the point of closet approach is in the range 2-4 Å. This means the actual tip-substrate separation at the end of the high-plateau state should be between at least 1.2 to $1.4\ \mathrm{nm}$, and 1.6 to $1.8\ \mathrm{nm}$ in the case of the low state. The length of the fully stretched molecule is between $2.2\ \mathrm{nm}$ and $2.3\ \mathrm{nm}$. Hence, the discrepancy between the molecular length and the observed mean breaking distances agrees well with part of the molecule being adsorbed to the side of the tip. This also means we can rule out the possibility that the high conductance corresponds only to a single C_{60} as the conductance is at least one order of magnitude lower than measured previously for contact to the C_{60}, and the distance at maximum separation is too great.

8.3 DFT calculations on the single-C_{60} dumbbell junction

In order, therefore, to explain these observations, density functional calculations were carried out followed by a non-equilibrium Green's function scattering approach to investigate the transport, by the group of Prof. C.J. Lambert at Lancaster University). Here we summarize some of their results [Gillemot2013]. They investigated three models which are summarized as following:

The first model that was investigated is shown in Figure 8-6a and involves pulling the molecule up with the tip attached to one of the C_{60} groups. The resulting conductance trace shows a plateau region, below $10^{-5}\,G_0$, which is lower than the experimental value (see Figure 8-6b). Furthermore, no switching mechanism between high and low conductance values appears.

The second model that was checked is shown in Figure 8-6c where the current bypasses the tip-bound C_{60} and is injected directly into the fluorene backbone. In Figure 8-6e (red trace) we can see that this geometry results in a conductance of $10^{-2}\,G_0$ which is close to the experimental high state. Although this model explains the high conductance state observed in the experiment, it still doesn't explain the low conductance state. The possibility that the low-conductance state could correspond simply to conductance across the whole molecule with the molecule strongly fixed to the side of the tip is not likely, because direct charge injection to the fluorene would occur.

The third model checked is shown in Figure 8-6d and includes an extra adsorbed molecule (1, 2, 4-trichlorobenzene (TCB), which was used to deposit the molecule) between the surface-side C_{60} anchor group and the gold surface. Hence, it considers that the low-conductance state corresponds to the surface-side C_{60} in a 'pre-gold contact' position, sitting atop the layer of adsorbates on the surface. The resulting conductance trace in the presence of an adsorbate molecule is shown in Figure 8-6e (black trace). As shown when an adsorbate is inserted into the gap between the lower C_{60} and the substrate, the conductance is lower than the relaxed situation without the solvent molecule. In the experiments, we expect that as the dumbbell is

pushed towards the adsorbate, it will eventually displace it and touch the gold substrate.

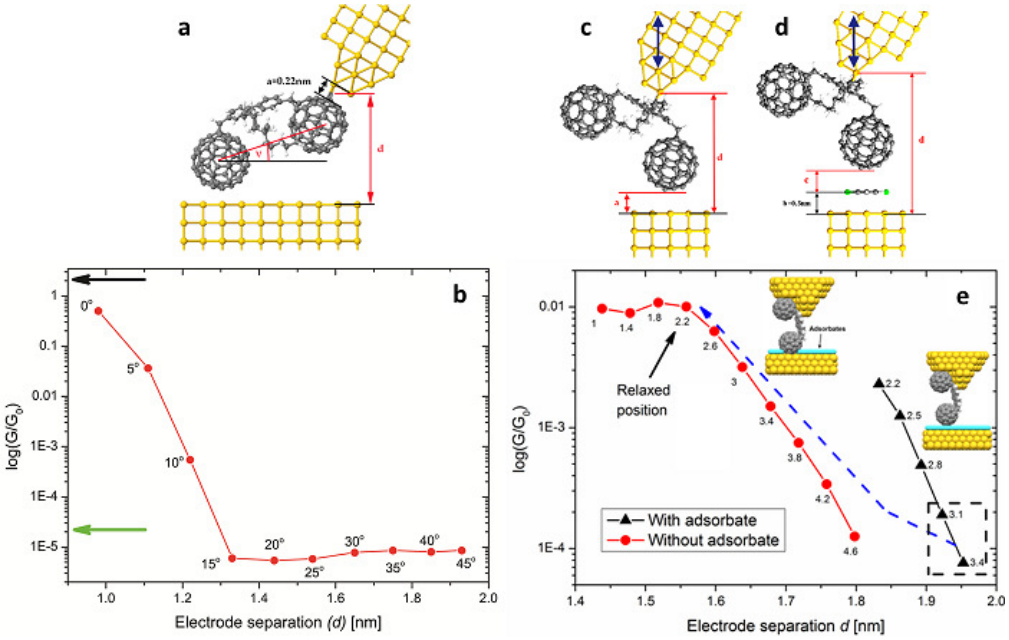

Figure 8-6: Density Functional Theory calculations. (by Prof. C.J. Lambert's group at Lancaster University) . (a) Schematic picture of the molecule being lifted up from the surface, with the moving variables are indicated with red color. The top electrode-molecule distance, a, was kept at a constant 0.22 nm, whilst d refers to the changing distance between the two electrodes, corresponding to the varying tilt angle (v). (b) Calculated conductance versus electrode separation, d, from theory for model in (a). The black arrow indicates the computed conductance of a single C_{60}, the green arrow the computed conductance of the molecule being wired while perpendicular to the Au surface (v=90°). (c) Schematic picture of the calculated molecule conducting through the backbone while lifted, with the top electrode-molecule distance kept fixed. Moving variables are indicated with red color. d refers to the electrode separation, and the molecule is only lifted, not tilted, throughout the sequence. (d) Schematic picture of the calculated molecule conducting through the backbone while lifted, but with a solvent "layer" separating it from the underlying Au surface. The top electrode-molecule distance is kept fixed. d refers to electrode separation, and c refers to the molecule-TCB distance. (e) Conductance versus electrode separation, d, for both geometries of (c) and (d), the red curve (filled circles) is the case without a solvent; the black curve (filled triangles) corresponds to the case with a solvent also present in the junction. The blue arrow represents the likely path for the solvent to leave the junction. The numbers next to the curves are the distances between the lower C_{60} and the solvent (for the black curve) and the Au surface (for the red curve) in Angströms. The black box represents the expected region for pi bonding.

As the common range for pi bonding in various systems is between 3.1-3.6 Å [Sinnokrot2002; Sygula2007], is therefore expected that the likely distance to which the dumbbell molecule can approach the extra molecule of solvent should be indicated by the black box in Figure 8-6e. In this region the conductance is on the order of $10^{-4}\,G_0$, which is the same order of magnitude as seen in the experiments.

The blue arrow represents the likely conductance transition pathway for the solvent to leave the junction. In the experiments, however, a continuous change in electrode separation is not seen due to the compliance of the junction. Instead, the transition is very sharp, manifesting in a sudden jump in conductance in both approach and retraction traces. This suggests that the molecule jumps through the layer in a single, fast step. When it does penetrate, it will be in a tilted or compressed state, so that when the molecule is pulled up, it will remain in the high-conductance state for a longer period than in the approach as a result of the recovery of the rotation/compression. When the molecule reaches its maximum extension in the high state, the adsorbate layer relaxes, and the molecule quickly returns to the top of the adsorbate layer. The conductance plateaus finally extend a little further before the molecule is completely lifted away from the surface. A diagram describing these steps is presented in Figure 8-7 with an example of approach (blue) retraction (red) experimental curve.

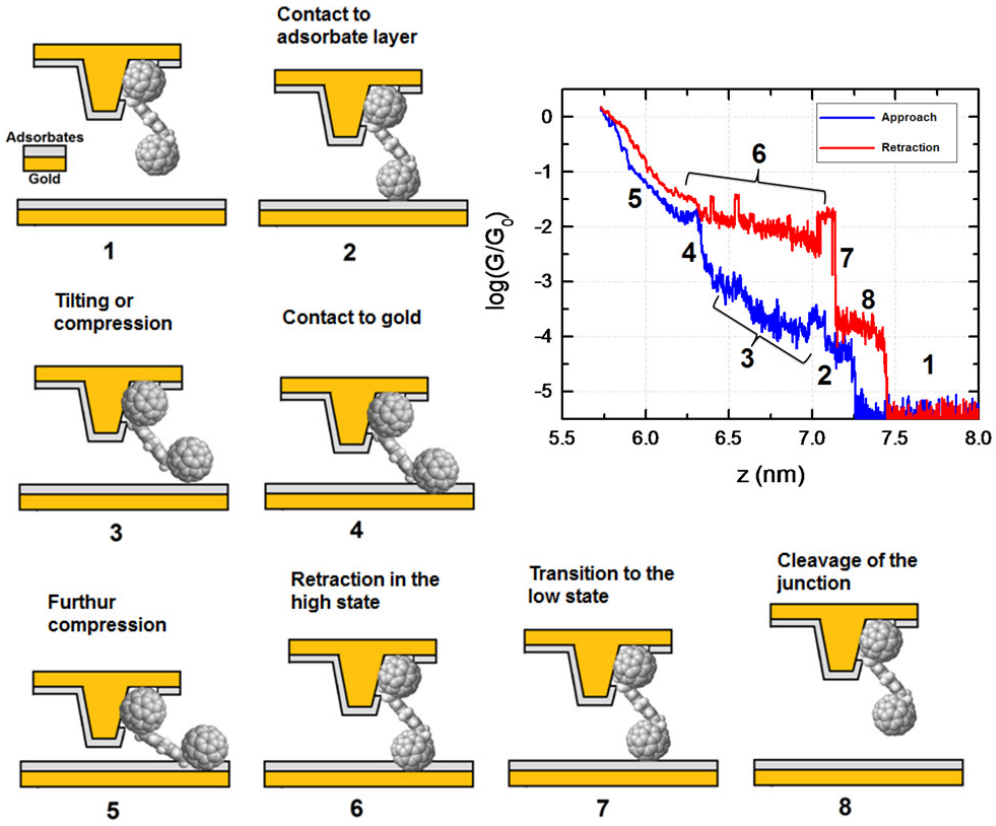

Figure 8-7: A simplified model of the molecule-electrode system in our experiment. During the entire cycle the central fluorene is in contact with the tip

8.4 Conclusions

In conclusion, we have investigated the junction formation and conductance of an isolated fullerene dumbbell molecule. By pressing the STM tip onto one of the C_{60} anchor groups, this sometimes results in the molecule being transferred to the tip. For one specific case the dumbbell was transferred to the tip at a vertically-wired configuration. With the molecule lifted we observed two main conductance states, a high conductance state close to $10^{-2}\ G_0$ and a lower state close to $10^{-4} G_0$. The theoretical calculations strongly suggest that the high conductance state corresponds to current injection directly into the fluorine bridge, thus the molecule is bound by the fluorine instead of the C_{60}. The low conductance state can be explained by a solvent monolayer, trapped between the surface and one C_{60} group, causing a dramatic reduction in the conductance.

References

[Arroyo2011] Arroyo, C. R., E. Leary, A. Castellanos-Gómez, G. Rubio-Bollinger, M. T. González, et al. (2011). "Influence of Binding Groups on Molecular Junction Formation." Journal of the American Chemical Society **133**(36): 14313-14319.

[Atienza-Castellanos2007] Atienza-Castellanos, C., M. Wielopolski, D. M. Guldi, C. van der Pol, M. R. Bryce, et al. (2007). "Determination of the attenuation factor in fluorene-based molecular wires." Chemical Communications(48): 5164-5166.

[Bilan2012] Bilan, S., L. A. Zotti, F. Pauly and J. C. Cuevas (2012). "Theoretical study of the charge transport through C_{60}-based single-molecule junctions." Physical Review B **85**(20): 205403.

[Eiermann1995] Eiermann, M., R. C. Haddon, B. Knight, Q. C. Li, M. Maggini, et al. (1995). "Electrochemical Evidence for Through-Space Orbital Interactions in Spiromethanofullerenes." Angewandte Chemie International Edition in English **34**(15): 1591-1594.

[French2012] French, W. R., C. R. Iacovella and P. T. Cummings (2012). "Large-Scale Atomistic Simulations of Environmental Effects on the Formation and Properties of Molecular Junctions." ACS Nano **6**(3): 2779-2789.

[Gillemot2013] Gillemot, K., C. Evangeli, E. Leary, A. La Rosa, M. T. González, et al. (2013). "A Detailed Experimental and Theoretical Study into the Properties of C60 Dumbbell Junctions." Small **9**(22): 3812-3822.

[Hong2011] Hong, W., D. Z. Manrique, P. Moreno-García, M. Gulcur, A. Mishchenko, et al. (2011). "Single Molecular Conductance of Tolanes: Experimental and Theoretical Study on the Junction Evolution Dependent on the Anchoring Group." Journal of the American Chemical Society **134**(4): 2292-2304.

[Kockmann2009] Kockmann, D., B. Poelsema and H. J. W. Zandvliet (2009). "Transport through a Single Octanethiol Molecule." Nano Letters **9**(3): 1147-1151.

[Kooistra2010] Kooistra, F. B., T. M. Leuning, E. Maroto Martinez and J. C. Hummelen (2010). "Two new types of [small pi]-conjugation between a fullerene sphere and an addend." Chemical Communications **46**(12): 2097-2099.

[Kumar2012] Kumar, A., R. Heimbuch, B. Poelsema and Z. H. J. W (2012). "Controlled transport through a single molecule." J. Phys. Condens. Matter **24**(8).

[Lafferentz2009] Lafferentz, L., F. Ample, H. Yu, S. Hecht, C. Joachim, et al. (2009). "Conductance of a Single Conjugated Polymer as a Continuous Function of Its Length." Science **323**(5918): 1193-1197.

[Leary2011] Leary, E., M. T. González, C. van der Pol, M. R. Bryce, S. Filippone, et al. (2011). "Unambiguous One-Molecule Conductance Measurements under Ambient Conditions." Nano Letters **11**(6): 2236-2241.

[Leary2009] Leary, E., H. Van Zalinge, S. J. Higgins, R. J. Nichols, F. Fabrizi de Biani, et al. (2009). "A molecular wire incorporating a robust hexanuclear platinum cluster." Physical Chemistry Chemical Physics **11**(25): 5198-5202.

[Lörtscher2007] Lörtscher, E., H. B. Weber and H. Riel (2007). "Statistical Approach to Investigating Transport through Single Molecules." Physical Review Letters **98**(17): 176807.

[Martin2008] Martin, C. A., D. Ding, J. K. Sørensen, T. Bjørnholm, J. M. van Ruitenbeek, et al. (2008). "Fullerene-Based Anchoring Groups for Molecular Electronics." Journal of the American Chemical Society **130**(40): 13198-13199.

[Matthias2012] Matthias, K., A. Francisco, J. Christian and G. Leonhard (2012). "Voltage-dependent conductance of a single graphene nanoribbon." Nature Nanotechnology **7**(11): 713-717.

[Mishchenko2010] Mishchenko, A., L. A. Zotti, D. Vonlanthen, M. Bürkle, F. Pauly, et al. (2010). "Single-Molecule Junctions Based on Nitrile-Terminated Biphenyls: A Promising New Anchoring Group." Journal of the American Chemical Society **133**(2): 184-187.

[Nichols2010] Nichols, R. J., W. Haiss, S. J. Higgins, E. Leary, S. Martin, et al. (2010). "The experimental determination of the conductance of single molecules." Physical Chemistry Chemical Physics **12**(12): 2801-2815.

[Reuter2012] Reuter, M. G., M. C. Hersam, T. Seideman and M. A. Ratner (2012). "Signatures of Cooperative Effects and Transport Mechanisms in Conductance Histograms." Nano Letters **12**(5): 2243-2248.

[Reuter2011] Reuter, M. G., T. Seideman and M. A. Ratner (2011). "Molecular Conduction through Adlayers: Cooperative Effects Can Help or Hamper Electron Transport." Nano Letters **11**(11): 4693-4696.

[Sinnokrot2002] Sinnokrot, M. O., E. F. Valeev and C. D. Sherrill (2002). "Estimates of the Ab Initio Limit for π−π Interactions: The Benzene Dimer." Journal of the American Chemical Society **124**(36): 10887-10893.

[Songmei2008] Songmei, W., G. Maria Teresa, H. Roman, G. Sergio, M. Marcel, et al. (2008). "Molecular junctions based on aromatic coupling." Nature Nanotechnology **3**(9): 569-574.

[Sygula2007] Sygula, A., F. R. Fronczek, R. Sygula, P. W. Rabideau and M. M. Olmstead (2007). "A Double Concave Hydrocarbon Buckycatcher." Journal of the American Chemical Society **129**(13): 3842-3843.

[Toher2011] Toher, C., R. Temirov, A. Greuling, F. Pump, M. Kaczmarski, et al. (2011). "Electrical transport through a mechanically gated molecular wire." Physical Review B **83**(15): 155402.

[Valkenier2014] Valkenier, H., C. M. Guedon, T. Markussen, K. S. Thygesen, S. J. van der Molen, et al. (2014). "Cross-conjugation and quantum interference: a general correlation?" Physical Chemistry Chemical Physics.

[Velizhanin2009] Velizhanin, K. A., T. A. Zeidan, I. V. Alabugin and S. Smirnov (2009). "Single Molecule Conductance of Bipyridyl Ethynes: The Role of Surface Binding Modes†." The Journal of Physical Chemistry B **114**(45): 14189-14193.

[Venkataraman2006] Venkataraman, L., J. E. Klare, I. W. Tam, C. Nuckolls, M. S. Hybertsen, et al. (2006). "Single-Molecule Circuits with Well-Defined Molecular Conductance." Nano Letters **6**(3): 458-462.

[Wang2009] Wang, C., A. S. Batsanov, M. R. Bryce, S. Martín, R. J. Nichols, et al. (2009). "Oligoyne Single Molecule Wires." Journal of the American Chemical Society **131**(43): 15647-15654.

[Wang2011] Wang, R. N., X. H. Zheng, L. L. Song and Z. Zeng (2011). "First-principles study on electron transport of carbon dumbbells C60-Cn-C60." The Journal of Chemical Physics **135**(4): -.

[Xu2003] Xu, B. and N. J. Tao (2003). "Measurement of Single-Molecule Resistance by Repeated Formation of Molecular Junctions." Science **301**(5637): 1221-1223.

[Zotti2010] Zotti, L. A., T. Kirchner, J.-C. Cuevas, F. Pauly, T. Huhn, et al. (2010). "Revealing the Role of Anchoring Groups in the Electrical Conduction Through Single-Molecule Junctions." Small **6**(14): 1529-1535.

General Conclusions

In this thesis scanning tunneling microscopy has been used to study thermoelectricity in molecular junctions at the fundamental level and explore routes to increase thermoelectric performance in these junctions.

A novel powerful experimental technique to measure the thermopower of single-molecule junctions has been developed. This technique expands the instrumental capabilities of a Scanning Tunneling Microscope (STM) to enable the simultaneous measurement of electrical transport and thermopower during the formation and evolution of a molecular junction. This work goes beyond the-state-of-the-art and opens the way to in situ engineering of the thermoelectric performance of molecular junctions.

The power of this technique was demonstrated, in particular, in C_{60} junctions where the enhancement of thermopower by molecular manipulation was shown. In contrast to previously reported experimental results, by imaging the sample prior to junction formation, the exact number of molecules in the junction is known. We formed single- and double-C_{60} junctions controllably and we measured simultaneously, the thermopower and conductance during the whole evolution of the junction. We observed that the thermopower of a C_{60} molecule can be doubled by coupling two C_{60} molecules. DFT-based calculations by Prof. C.J. Lambert's group show that the thermopower can be further doubled by coupling to a third C_{60}. The figure of merit ZT shows a 4-fold and a 16-fold increase, for two and three C_{60}s respectively with respect to one C_{60}. Our results demonstrate the possibility of engineering the thermopower of a molecular junction by mechanical manipulation.

The role of the electronic structure in determining the thermopower in nanoscale of metallic contacts was evidenced. This system offers the unique possibility of investigating how thermoelectricity is continuously modified from bulk all the way down to the atomic scale where quantum effects dominate. We found that the thermopower, changes not only its magnitude but also its sign when the contact size dimensions are reduced to the size of a single atom. Moreover, we find that in

the case of gold, the thermopower of a few-atom contact exhibits a series of minima correlated with the maxima of the conductance, in marked contrast with the platinum wires where such oscillations are absent. Coherent transport theoretical calculations by Prof. J.C. Cuevas' group, demonstrate that the different behaviour of the two metals can be explained in terms of their different electronic structure.

Furthermore, the enhancement of the thermopower without affecting the conductance by modifying the chemical structure of OPEs molecules was demonstrated. More specifically, by incorporating a dithiafulvalene unit to the OPE backbone, we introduce a Fano resonance in the transmission spectrum close to the Fermi level. Introducing a second unit moves the Fano resonance closer to the Fermi level, enhancing the Seebeck coefficient. In contrast, previous strategies suggested for improving the thermopower, were also causing modification of conductance. We have also observed, that the thermopower of a molecular junction is sensitive to strain increasing as the molecule is stretched.

Finally, the use of C_{60} as a linker in molecular junctions was explored by investigating the junction formation and conductance of an isolated fullerene dumbbell molecule. By pressing the STM tip onto one of the C_{60} anchor groups, this sometimes results in the molecule being transferred to the tip. For one specific case the dumbbell was transferred to the tip at a vertically-wired configuration. With the molecule lifted we observed two main conductance states; a high conductance state close to $10^{-2}\,G_0$ and a lower state close to $10^{-4}\,G_0$. The theoretical calculations by Prof. C.J. Lambert's group strongly suggest that the high conductance state corresponds to current injection directly into the fluorine bridge, thus the molecules are bound by the fluorine instead of the C_{60}. The low conductance state can be explained with a solvent monolayer, trapped between the surface and one C_{60} group, causing a dramatic reduction in the conductance.

Conclusiones Generales

En esta tesis hemos utilizado un microscopio de efecto túnel para estudiar termoelectricidad en uniones moleculares a nivel fundamental y explorar nuevas rutas para incrementar el rendimiento termoeléctrico en estas uniones.

Se ha desarrollado una innovadora y potente técnica experimental para medir thermopower de uniones moleculares formadas por una única molécula. Esta nueva técnica amplía la capacidad instrumental de un Microscopio de Efecto Túnel (STM) para permitir la medida simultánea de transporte eléctrico y thermopower durante la formación y evolución de una unión molecular. Este trabajo va más allá de los últimos avances en el campo y abre el camino para hacer ingeniería *in situ* del rendimiento termoeléctrico de uniones moleculares.

El potencial de esta técnica se ha demostrado, en particular, en uniones de moléculas C_{60} donde se ha mostrado el incremento del thermopower mediante manipulación molecular. En contraste con resultados experimentales publicados previamente, mediante la toma de imágenes antes de la formación de la unión molecular se conoce el número exacto de moléculas en la unión. Se han formado de manera controlada uniones de C_{60} compuestas por una y dos moléculas y se ha medido simultáneamente el thermopower y la conductancia durante toda la evolución de la unión. Hemos observado que el thermopower de una molécula C_{60} puede doblarse mediante el acoplamiento de dos C_{60}. Cálculos de DFT realizados por el grupo del Prof. C.J. Lambert muestran que el thermopower puede ser doblado de nuevo mediante el acoplamiento de una tercera molécula C_{60}. En comparación con un único fullereno, el factor 'figure of merit' ZT resulta 4 y 16 veces mayor para dos y tres C_{60}, respectivamente. Nuestros resultados demuestran la posibilidad de hacer ingeniería con el thermopower de una unión molecular mediante manipulación mecánica.

Se ha probado también el papel de la estructura electrónica al determinar el thermopower en la nanoescala de contactos metálicos. El sistema ofrece la posibilidad única de investigar cómo se modifica progresivamente la

termoelectricidad desde el volumen hasta la escala atómica, donde dominan los efectos cuánticos. Hemos demostrado que el thermopower cambia no sólo de magnitud, sino también de signo, cuando las dimensiones del contacto se reducen hasta el tamaño de un único átomo. Además, encontramos que en el caso del oro, el thermopower de un contacto formado por unos pocos átomos presenta una serie de mínimos correlacionados con los máximos de conductancia, en un marcado contraste con los contactos de platino donde dichas oscilaciones no aparecen. Cálculos teóricos de transporte coherente realizados por el grupo del Prof. J.C. Cuevas demuestran que el comportamiento diferente de estos dos metales se puede explicar en términos de sus diferentes estructuras electrónicas.

Además, se ha demostrado el incremento del thermopower sin reducir la conductancia mediante la modificación de la estructura química de moléculas OPE. Más concretamente, gracias a la incorporación de un ditiolfulvaleno a la columna del OPE, introducimos una resonancia Fano en el espectro de transmisión cerca del nivel de Fermi. Añadir una segunda unidad mueve la resonancia Fano aún más cerca del nivel de Fermi, aumentando el coeficiente Seebeck. En contraste con estos resultados, estrategias previas propuestas para mejorar thermopower también producían una modificación de conductancia. También hemos observado que el thermopower de una unión molecular es sensible a la tensión, aumentando según se estira la molécula.

Finalmente, se ha explorado el uso del C_{60} como enlace en uniones moleculares mediante la investigación de la formación de la unión y la conductancia de moléculas dumbbell aisladas. Presionar la punta del STM sobre uno de los grupos de anclaje C_{60} a veces resulta en la transferencia de la molécula a la punta. En un caso específico, el dumbbell es transferido a la punta con una configuración vertical. Con la molécula alzada en la punta, observamos dos estados principales de conductancia, un estado de conductancia elevada cercana a $10^{-2}\ G_0$ y un estado más bajo cercano a $10^{-4}\ G_0$. Los cálculos teóricos realizados por el grupo del Prof. C.J. Lambert sugieren que el estado de alta conductancia corresponde a la inyección de corriente directamente en el puente de fluorina, por lo que la molécula se enlaza por la fluorina en lugar del C_{60}. El estado de baja conductancia puede explicarse con

una monocapa de disolvente atrapada entre la superficie y uno de los grupos C_{60}, lo que provoca una dramática reducción de la conductancia.

Appendices

Appendix A Piezotube calibration

The piezotube (PZT) needs to be calibrated in order to know the tip's x, y, z movement in distance units for an applied voltage. We scan samples with known periodic patterns, in constant current mode, and get the spatial images in units of voltage applied to the PZT for the x, y, z movement. Then we compare known distances of the pattern with the voltage units of the image and extract the displacement of the PZT per volt, $K_{x,y,z} = \frac{\Delta x,y,z}{\Delta V}$. We follow the same procedure for the two tip holders, with and without the heater.

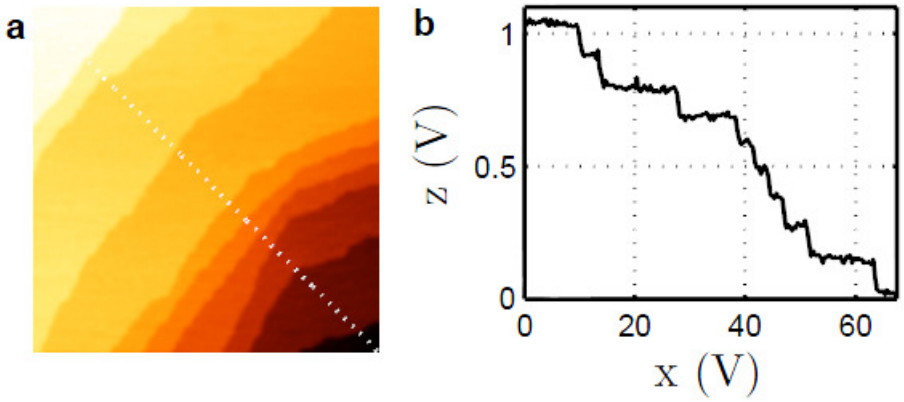

Figure A-1: z calibration of the piezotube. (a) Image of atomically flat gold terraces separated by monoatomic steps and (b) the profile of the image on the white line of the image.

For the z calibration a common pattern to use is the monoatomic steps of gold (111) surface with height of $0.24\ \mathrm{nm}$ (see Figure A-1a). By averaging values of the height of the monoatomic steps from cross sections (see Figure A-1b) for different areas of the gold sample we calculated $K_z = 2.2\ \mathrm{nm/V}$. The same value was found for both configurations, with and without heater.

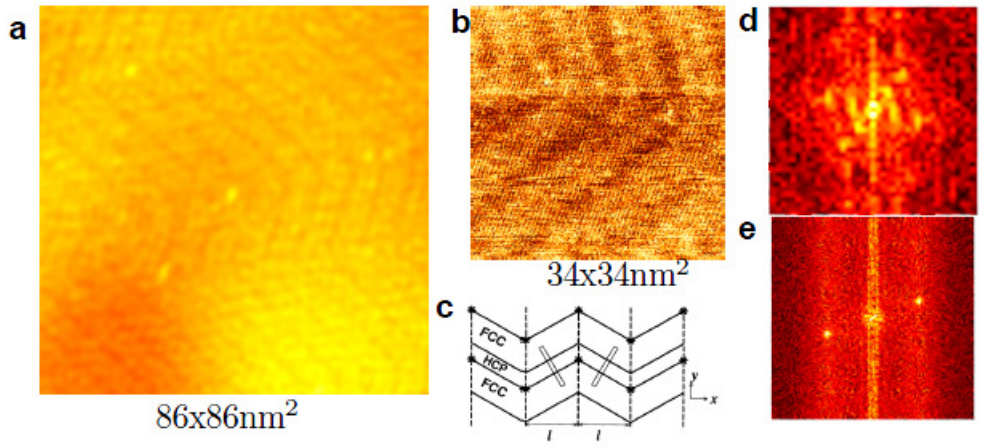

Figure A-2: x,y calibration of the piezotube without heater. (a) Image of reconstructed gold (111) surface. (b) A zoom image where the pairs of zigzag parallel lines of the reconstruction can be seen. (c) Schematic drawing of the herringbone reconstruction x-axis is along $[\bar{1}10]$ and y axis along $[\bar{1}\bar{1}2]$. The regions of FCC and HCP lattice are shown [Narasimhan1992]. (d) 2D-Fourier Transform (FT) ($1.6\text{x}1.6\ \text{nm}^{-1}$) of image (b) in low frequencies with the bright spots corresponding to the zigzag lines. (e) 2D-FT $10\text{x}10\ \text{nm}^{-1}$ of image (a) for higher frequencies with the bright spots corresponding to the gold atomic rows.

For the x, y calibration of the piezotube with only the tip mounted, we used a gold (111) sample. Gold exhibits a reconstruction of the close-packed (111) surface, called "herringbone" reconstruction. The surface atoms rearrange and give an ordered array of boundaries between surface regions with fcc-stacking and hexagonal-close-pack (hcp) stacking [Wöll1989]. This rearrangement can be seen in a STM image, as a periodic pattern of arranged zigzag parallel lines in the $[1\bar{1}0]$ direction. The distance between neighbored pairs is $6.3\ \text{nm}$ and between individual lines within a pair is $4.4\ \text{nm}$ [Barth1990]. Figure A-2c shows a schematic of the "herringbone" reconstruction [Narasimhan1992].

In Figure A-2a,b examples of scans taken of reconstructed areas of gold surface are shown. In the 2D-FT image two main features can be distinguished: for low frequencies (Figure A-2d) 2 pairs of bright spots corresponding to the different directions for the zigzag lines of the reconstruction and for higher frequencies 2 bright spots corresponding to the atomic rows of the gold (Figure A-2e). The angle

between the two lines connecting each pair in the low frequencies is 120^o and the distance between them is equal. For the calculation of the x, y calibration we measured the distance in several of our images in volt units (volts applied to the piezotube) between neighboured pairs of the reconstruction. While this distance is known to be 6.3 nm, we extracted $K_{x,y} = 5.1\,\mathrm{nm/V}$ for the x, y calibration.

For the x, y calibration of the configuration with the tip holder with incorporated heater we used graphene on SiO_2. We used the atomic resolution image which was corrected for thermal drift, shown in Figure A-3b (see Appendix B for the drift correction). While the spacing of the hexagonal lattice of graphene is known to be 0.246 nm [Castro Neto2009], we got $K_{x,y} = 7.58\,\mathrm{nm/V}$.

We can compare this calibration with that obtained of the formulas that already exist in the literature for the displacement of a PZT with [Yang1998] and without [Chen1992] the tip mount on it. For a piezoelectric tube the z displacement for an applied voltage ΔV, can be calculated with the formula [Chen1992]

$$\Delta z = \frac{d_{31} V_z l}{h}, \qquad \text{Equation A-1}$$

where l is the length, h is the wall thickness and d_{31} is the relevant piezoelectric coefficient of the piezoelectric tube.

The x and y deflections of the tube scanner when applying two equal and opposite voltages on the two opposite quadrants ($V = V_{+x,-y} = -V_{-x,-y}$) are given by [Chen1992]:

$$\Delta x, y = \frac{2\sqrt{2} d_{31} V l^2}{\pi D h}, \qquad \text{Equation A-2}$$

where D is the inner diameter of the piezoelectric tube.

The above formulas don't take in to account the influence of the tip on the lateral movement of the PZT. In a STM we are interested in the displacement of the scanner and thus the displacement of the tip. The tube deflects by bending and the free end where the tip is mounted is tilted and this will cause a further lateral shift. Also if the tip is not mounted on the center of the tube then there is a coupling between z movement and x, y movement and, as a result, when the tube deflects

in the x, y direction the z movement of the tip end will vary depending on the position of the tip with respect to the center of the tube. By applying simple geometry, the above formulas can be modified to include the effect of the tip to the displacement [Yang1998]:

$$\Delta z = \frac{d_{31} l}{h}\left[\lambda\left(V_x x_t + V_y y_t\right) + V_z\right], \qquad \text{Equation A-3}$$

where $V_{x,y} = V_{+x,-y} - V_{-x,-y}$ and $\lambda = 4\sqrt{2}(R_2^3 - R_1^3)/[4\pi(R_2^4 - R_1^4)]$ with R_1 and R_2 the inner and outer radius of the piezotube respectively. x_t and y_t is the position where the tip is mounted on the end of the piezotube with respect to its center, and

$$\Delta x, y = \frac{2\sqrt{2} d_{31} V l^2}{\pi D h}\left(1 + \frac{l_t}{l}\right), \qquad \text{Equation A-4}$$

where l_t is the tip length.

We applied Equation A-3 and Equation A-4 for the calculation of the piezoelectric constant of our piezotube using the manufacturer parameters ($l = 1.62 \times 10^{-2}\ \mathrm{m}, h = 0.1 \times 10^{-2}\ \mathrm{m}, R_1 = 0{,}85 \times 10^{-2}\ \mathrm{m}, D = 0{,}95 \times 10^{-2}\ \mathrm{m}, d_{31} = 1.73 \times 10^{2-10}\ \mathrm{m}$) [Inc.] and with an average tip length $l_t \approx 0.3 \times 10^{-2}\ \mathrm{m}$ we found $K_z = 2.82\ \mathrm{nm/V}$, $K_{x,y} = 5.76\ \mathrm{nm/V}$. When the tip holder with the incorporated heater is mounted on the piezotube we have to consider an extended tip, with its length equal to the sum of the heater and tip length $l_{ht} = l_h + l_t \approx 1.1 \times 10^{-2}\ \mathrm{m}$ and the piezoelectric constant changes to $K_z = 2.82\ \mathrm{nm/V}$, $K_{x,y} = 8.15\ \mathrm{nm/V}$. In both cases we consider that the tip is centered on the tube ($x_t = y_t = 0$). Table A-1 shows a summary of the values for the calibration extracted from the images and from the formulas. It seems that the formulas are overestimating the piezoelectric constants, but they are a very useful tool for the first estimation of the calibration of a PZT.

Table A-1: Piezoelectric constants. Extracted from the formulas and from the images, for configuration with the heater and with just the tip.

	Equations for PZT displacement with tip mounted		*Images*	
	Tip	**heater**	**Tip**	**Heater**
$K_{x,y}$ $(^{\mathrm{nm}}/_{\mathrm{V}})$	5.8	8.2	5.1	7.6
K_z $(^{\mathrm{nm}}/_{\mathrm{V}})$	2.8	2.8	2.2	2.2

References

[Barth1990] Barth, J. V., H. Brune, G. Ertl and R. J. Behm (1990). "Scanning tunneling microscopy observations on the reconstructed Au(111) surface: Atomic structure, long-range superstructure, rotational domains, and surface defects." Physical Review B **42**(15): 9307-9318.

[Castro Neto2009] Castro Neto, A. H., F. Guinea, N. M. R. Peres, K. S. Novoselov and A. K. Geim (2009). "The electronic properties of graphene." Reviews of Modern Physics **81**(1): 109-162.

[Chen1992] Chen, C. J. (1992). "Electromechanical deflections of piezoelectric tubes with quartered electrodes." Applied Physics Letters **60**(1): 132-134.

[Inc.] Inc., E. P. Piezoceramic Tubes For Ultra-precise Positioning Applications. E. P. Inc.

[Narasimhan1992] Narasimhan, S. and D. Vanderbilt (1992). "Elastic stress domains and the herringbone reconstruction on Au(111)." Physical Review Letters **69**(10): 1564-1567.

[Wöll1989] Wöll, C., S. Chiang, R. J. Wilson and P. H. Lippel (1989). "Determination of atom positions at stacking-fault dislocations on Au(111) by scanning tunneling microscopy." Physical Review B **39**(11): 7988-7991.

[Yang1998] Yang, S. and H. Wenhao (1998). "Three-dimensional displacements of a piezoelectric tube scanner." Review of Scientific Instruments **69**(1): 226-229.

Appendix B Drift estimation

The most common reason for a distortion in a topographic image acquired with STM at room temperature is the microscope tip drift with respect to; the sample due to thermal expansion of the STM parts, the drift of the electronic amplifiers and the creep of the piezoelectric elements. The x, y drift velocity can be separated into two components: the constant and the time-dependent. The drift velocity can change, in ambient conditions at room temperature, due to change of the environmental temperature, although this nonlinear distortion is much smaller than the linear one [Yurov1994]. The linear velocity of the drift can be estimated in two ways: By imaging a known periodic surface structure or by taking images of an area with a certain structure in different time intervals.

As a known periodic structure we imaged graphene on SiO_2 shown in Figure A-3a. The hexagonal pattern of graphene is distorted due to the thermal drift, mainly in the y scan axis, which is the slow axis of the scanning and the drift velocity is smaller than the scanning velocity, while in the fast x scanning axis, the drift velocity is greater. In the 2D Fourier transform (2D-FT) image of graphene, six bright spots appear which form a hexagon and each pair of opposite spots denotes the symmetrical direction of graphene lattice. The frequency difference for each pair should be equal since the periodicity of the lattice is the same in all directions [Castro Neto2009]. To remove the contribution of the drift from the image we need to know the drift velocity. By knowing that and the time difference between the scanning points with respect to the beginning of the image we can compose the real image by using the equations

$$\begin{aligned} X_{real} &= X_{scan} + U_{xdr}T, \\ Y_{real} &= Y_{scan} + U_{ydr}T, \end{aligned} \qquad \text{Equation A-5}$$

where T is the matrix of the time interval, for each point of the image, from the first point. X_{scan} and Y_{scan} are the matrices of the coordinates we know from the movement of the piezotube. X_{real} and Y_{real} are the matrices of the coordinates of the real area of the surface that we scanned. U_{xdr} and U_{ydr} are the velocities of the drift in the x and y directions respectively.

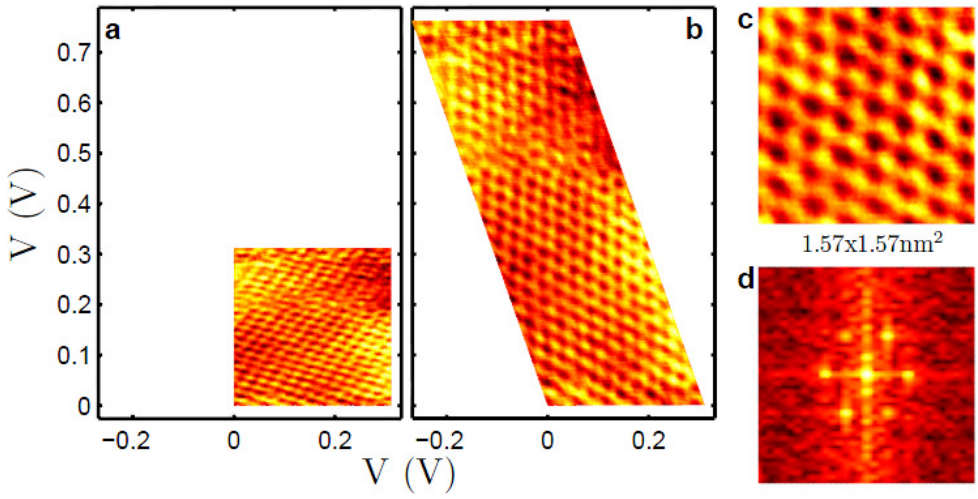

Figure A-3: Drift estimation from an atomic resolution image of graphene. (a) Atomic resolution image of graphene as taken. (b) Image corrected for drift. (c) A zoom in an area of image (b). (d) 2D-FT ($40\text{x}40\ \text{nm}^{-1}$) image where the bright spots form a hexagon due to the periodic structure of graphene.

For a distorted spatial image of graphene, the hexagon in the 2D-FT domain will be distorted as well. Since the drift velocity is not known we can estimate it by applying different values to the Equation A-5 and build up the real image to get a hexagon in the 2D-FT. The resulting image of the 2D-FT is shown in Figure A-3d, the corrected spatial image in Figure A-3b, and a zoom of that image in Figure A-3c. The values for the drift velocity we found were $U_{xdr} = -0.003\ \text{nm}/s$ and $U_{ydr} = 0.0065\ \text{nm/s}$ in the x and y directions respectively which gives $U_{drift} \approx 0.0076\, nm/s$ for the drift vector.

Another way of estimating the drift velocity is to take images of an area with a certain structure in different time intervals. While the movement of the tip is known from the voltage applied to the PZT, we extract the coordinates of a certain characteristic point of all the images corresponding to different times. By plotting the times with the position, once the plot is linear, the drift speed will be equal to the slope. An example is shown in Figure A-4, where we choose the point shown by the green circle in the first image and we plot its relative distance and relative time

interval with respect to the first image. Points marked with a,b,c refer to the corresponding image a,b,c. The relation between the distance and the time is linear, thus the speed velocity is constant with a value of $U_{drift} \approx 0.001\, nm/s$. Since the microscope functions at room temperature in ambient conditions, the drift differs for different experiments but usually it is in the order of a few Angstroms per min.

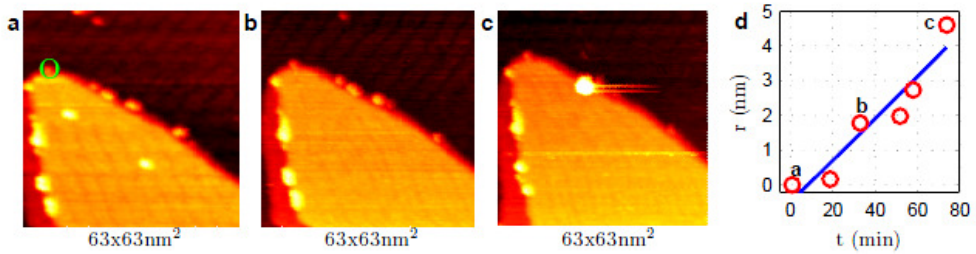

Figure A-4: Measuring the drift by consecutive images. (a-c) Images taken in different time intervals at the same position as specified by the voltage applied to the piezotube. Due to the drift the features of the area are displaced over time. (d) distance that the point shown by green circle in the first image shifted by time. Points a,b and c where extracted from images a,b,c respectively.

The minimization of the drift of this STM is succeeded because: of its symmetric geometry and is placed in a box with isolation sponge that keeps the temperature quite stable (see Figure A-5).

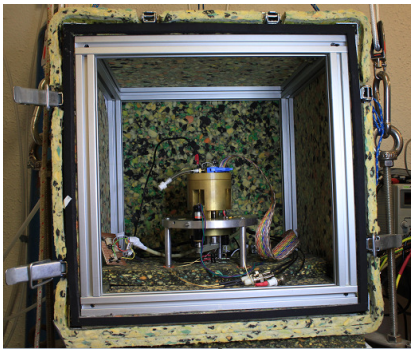

Figure A-5: Photo of the box where STM is placed. The box is metallic with isolation sponge inside and outside.

References

[Castro Neto2009] Castro Neto, A. H., F. Guinea, N. M. R. Peres, K. S. Novoselov and A. K. Geim (2009). "The electronic properties of graphene." Reviews of Modern Physics **81**(1): 109-162.

[Yurov1994] Yurov, V. Y. and A. N. Klimov (1994). "Scanning tunneling microscope calibration and reconstruction of real image: Drift and slope elimination." Review of Scientific Instruments **65**(5): 1551-1557.

Appendix C Tip temperature calibration

In thermopower measurements we monitor the temperature difference between the tip and the substrate. The ideal way to do that would be by adjusting one thermocouple, with the one junction in contact with the tip and the other with the sample. Nevertheless, establishing a good thermal contact between the tip and the junction of a thermocouple is difficult due to the small size of the tip.

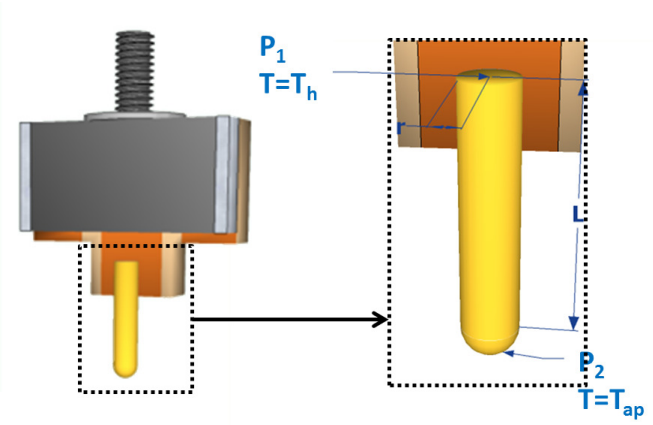

Figure A-6: Schematic of the tip holder with incorporated heater. indicating the dimensions and points where the temperature was measured (T2) and the point where the temperature is estimated (T1).

The closest point to the tip where we can adjust a thermocouple is the point where the tip is soldered (tip base) on the tip-holder. By knowing this temperature, we have to estimate the heat loses through conduction (Q_{cond}) with the air molecules and convection (Q_{conv}) because of the air flow in order to estimate the temperature at the apex of the tip. Thus overall the heat flow is given by:

$$Q_{All} = Q_{conv} + Q_{cond}. \qquad \text{Equation A-6}$$

An upper bound of the heat lost to the surroundings is to consider the heat flow to be just from the apex of the tip (point P2 at Figure A-6) with temperature T_h.

First we calculate the heat flow through conduction to the surroundings by considering the tip as a black body. According to the Stefan-Boltzmann law the energy radiated per unit surface area [Griffiths1995] of a non-ideal black body across all wavelength per unit time is proportional to the fourth power of the absolute temperature $\frac{Q_{cond}}{\alpha} = \varepsilon\sigma T^4$, where σ is the Stefan-Boltzman constant and ε is the emissivity of the material and α the surface. For radiation to the surroundings the formula is given by:

$$Q_{cond} = \alpha\varepsilon\sigma\left(T_h^4 - T_c^4\right), \qquad \text{Equation A-7}$$

where T_c is the temperature of the environment.

We consider the apex of the tip to be a semi-sphere, so that α is equal to the surface of a semi-sphere. The radius of the tip is $r = 0.00025\ \mathrm{m}$ so that $\alpha = 2\pi r^2 = 3.927 \times 10^{-7}\ \mathrm{m}^2$. The usual temperature of the hot tip used in our experiments is $T_h = 340\ \mathrm{K}$, and the room temperature is $T_c = 300\mathrm{K}$ for the surroundings. By using the values $\varepsilon = 0.02$ for gold and the Stefan Boltzman constant $\sigma = 5.67 \times 10^{-8}\ \mathrm{Wm^{-2}K^{-4}}$ we get $Q_{cond} \approx 2.34 \times 10^{-6}\ \mathrm{W}$.

Then we calculate the heat flow through convection to the surroundings by the formula:

$$Q_{conv} = h\alpha(T_h - T_c), \qquad \text{Equation A-8}$$

where h is the convective heat transfer coefficient (units $\mathrm{Wm^{-2}K^{-1}}$) which depends on the shape and orientation of the object. A typical value for a vertical cylinder is $h = 10\ \mathrm{Wm^{-2}K^{-1}}$ [Nilesh2013].

We find that $Q_{conv} = 1.57 \times 10^{-4}\ \mathrm{W}$ which is two orders of magnitude higher than the Q_{cond} and so we can write: $Q_{All} \approx Q_{conv}$.

In order to calculate the temperature at the apex of the tip we use the formula for heat conduction within a material [Datta2005]:

$$Q_{All} = \frac{kA}{L}(\Delta T) \approx Q_{conv}, \qquad \text{Equation A-9}$$

where *k* is the thermal conductivity, A is the surface area of the tip, L the thickness and ΔT the difference of temperature between the tip base and the apex, $T_c - T_{ap}$.

By using the parameters $A = 2\pi rL = 6.042 \times 10^{-6}\ \mathrm{m}^2$, $r = 0.00025\ \mathrm{m}$, $L = 0.004\ \mathrm{m}$, $k = 317\ {}^{\mathrm{W}}/_{\mathrm{mK}}$ for the gold tip we get that $\Delta T = 3.3 \times 10^{-5}\ \mathrm{K}$ which is very small and practically means that the apex of the tip has the same temperature with the tip base.

In addition to this small drop of temperature, another drop is expected to appear when the tip is closed to the sample, which is kept in room temperature T_c, due to heat transport because of conduction through air and conduction through the organic molecules which may be bridging the gap between the substrate and the tip. It has been calculated by Reddy et al [Reddy2007] that even when the tip-substrate gap is reduced to $1\ \mathrm{nm}$, the temperature at the very end of the tip will be $T_{ap} \approx T_h - 0.01(T_h - T_c)$, which is less than one percent of the temperature differential applied across the substrate and tip.

During the experiments we monitor the temperature difference between the heater (resistor) and the substrate. Then, while the temperature at the tip base and at the apex of the tip is the same, we just need to estimate the temperature drop between the resistor and tip base. To calibrate that, we used three type-k chromel - alumel thermocouples. The one junction of every thermocouple was always placed on the body of the microscope and the other on the tip holder, the heater and the sample, respectively. With the one on the sample we check the effect of the heat radiated from the heater to the gold sample. Then by increasing the temperature of the heater and keeping the tip in tunneling with the sample we measure the temperature of the different points mentioned above. In Figure A-7a,b the points where the thermocouples were adjusted are indicated by arrows.

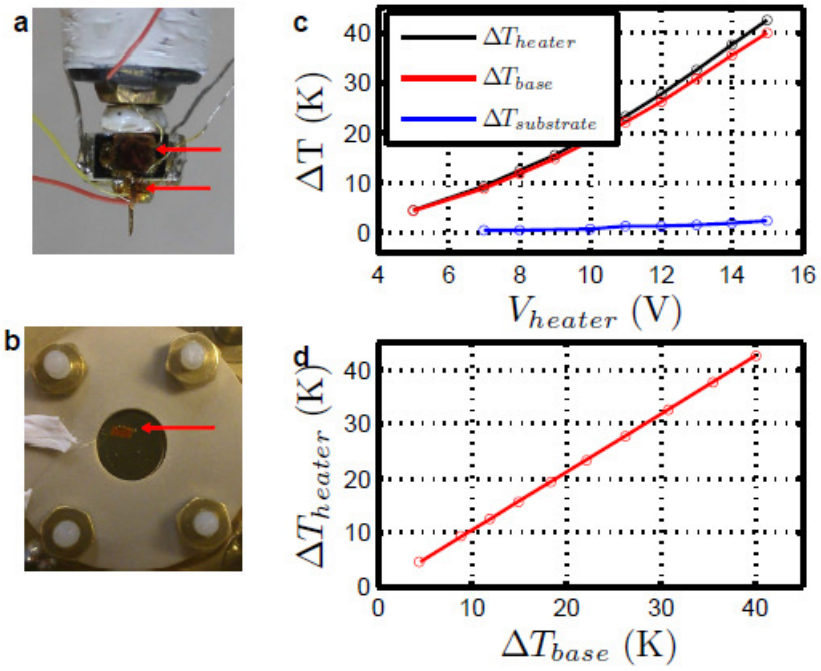

Figure A-7: Tip temperature estimation. (a,b) Pictures showing the different points where the thermocouple junctions were placed: on base of the tip and the resistor (a) and on the gold substrate (b). (c) Temperature difference heater-body (black), holder-body (red) and gold substrate-body (blue) versus voltage applied to the heater. (d) linear relation between the temperature of the heater and of the base of the tip.

The temperature difference with respect to the metallic body of the STM measured on the heater, tip holder and the sample surface are plotted as a function of the voltage applied to the heater in Figure A-7c. Comparing the curves for the heater and the tip base we observe a small drop of temperature between the two. The relation between the two temperatures is linear (Figure A-7d), which indicates that the temperature drop appears because of the imperfect thermal contact of the resistor to the metal where the tip is soldered. This drop is constant as we checked it in several series of measurements. The temperature of the gold sample surface on the other hand, is increasing slightly while the tip temperature increases, because of the heat radiation from the heater and the tip.

Finally, we checked how the temperature of the tip varies if it is in tunneling or in contact with the sample. For junctions with conductance of the order of $\sim 100\ G_0$ no changes where observed. A small drop of the temperature of the order of 2% was observed by creating macroscopic metallic junctions using the coarse movement of the tip.

Consequently, in this thesis, when the temperature difference was measured between the heater and the sample we discounted the loss of heat due to the thermal contact of the resistor to the metal where the tip is soldered.

References

[Datta2005] Datta, S. (2005). Quantum Transport: Atom to Transistor, Cambridge University Press.

[Griffiths1995] Griffiths, D. J. (1995). Introduction to Quantum Mechanics, Prentice Hall.

[Nilesh2013] Nilesh, M., Nanasaheb, Vijay and S. Totala, Shete,Bhopate (2013). "Natural Convection Characteristicsin Vertical Cylinder." International Journal Of Engineering And Science **3**(8): 27-31.

[Reddy2007] Reddy, P., S.-Y. Jang, R. A. Segalman and A. Majumdar (2007). "Thermoelectricity in Molecular Junctions." Science **315**(5818): 1568-1571.

Appendix D Thermopower offset due to the tip-connecting lead

By heating the tip we not only establish a temperature difference between the tip and the substrate of the STM but also a temperature gradient across the tip connecting lead that gives rise to an additional thermoelectric voltage, $S_{lead}(T_c - T_h)$, where S_{lead} is the thermopower of the lead, T_c is the temperature of the substrate and $T_h = T_c + \Delta T$ is the temperature of the tip (see the equivalent thermal circuit in Figure A-8). To estimate this voltage we measured the macroscopic absolute thermopower of bulk Platinum (Pt) and gold (Au) wire which is well known in the literature [Cusack1958; Huebener1964; Huebener1965; Soni2008].

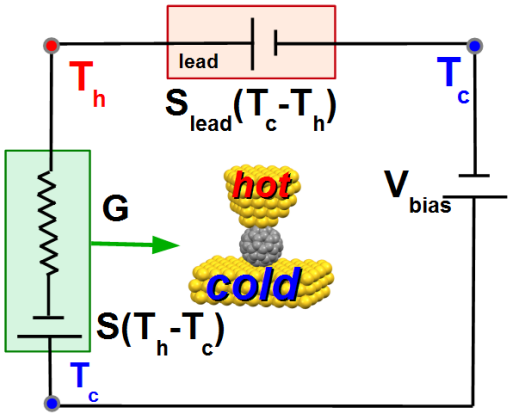

Figure A-8: Equivalent thermal circuit of the setup for the calculation of the thermopower. The substrate and body of the STM are at ambient Temperature T_c while the tip is heated to a temperature of $T_h = T_c + \Delta T$ above ambient temperature. S is the thermopower of the molecular junction and S_{lead} is the thermopower tip connecting lead. V_{bias} is the bias voltage imposed by the control electronics of the STM.

We soldered the one end of the wire (Pt or Au with diameter of 0.07 and 0.25 mm respectively) at the tip holder, and the other to the connection for applying the bias voltage at the STM. In this way we keep exactly the same cables and connections of the STM, and we just replace the STM junction with the bulk material. The cable normally connected with the IV converter and the one with the card for applying the bias voltage, are now connected directly to a Keithley 2000 multimeter.

A temperature gradient is applied to the metallic wire by heating the one end with the heater and keeping the other end in thermal contact with the body of the microscope. For different temperature gradients we measure the voltage difference between the two ends of the wire with a Keithley 2000 multimeter. We extract the measured absolute thermopower for each temperature from the corresponding equations: $S_{mPt} = -0.018\Delta T - 5.14$ and $S_{Aum} = -0.0021\Delta T + 1.89$, calculated from the experimental data by fitting a quadratic line [Huebener1965] following the idea of Equation 2-9.

The absolute thermopower values ($S_{mPt}(T)$, $S_{mAu}(T)$) for temperatures measured are plotted in Figure A-9a,b with magenta, and with the blue line the accepted thermopower values from the literature ($S_{Pt}(T)$, $S_{Au}(T)$) [Cusack1958]. There is a shift in our values with respect to the accepted values which is not in the same direction for the two metals. One would expect a shift $S_{lead}(T)$ in the same direction for the two metals according to the equations:

$$S_{Pt}(T) - S_{lead}(T) = S_{mPt}(T), \qquad \text{Equation A-10}$$

$$S_{Au}(T) - S_{lead}(T) = S_{mAu}(T). \qquad \text{Equation A-11}$$

A possible reason could be that the temperature gradient we measure has an error so that $\Delta T_{real} = \alpha \Delta T_{measured}$. Following this hypothesis, we applied this correction to our data and we calculated the tip connecting lead thermopower,$S_{lead}(T)$, and the factor α using Equation A-10 and Equation A-11, for different temperatures T (see Table A-2).

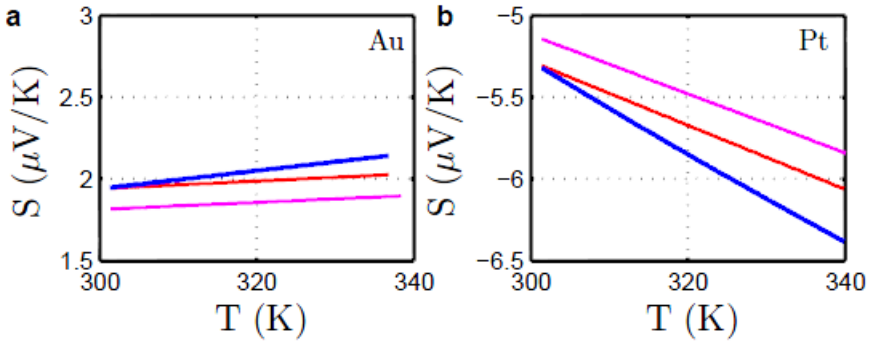

Figure A-9: Absolute thermopower of bulk Au and Pt. Absolute thermopower values versus temperature as measured (magenta line), by applying the correction in temperature and adding the system thermopower offset (red line) and the accepted values from literature (blue line) [Cusack1958] for gold (a) and platinum (b).

In Figure A-9 the shifted absolute thermopower by Equation A-10 and Equation A-11 is plotted with the red line, using $S_{lead}(T) = 0.051\ \mu\text{V/K}$, and the temperature was corrected by the factor $\alpha = 0.958$. The slope of the curve differs slightly from the one of the accepted values. That arises from the fact that we considered the same factor α for the two metals because our purpose was to calculate the system thermopower offset rather than the exact absolute thermopower values. The fact that the factor α is changing for different temperatures (Table A-2) also supports that this factor is different for the two materials. The values of $S_x(T)$ are in the range of $0.05 - 0.06\ \mu\text{V/K}$ and they are small relative to the values we are interested in measuring.

Table A-2: Values of the tip connecting lead thermopower $S_{lead}(T)$ and factor α calculated for different temperatures. Factor α is the factor between the measured and the real temperature $\Delta T_{real} = \alpha \Delta T_{measured}$

$T\ (K)$	α	$S_{lead}(T)\ (\mu V/K)$
301	0.958	0.051
310	0.945	0.051
320	0.932	0.056
330	0.922	0.063

References

[Cusack1958] Cusack, N. and P. Kendall (1958). "The Absolute Scale of Thermoelectric Power at High Temperature." Proceedings of the Physical Society (1960) **72**(5): 898-901.

[Huebener1964] Huebener, R. P. (1964). "THERMOELECTRIC POWER OF LATTICE VACANCIES IN GOLD." PHYSICAL REVIEW A-GENERAL PHYSICS **135**(5a): 1281-&.

[Huebener1965] Huebener, R. P. (1965). "SIZE EFFECT ON PHONON DRAG IN PLATINUM." Physical review **140**(5a): 1834-&.

[Soni2008] Soni, A. and G. S. Okram (2008). "Resistivity and thermopower measurement setups in the temperature range of 5–325 K." Review of Scientific Instruments **79**(12): -.

Appendix E Ideal-Non ideal Op-Amp

As we saw in chapter 4 the electronical offsets are related to the Operational Amplifier (Op-Amp) of the current to voltage amplifier. Here we explain the origin of these offsets. An operational amplifier is a three-terminal device which consists of two high impedance inputs and an output. It amplifies the voltage difference between the inverting and non-inverting input $V_i = V_p - V_n$ and produces a voltage V_0 at the output with respect to the ground.

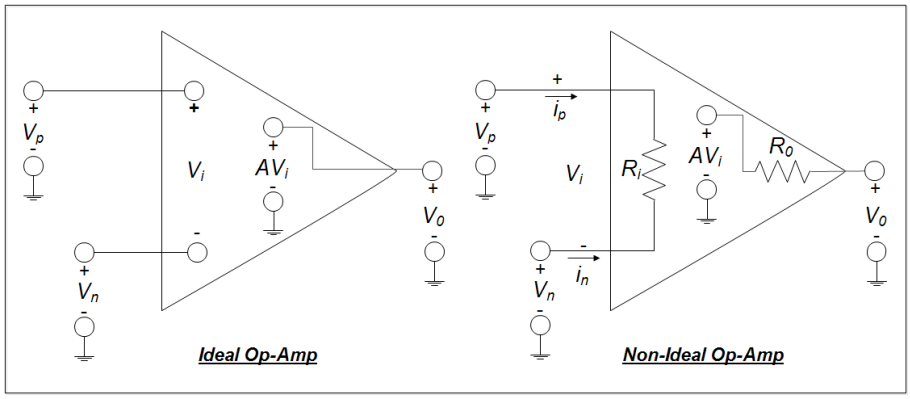

Figure A-10: Equivalent circuit of an Ideal (left) and non-Ideal (right) Op-Amp.

Figure A-10 demonstrates the equivalent circuit of an Ideal and a non-Ideal Operational Amplifier. The Ideal Op-Amp has the following assumptions:

1. Infinite gain: $A = \infty$
2. Infinite input resistance: $R_i = \infty$
3. Zero output resistance: $R_0 = 0$
4. Zero Offset voltage (V_0 will be zero when V_i is zero)

As a consequence of these simplifications $i_p = i_n = 0$ and $V_p = V_n$.

A non-ideal Op-Amp, which is normally the case, will have the following characteristics.

1. Bias current (I_{bias}): The average of the current of the 2 inputs of the Op-Amp. It is caused by the transistors' inputs (that are inside the Op-amp) which draw some current.
2. Offset current (I_{Os}): The difference between the input bias currents. Each current, by entering the Op-Amp, will finally give an offset voltage at the output.
3. Input Offset Voltage(V_{Os}): The voltage produced in the inputs of the Op-Amp due to the DC imbalances within it.
4. Drift: A general term that describes the variation of the DC characteristics of the Op-Amp by time and/or temperature.

Appendix F C_{60} deposition

The most common way of depositing C_{60} molecules on gold is by thermal evaporation in ultra-high vacuum [Joachim1995; Gardener2009; Schull2009]. Wet deposition techniques such as drop casting [Guo2004] and spray coating [Červenka2010] are also used, but less frequently. In our experiments we mainly used drop casting. We deposit the molecules from dilute solutions in 1, 2, 4-trichlorobenzene (TCB) of concentrations close to 10^{-5} - 10^{-8} M by applying several drops to a freshly flamed annealed gold (1,1,1) substrate. After waiting a couple of minutes, we blow off the excess solvent and dry the substrate under a stream of argon gas. Then we let the sample dry for several hours. Examples of topographic images of such samples for different concentrations are shown in Figure A-11a-k. Concentrations close to 10^{-8} M (Figure A-11a-c) give samples with individual molecules spread across terraces and steps, and some small islands of molecules. Increasing the concentration around 10^{-7} M (Figure A-11d-f) the islands are getting bigger and we can still see some individual molecules. For higher concentrations 10^{-5} M (Figure A-11g-i) and 10^{-6} M (Figure A-11j) the number of islands increase and not many individual molecules can be found.

In some cases we used the dip casting technique where we dip the sample in the C_{60} solution for several hours and then we dry it in the same way. In this way the molecules have time to organize on the surface. In Figure A-11k,l the sample was dipped in a solution in Dichloromethane (DCM) with concentration of 10^{-6} M for 24 hours. Areas of hexagonally closed pack structure can be found, as well as disordered molecules. Imaging such samples was quite difficult due to the many molecules on the surface which sometimes were very mobile. It is important to mention here that images Figure A-11e,f,k,l ware taken with a C_{60} tip, which gives sharper images (see chapter 5).

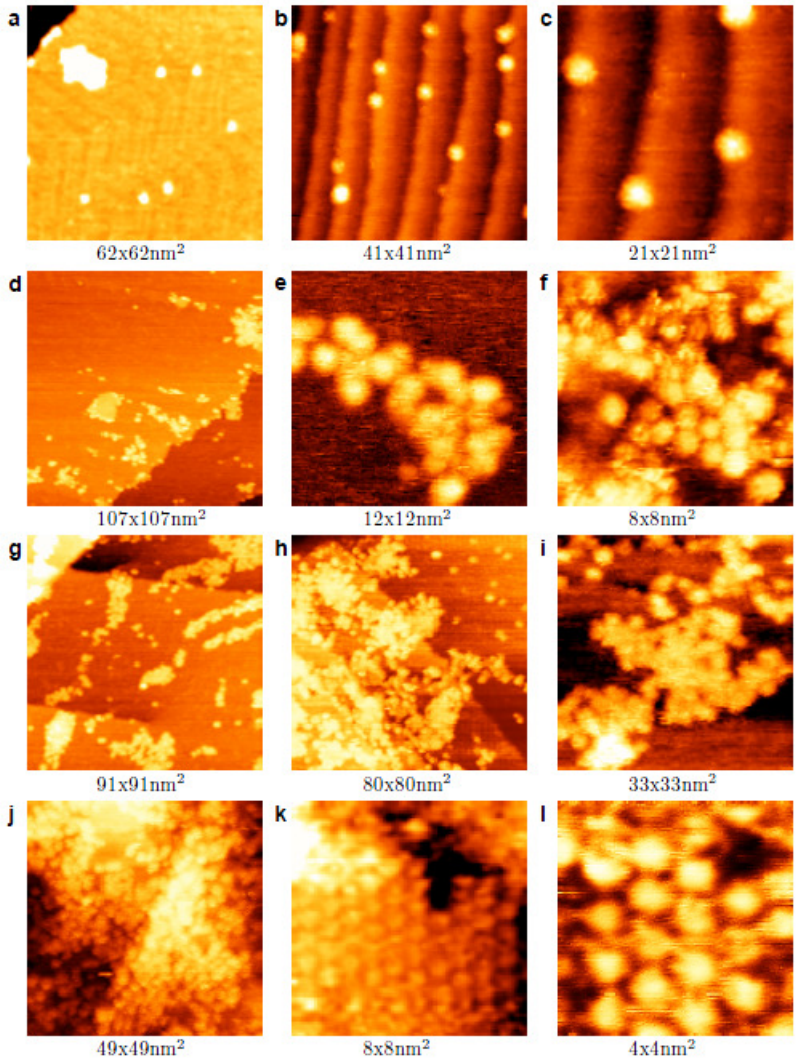

Figure A-11: STM topographic images for different deposition procedures of C_{60}. (a-j) Drop casting from dilute solutions of C_{60} in 1, 2, 4-trichlorobenzene (TCB) of concentrations 10^{-8} M (a-c), 10^{-7} M (d-f), 10^{-5} M (g-i) and 10^{-6} M (j). (k,l) Dip casting from solution of C_{60} in Dichloromethane (DCM) of concentration 10^{-6} M. Images e,f,k,l were taken with C_{60} tip.

References

[Červenka2010] Červenka, J. and C. F. J. Flipse (2010). "Fullerene monolayer formation by spray coating." Nanotechnology **21**(6): 065302.

[Gardener2009] Gardener, J. A., G. A. D. Briggs and M. R. Castell (2009). "Scanning tunneling microscopy studies of C_{60} monolayers on Au(111)." Physical Review B **80**(23): 235434.

[Guo2004] Guo, S., D. P. Fogarty, P. M. Nagel and S. A. Kandel (2004). "Thermal Diffusion of C60 Molecules and Clusters on Au(111)." The Journal of Physical Chemistry B **108**(37): 14074-14081.

[Joachim1995] Joachim, C., J. K. Gimzewski, R. R. Schlittler and C. Chavy (1995). "Electronic Transparence of a Single C_{60} Molecule." Physical Review Letters **74**(11): 2102-2105.

[Schull2009] Schull, G., T. Frederiksen, M. Brandbyge and R. Berndt (2009). "Passing Current through Touching Molecules." Physical Review Letters **103**(20): 206803.

Appendix G Dumbbell molecular wires deposition

In the experiments with dumbbell molecules we mainly used drop casting. We deposited the molecules from dilute solutions in 1, 2, 4-trichlorobenzene (TCB) of concentrations close to 10^{-5} - 10^{-8} M by applying several drops to a freshly flamed annealed gold (1,1,1) substrate. After waiting a couple of minutes, we blew off the excess solvent and dried the substrate under a stream of argon gas. Then we let the sample dry for several hours. Examples of topographic images of such samples for different concentrations are shown in Figure A-12a-k. Concentrations close to 10^{-10} - 10^{-11}M (Figure A-12e,f,k,l) give samples with individual molecules mainly located on the step edges. More dense individual molecules mainly on step-edges and a few on the terraces gave concentrations close to 10^{-9}M (Figure A-12j). Increasing the concentration around 10^{-8} M we get samples of individual molecules spread across terraces and steps, and some small islands of molecules (Figure A-12d,l). For higher concentrations the number of islands and their sizes (Figure A-12a,b,g,h).

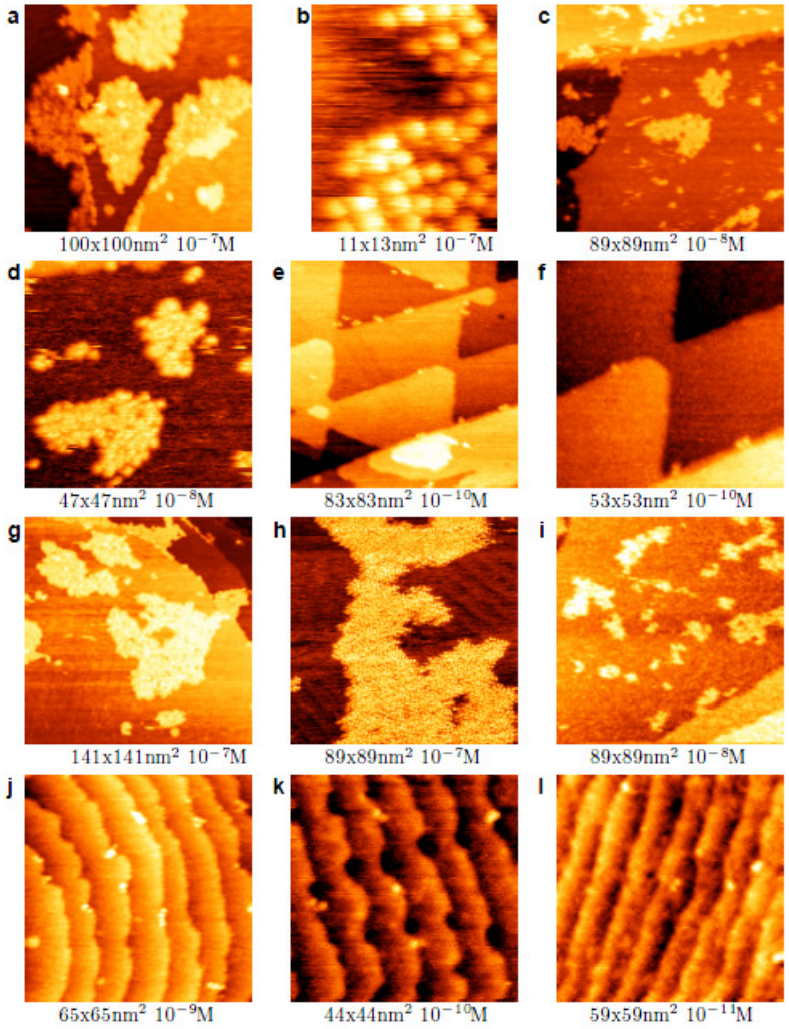

Figure A-12: STM topographic images for dumbbell molecular wires deposited with drop casting. (a-l) Dumbbell-type molecule samples deposited with drop casting from dilute solutions in 1, 2, 4-trichlorobenzene (TCB) of concentrations 10^{-7} M (a,b,g,h), 10^{-8} M (c,d,i), 10^{-9} M (j), 10^{-10} M (e,f,k) and 10^{-11} M (l).

Appendix H Sample-tip cleanliness characterization

After depositing the molecules and during the experiments we check the cleanliness of the tip in a molecule-free area of the sample by gently moving the tip until slight contact with the surface is made and then retracting it (see Figure A-13). For a such approach $\log(G/G_0) - z$ curve, we can fit a straight line to the experimental curve, and its slope will give us the apparent tunneling barrier height, φ, which normally is between 1 and 1.3 eV. This shows that the tip is not contaminated with a molecule, but it does signify the presence of ambient adsorbates. Apparent tunneling barrier height measurements using STM have been carried out under various conditions, such as in humid atmosphere, water and electrochemical environments [Pan1994; Song2002; Hugelmann2003]. The largest apparent tunneling barrier height in all these cases lies close to 1 eV, which is evidently much lower than the vacuum apparent tunneling barrier of 4-5 eV, but it shows that in our experiment the conditions are as clean as possible for ambient conditions. The decrease of the apparent tunneling barrier for an STM experiment is usually attributed to the existence of humidity (or contaminants) in the junction [Hahn1998]. We also check the cleanliness of the tip in the same way several times during the experiments.

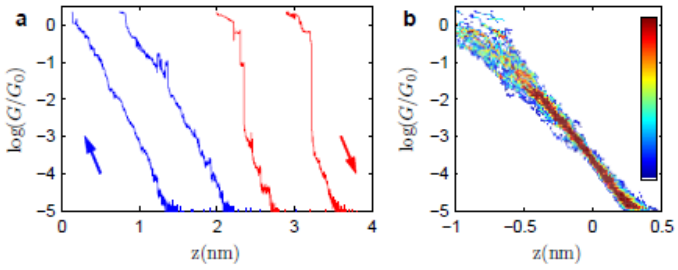

Figure A-13: Checking the cleanliness of a sample. (a) Typical examples of approach (blue) - retraction (red) traces recorded on a molecule free area of a sample. (b) 2D histogram of 30 approach traces recorded on a dumbbell-free area of a sample. This demonstrates the cleanliness of the tip, as only minor bending can be seen close to 1 G_0.

References

[Hahn1998] Hahn, J. R., Y. A. Hong and H. Kang (1998). "Electron tunneling across an interfacial water layer inside an STM junction: tunneling distance, barrier height and water polarization effect." Applied Physics A **66**(1): S467-S472.

[Hugelmann2003] Hugelmann, M. and W. Schindler (2003). "Tunnel barrier height oscillations at the solid/liquid interface." Surface Science **541**(1–3): L643-L648.

[Pan1994] Pan, J., T. W. Jing and S. M. Lindsay (1994). "Tunneling Barriers in Electrochemical Scanning Tunneling Microscopy." The Journal of Physical Chemistry **98**(16): 4205-4208.

[Song2002] Song, M.-B., J.-M. Jang, S.-E. Bae and C.-W. Lee (2002). "Charge Transfer through Thin Layers of Water Investigated by STM, AFM, and QCM." Langmuir **18**(7): 2780-2784.

Appendix I Conductance of Au atomic contacts

It is well-known for Au contacts [Agraït1993], that the conductance decreases in a step-like manner due to atomic rearrangements in the contact [Rubio1996; Rubio2001] with a tendency to exhibit plateaus close to multiples of the conductance quantum. A typical conductance histogram for 1,2,3 atom contacts is dominated by the presence of a peak located very close to $1 \times G_0$, and by two peaks close to 2 and $3 \times G_0$,which are less pronounced, although these histograms are quite sensitive to experimental conditions such as temperature, voltage, breaking speed, environmental conditions, etc. [Yanson1999].

In our measurements described in chapter 6 (Figure 6-4d) the conductance peaks corresponding to G_0 are shifted to slightly higher values. These measurements were a result of soft indentations (up to conductance values of $\sim 6\ G_0$) of the substrate. In order to check if the shift of the conductance peaks is a result of the small penetration of the tip to the substrate we performed small ($\sim 6\ G_0$) and large ($\sim 70\ G_0$) indentations. In Figure A-14a,b examples of conductance measurements G in the last stages of the breaking of Au wires as a result of soft (Figure A-14a) and large (Figure A-14b) indentations are shown. The plateaus for soft indentations are shorter and they have bigger slopes.

We carried out a statistical analysis out of hundreds of curves and we built the conductance histogram (Figure A-15a) and the 2D- histogram for the breaking curves for the two kinds of indentations (Figure A-15c,d). The histogram shows three conductance peaks close to the $1,2,3$ multiples of conductance quantum ($1,2,3 \times G_0$). The histogram for the large indentations is the typical histogram observed for gold atomic contacts, and the peak of one atom contact is located at G_0. In comparison to this histogram the peaks for the soft indentations are slightly shifted to higher conductance values (see blue histogram Figure A-15a). In order to check if this is a random behaviour in some of the curves or there is a transition, we made small and large indentations at the same point of contact continuously, and

we plotted the evolution over time of the individual conductance traces (see Figure A-15b). The magenta dashed line shows where the indentation becomes larger. Each curve in the vertical axis represents the conductance histogram of a single trace. The graph has been obtained from 1200 conductance traces measured continuously. It turns out that at the point where the indentation increases (shown with magenta vertical line) there is a gradual decrease of the conductance until it stabilizes to lower conductance values.

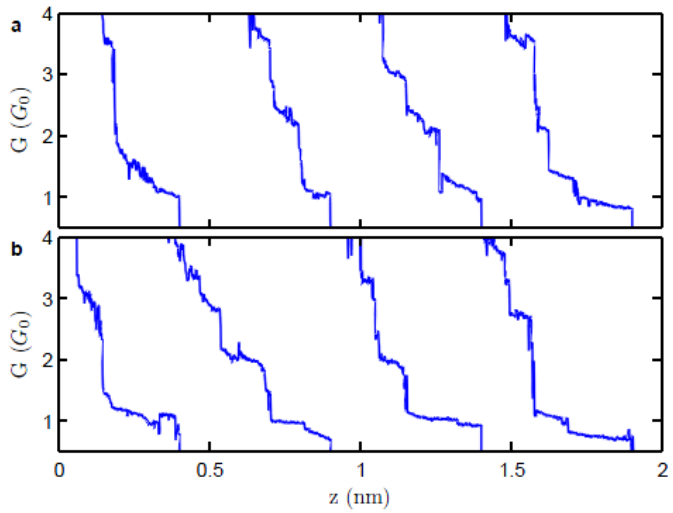

Figure A-14: Conductance curves of Au atomic contacts. (a,b) Examples of conductance curves in the last stages of the breaking of a Au wire at room temperature as a result for small (a) and big (b) indentation of the substrate.

The shift in the conductance is possibly due to the configuration of the atoms participating in the atomic contacts. With a soft indentation of the substrate (up to $\sim 6\ G_0$) the atoms of the metallic contact move just a bit and they can organize and remain in a more stable configuration than that of larger indentations where the atoms rearrange after each indentation. Thus for 1,2,3 atoms contacts, apart from the electron transport through the contact, extra gap tunneling through between the surrounding atoms is taking place. That's also supported by the higher slope of

conductance plateaus for small indentations than for large ones (see 2D histograms Figure A-15c,d and individual curves Figure A-14a,b). In addition, the contacts as a result of larger indentations, have longer conductance plateaus. We can conclude that the shift in the conductance is due to the establishment of a more stable configuration of the atoms participating in the atomic contacts

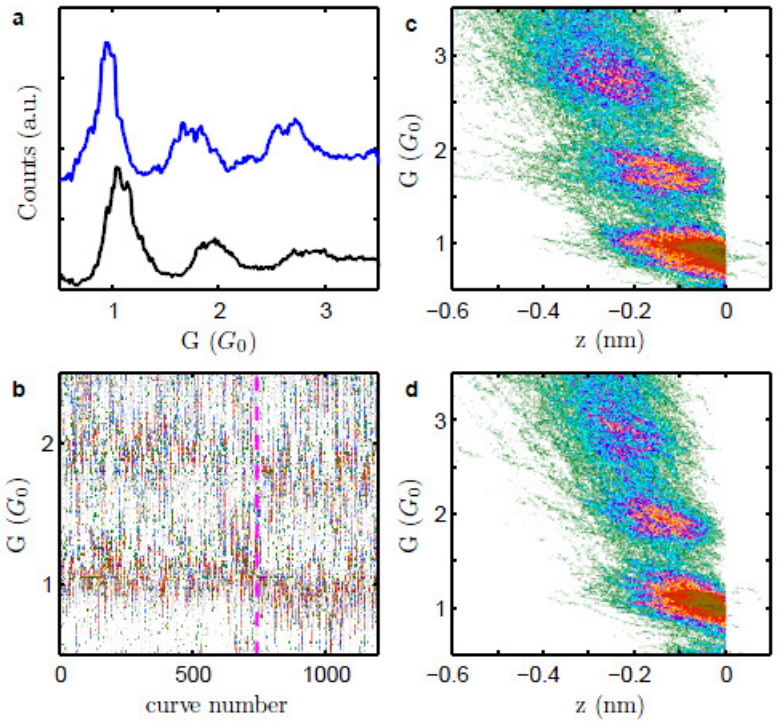

Figure A-15: Conductance of atomic contacts of gold as a result of small and large indentation of the substrate. (a) Conductance histogram for atomic contacts of Au after small (black trace) and large (blue) indentation for 750 and 700 traces respectively. (b) Evolution over time of the individual conductance traces. The magenta line shows where the indentation becomes larger and a gradual decrease of the conductance begins. (c,d) 2D-histograms for small (d) and large (c) indentation of the substrate.

References

[Agraït1993] Agraït, N., J. G. Rodrigo and S. Vieira (1993). "Conductance steps and quantization in atomic-size contacts." Physical Review B **47**(18): 12345-12348.

[Rubio1996] Rubio, G., N. Agraït and S. Vieira (1996). "Atomic-Sized Metallic Contacts: Mechanical Properties and Electronic Transport." Physical Review Letters **76**(13): 2302-2305.

[Rubio2001] Rubio, G., S. R. Bahn, N. Agraït, K. W. Jacobsen and S. Vieira (2001). "Mechanical Properties and Formation Mechanisms of a Wire of Single Gold Atoms." Physical Review Letters **87**(2): 026101.

[Yanson1999] Yanson, A. I. (1999). Quantum conductance properties of atomic-size contacts. T. N. Universiteit Leiden.

Appendix J Green's Functions

Non equilibrium Green's function methods are used to calculate the current in nanoscale conductors under certain bias [Paulsson2002; Ryndyk2009]. We divide the Hamiltonian of the system contact-conductor-contact (see Figure A-16) to the corresponding contributions:

$$\begin{pmatrix} H_1 & \tau_1 & 0 \\ \tau_1^\dagger & H_c & \tau_2^\dagger \\ 0 & \tau_2 & H_2 \end{pmatrix} \begin{pmatrix} |\Psi_1\rangle \\ |\Psi_c\rangle \\ |\Psi_2\rangle \end{pmatrix} = E \begin{pmatrix} |\Psi_1\rangle \\ |\Psi_c\rangle \\ |\Psi_2\rangle \end{pmatrix}, \qquad \text{Equation A-12}$$

where $\tau_{1,2}$ describes the interaction between the conductor (H_c) and contacts ($H_{1,2}$).

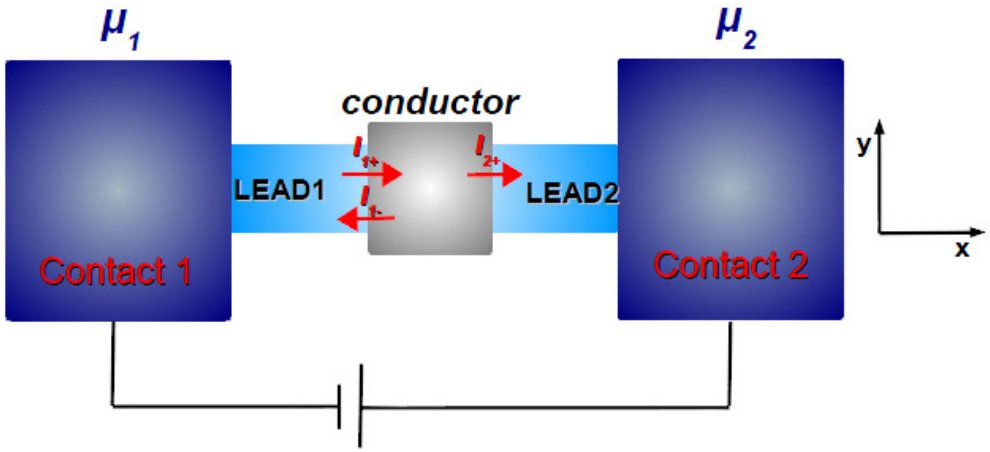

Figure A-16: Conductor with transmission probability T connected to two large contacts through two leads.

Green's function is defined by the following relation:

$$(E - H)G(E) = I. \qquad \text{Equation A-13}$$

Practically, Green's function will give us the response of a system to a perturbation $|u\rangle$ in Schrodinger equation $|\psi\rangle = E|\psi\rangle + |u\rangle$. The response of this perturbation is $|\psi\rangle = -G(E)|u\rangle$. Then, for example, if we want to calculate the wavefunction of the contact ($|\Psi_2\rangle$) we can do so if we know the wavefunction of the conductor ($|\Psi_c\rangle$). From the third row of Equation A-12:

$$H_2|\Psi_2\rangle + \tau_2|\Psi_c\rangle = E|\Psi_2\rangle \Rightarrow |\Psi_2\rangle = g_2(E)\tau_2|\Psi_c\rangle, \qquad \text{Equation A-14}$$

where $g_2 = E - H_2$.

Calculating Green's Function is much easier than solving the Shrodinger equation. Also, for the case of the conductor, we can just calculate Green's function of it (G_c), without calculating it for the whole system:

$$\begin{pmatrix} E-H_1 & \tau_1 & 0 \\ \tau_1^\dagger & E-H_c & \tau_2^\dagger \\ 0 & \tau_2 & E-H_2 \end{pmatrix} \begin{pmatrix} G_1 & G_{1c} & G_{12} \\ G_{c1} & G_c & G_{c2} \\ G_{21} & G_{2c} & G_2 \end{pmatrix} = \begin{pmatrix} I & 0 & 0 \\ 0 & I & 0 \\ 0 & 0 & I \end{pmatrix}. \qquad \text{Equation A-15}$$

By selecting the three equations in the second column of the Green's functions matrix, and solving the system we find the Green's function of the conductor:

$$G_d = (E - G_d - \Sigma_1 - \Sigma_2)^{-1}, \qquad \text{Equation A-16}$$

where $\Sigma_1 = \tau_1^\dagger g_1 \tau_1$ and $\Sigma_2 = \tau_2^\dagger g_2 \tau_2$ are the self-energies (lowercase g is used for the Green's functions of the isolated subsystems).

In the case where a bias $\mu_1 - \mu_2$ is applied in the contact-conductor-contact system, electrons will be injected and occupy the states corresponding to incoming waves in contacts. Then we can calculate the wavefunction on the whole system caused by the incoming wave in contact 1. The wavefunction now is changing to $\left|\Psi_{1,n}\right\rangle + |\Psi^R\rangle\big|$ ($|\Psi_{1,n}\rangle$ is the totally reflected wave and $|\Psi^R\rangle$ is the retarded response of the whole system. Using this wavefunction in the Shrodinger equation we find the device wavefunction and the wavefunction in contact 1:

$$\begin{aligned}\left|\Psi_d\right\rangle &= G_d\tau_1^\dagger\left|\Psi_{1,n}\right\rangle,\\ \left|\Psi_1\right\rangle &= (1+g_1\tau_1 G_d\tau_1^\dagger)\left|\Psi_{1,n}\right\rangle,\end{aligned} \qquad \text{Equation A-17}$$

The current in the conductor from the incoming wave with energy E in contact 1 ($|\Psi_{1,n}\rangle$) with coupling τ_2 is $i_{2\ from\ 1} = -{}^{ie}/_{\hbar}\left(\langle\Psi_2|\tau_2|\Psi_c\rangle - \langle\Psi_c|\tau_2^\dagger|\Psi_2\rangle\right)$. Then by adding across all the modes n we get:

$$i_{2\ from\ 1} = \frac{2e}{h}\int_{E=-\infty}^{\infty} dE f(E,\mu_1) Tr(G_c^\dagger\,\Gamma_2 G_c \Gamma_c). \qquad \text{Equation A-18}$$

Finally, to get the total current in the conductor we have to subtract the current coming from contact 2:

$$I = \frac{2e}{h}\int_{E=-\infty}^{\infty} dE(f(E,\mu_1) - f(E,\mu_2)) Tr(G_c^\dagger\,\Gamma_2 G_c \Gamma_c). \qquad \text{Equation A-19}$$

For zero temperature, it reduces to the Landauer formula:

$$I = \frac{2e^2 V}{h} Tr\left(G_c^\dagger \Gamma_2 G_c \Gamma_c\right) \Rightarrow G_c = \frac{2e^2}{h} Tr\left(G_c^\dagger \Gamma_2 G_c \Gamma_c\right). \qquad \text{Equation A-20}$$

References

[Paulsson2002] Paulsson, M. (2002). "Non Equilibrium Green's Functions for Dummies: Introduction to the One Particle NEGF equations." arXiv:cond-mat/0210519.

[Ryndyk2009] Ryndyk, D. A., R. Gutiérrez, B. Song and G. Cuniberti (2009). Green Function Techniques in the Treatment of Quantum Transport at the Molecular Scale. Energy Transfer Dynamics in Biomaterial Systems. I. Burghardt, V. May, D. A. Micha and E. R. Bittner, Springer Berlin Heidelberg. **93:** 213-335.

Appendix K Quantum transport Calculations

Understanding the electronic transport through single molecules requires the knowledge of their electronic properties when they are attached between two electrodes. The description of the electronic structure entails the correct characterization of a large number of particles: electrons and nuclei, which means solving the many-body Schrödinger equation, which is analytically impossible for a large amount of electrons and nuclei. One way to reduce the complexity of such systems is to use Density Functional Theory which is an ab-initio method which can efficiently handle systems containing thousands of atoms [Parr1989; Springborg1997]. The DFT numerical code used to perform the electronic structure calculations of chapter 5 and 8 is the SIESTA [Soler2002] (Spanish Initiative for Electronic Simulations with Thousands of Atoms). Apart from the Hamiltonian of the system we can get an optimization of our structure (geometry with minimal ground state energy). Before setting a calculation with SIESTA code in order to get the Hamiltonian for the desired system we have to:

1. Construct the geometrical configuration of the system.
2. Generate an appropriate pseudo-potential for each element.
3. If the system is periodic, define the lattice vectors
4. Choose the basis set for each element present in the calculation.
5. Set the computational parameters

Once the Hamiltonian of the System is calculated we use the ab-initio code SMEAGOL [Alexandre2005] which combines this Hamiltonian with non-equilibrium Green's function scattering approach in order to observe the transport properties of the system. Before using SMEAGOl code we need to model the quantum transport problem of the nanometer sized device (molecule), which is sandwiched between two macroscopic electrodes. Figure A-17 shows the system from three different perspectives: thermodynamical, quantum mechanical and electrostactical . From the thermodynamic point of view the system consists of two bulk leads and a

central region which includes the molecule and a part of the leads. The two leads are in different chemical potentials (μ_L, μ_R) which, if they are equal, the system is in thermodynamic equilibrium and if they are different (bias voltage applied) current will flow.

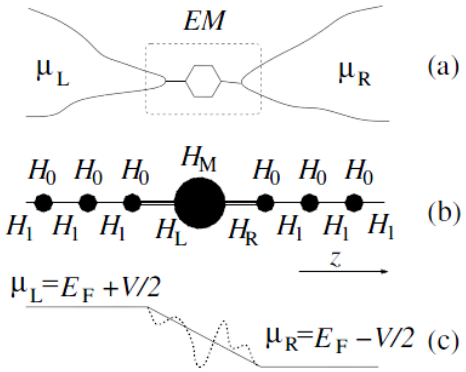

Figure A-17: Schematic representation of the transport problem from three different perspectives. (a) Thermodynamical. (b) Quantum mechanical. (c) Electrostactical.[Rocha2007]

In the Quantum mechanical point of view (Figure A-17b), modeling of the macroscopic electrodes as infinitely long leads with infinite cross-sections with the finite scattering region in the middle EM (Extended Molecule) will result in the Hamiltonian of the system being an infinite Hermitian matrix ($\mathcal{H}$). In order to avoid that, we make two assumptions:

1. Leads are semi-infinite defect-free crystalline metals, and the Hamiltonian will have a regular periodic structure and a unit cell along which the direction of the transport can be calculated.
2. Periodic boundary conditions are used in order to avoid the infinite cross-section. The system is repeated periodically in the transverse direction.

Then in order to further simplify the problem we introduce the concept of a principal layer (PL), which is the smallest cell that repeats periodically in the

direction of transport, and is constructed in a way that it interacts only with the next neighbored principal layer. We define H_0 (the $N \times N$matrix describing all interactions in a PL), H_1 (the $M \times M$ matrix describing the interactions between the PLs), H_{LM} and H_{RM} (the matrix describing the interaction between the last PLs and the extended molecule at the left hand side and right hand side respectively). Finally, $\mathcal{H}$takes the following form:

$$\mathcal{H} = \begin{pmatrix} \ddots & H_1 & 0 & . & . & . & . \\ H_1^\dagger & H_0 & H_1 & 0 & . & . & . \\ 0 & H_1^\dagger & H_0 & H_{LM} & 0 & . & . \\ . & 0 & H_{ML} & H_M & H_{MR} & 0 & . \\ . & . & 0 & H_{RM} & H_0 & H_1 & 0 \\ . & . & . & 0 & H_1^\dagger & H_0 & H_1 \\ . & . & . & . & 0 & H_1^\dagger & \ddots \end{pmatrix}. \qquad \text{Equation A-21}$$

$\mathcal{H}$ now has the same structure as the Hamiltonian of one-dimensional chain but with block elements instead of chains. In the electrostatic point of view (Figure A-17c) an external bias voltage applied on the leads will produce a rigid shift of the whole spectrum which will lead to a non-trivial potential profile over the EM which will need to be calculated self-consistently. The resulting potential must match one of the leads at the boundaries of the EM, in order not to develop a discontinuity with the generation of spurious scattering. Therefore, in order to achieve a good match of the electrostatic potential, several layers of the leads are usually included in the extended molecule.

Then, by assuming that states deep inside the electrodes are scattered by the potential created by the central EM, Green's Functions techniques [Datta1997] are used to calculate the ground state electronic properties of the system. Finally, at the zero-bias limit using the Landauer-Buttiker formalism [Büttiker1985], the conductance of the scatterer is calculated.[Rocha2007]

References

[Alexandre2005] Alexandre, R. R., M. G.-s. Víctor, W. B. Steve, J. L. Colin, F. Jaime, et al. (2005). "Towards molecular spintronics." Nature Materials **4**(4): 335-339.

[Büttiker1985] Büttiker, M., Y. Imry, R. Landauer and S. Pinhas (1985). "Generalized many-channel conductance formula with application to small rings." Physical Review B **31**(10): 6207-6215.

[Datta1997] Datta, S. (1997). Electronic Transport in Mesoscopic Systems, Cambridge University Press.

[Parr1989] Parr, R. G. and W. Yang (1989). Density-Functional Theory of Atoms and Molecules, Oxford University Press, USA.

[Rocha2007] Rocha, A. R. (2007). Theoretical and Computational Aspects of electronic transport at the Nanoscale. PhD, University of Dublin.

[Soler2002] Soler, J. M., E. Artacho, J. D. Gale, A. García, J. Junquera, et al. (2002). "The SIESTA method for ab initio order-N materials simulation." J. Phys.: Condens. Matter **14**(2745).

[Springborg1997] Springborg, M. (1997). Density-functional methods in chemistry and materials science, Wiley.

Publication List

[1] *Engineering the Thermopower of C_{60} Molecular Junctions.*
C. Evangeli, K. Gillemot, E., M. T. González, G. Rubio-Bollinger, C. J. Lambert, and N. Agraït. Nano Letters **13**, 2141-5 (2013).

[2] *A Detailed Experimental and Theoretical Study into the Properties of C_{60} Dumbbell Junctions*
K. Gillemot, C. Evangeli, E. Leary, A. La Rosa, M. T. González, S. Filippone, I. Grace , G. Rubio-Bollinger, J. Ferrer, N. Martín , C. J. Lambert, N. Agraït. Small **9**, 3812–3822 (2013).

[3] *Does the Cyclopropane Ring Enhance the Electronic Communication in Dumbbell-type C_{60} dimers?*
A. La Rosa, K. Gillemot, E. Leary, C. Evangeli, T. Gonzalez, S. Filippone, N. Agraït, C. J. Lambert, N. Martín
J. Org. Chem. 79, 4871-4877 (2014).

[4] *Quantum thermopower of metallic atomic-size contacts at room temperature*
C. Evangeli, M. Matt, L. Rincón-García, F. Pauly, P.r Nielaba, G. Rubio-Bollinger, J. C. Cuevas, and N. Agraït
submitted to Nano Letters (october 2014)

[5] *Locating the levels in dithiafulvalene functionalized molecular wires*
E. Leary, C. Evangeli, M. T. González, G. Rubio-Bollinger, N. Agraït, in preparation.